

Image Matching Filtering and Refinement by Planes and Beyond

Fabio Bellavia^{1*}, Zhenjun Zhao², Luca Morelli³, Fabio Remondino³

¹Università degli Studi di Palermo, Italy.

²The Chinese University of Hong Kong, China.

³Bruno Kessler Foundation, Italy.

*Corresponding author(s). E-mail(s): fabio.bellavia@unipa.it;

Contributing authors: ericzzj89@gmail.com; lmorelli@fbk.eu; remondino@fbk.eu;

Abstract

This paper introduces a modular, non-deep learning method for filtering and refining sparse correspondences in image matching. Assuming that motion flow within the scene can be approximated by local homography transformations, matches are aggregated into overlapping clusters corresponding to virtual planes using an iterative RANSAC-based approach, with non-conforming correspondences discarded. Moreover, the underlying planar structural design provides an explicit map between local patches associated with the matches, enabling optional refinement of keypoint positions through cross-correlation template matching after patch reprojection. Finally, to enhance robustness and fault-tolerance against violations of the piece-wise planar approximation assumption, a further strategy is designed for minimizing relative patch distortion in the plane reprojection by introducing an intermediate homography that projects both patches into a common plane. The proposed method is extensively evaluated on standard datasets and image matching pipelines, and compared with state-of-the-art approaches. Unlike other current comparisons, the proposed benchmark also takes into account the more general, real, and practical cases where camera intrinsics are unavailable. Experimental results demonstrate that our proposed non-deep learning, geometry-based approach achieves performances that are either superior to or on par with recent state-of-the-art deep learning methods. Finally, this study suggests that there are still development potential in actual image matching solutions in the considered research direction, which could be in the future incorporated in novel deep image matching architectures.

Keywords: image matching, keypoint refinement, planar homography, normalized cross-correlation, SIFT, SuperGlue, LoFTR

1 Introduction

1.1 Background

Image matching constitutes the backbone of most higher-level computer vision tasks and applications that require image registration to recover the 3D scene structure, including the camera

poses. Image stitching [1, 2], Structure-from-Motion (SfM) [2–5], Simultaneous Localization and Mapping (SLAM) [2, 6] and the more recently Neural Radiance Fields (NeRF) [7, 8] and Gaussian Splatting (GS) [9, 10] are probably nowadays the most common, widespread and major tasks critically relying on image matching.

Image matching traditional paradigm can be organized into a modular pipeline concerning keypoint extraction, feature description, and the proper correspondence matching [11]. This representation is being neglected in modern deep end-to-end image matching methods due to their intrinsic design which guarantees a better global optimization at the expense of the interpretability of the system. Notwithstanding that end-to-end deep networks represent for many aspects the State-Of-The-Art (SOTA) in image matching, such in terms of the robustness and accuracy of the estimated poses in complex scenes [12–18], handcrafted image matching pipelines such as the popular Scale Invariant Feature Transform (SIFT) [19] are employed still today in practical applications [2, 4] due to their scalability, adaptability, and understandability. Furthermore, handcrafted or deep modules remain present in post-process modern monolithic deep architectures, to further filter the final output matches as done notably by the RAnDom SAmpling Consensus (RANSAC) [20] based on geometric constraints.

Image matching filters to prune correspondences are not limited to RANSAC, which in any of its form [21–24] still remains mandatory nowadays as final step, and have been evolved from handcrafted methods [25–33] to deep ones [34–41]. In addition, more recently methods inspired by coarse-to-fine paradigm, such as the Local Feature TRansformer (LoFTR) [14], have been developed to refine correspondences [42–44], which can be considered as the introduction of a feedback-system in the pipelined interpretation of the matching process.

1.2 Main contribution

As contribution, within the former background, this paper introduces a modular approach to filter and refine matches as post-process before RANSAC. The key idea is that the motion flow within the images, i.e. the correspondences, can be approximated by local overlapping homography transformations [45]. This is the core concept of traditional image matching pipelines, where local patches are approximated by less constrained transformations going from a fine to a coarse scale level. Specifically, besides the similarity and affine

transformations, the planar homography is introduced at a further level. The whole approach proceeds as follows:

- The Multiple Overlapping Planes (MOP) module aggregates matches into soft clusters, each one related to a planar homography roughly representing the transformation of included matches. On one hand, matches unable to fit inside any cluster are discarded as outliers, on the other hand, the associated planar map can be used to normalize the patches of the related keypoint correspondences. As more matches are involved in the homography estimation, the patch normalization process becomes more robust than the canonical ones used for instance in SIFT. Furthermore, homographies better adapt the warp as they are more general than similarity or affine transformations. MOP is implemented by iterating RANSAC to greedily estimate the next best plane according to a multi-model fitting strategy. The main difference from previous similar approaches [46, 47], is in maintaining matches during the iterations in terms of strong and weak inliers according to two different reprojection errors to guide the cluster partitioning.
- The Middle Homography (MiHo) module additionally improves the patch normalization by further minimizing the relative patch distortion. More in detail, instead of reprojecting the patch of one image into the other image taken as reference according to the homography associated with the cluster, both the corresponding patches are reprojected into a virtual plane chosen to be in the middle of the base homography transformations so that globally the deformation is distributed into both the two patches, reducing the patch distortions with respect to the original images due to interpolation but also to the planar approximation.
- The Normalized Cross-Correlation (NCC) is employed following traditional template matching [2, 48] to improve the keypoint localization in the reference middle homography virtual plane using one patch as a template to being localized on the other patch. The relative shift adjustment found on the virtual plane is finally back-projected through into the original images. In order to improve the process, the template patch is perturbed by small rotations and

anisotropic scaling changes for a better search in the solution space.

MOP and MiHo are purely geometric-based, requiring only keypoint coordinates, while NCC relies on the image intensity in the local area of the patches. The early idea of MOP+MiHo+NCC can be found in [49]. Furthermore, MOP overlapping plane exploitation concept have been introduced in [50], while MiHo definition was draft in [51]. The proposed approach is handcrafted and hence more general as it does not require re-training to adapt to the particular kind of scene and its behavior is more interpretable as not hidden by deep architectures. As reported and discussed later in this paper, RANSAC takes noticeable benefits from MOP+MiHo as pre-filter before it in most configurations and scene kinds, and in any case does not deteriorate the matches. Concerning MOP+MiHo+NCC instead, keypoint localization accuracy seems to strongly depend on the kind of extracted keypoint. In particular, for corner-like keypoints, which are predominant in detectors such as the Keypoint Network (Key.Net) [52] or SuperPoint [53], NCC greatly improves the keypoint position, while for blob-like keypoints, predominant for instance in SIFT, NCC application can degrade the keypoint localization, due probably to the different nature of their surrounding areas. Nevertheless, the proposed approach indicates that there are still margins for improvements in current image matching solutions, even the deep-based ones, exploiting the analyzed methodology.

1.3 Additional contribution

As further contribution, an extensive comparative evaluation is provided against eleven less and more recent SOTA deep and handcrafted image matching filtering methods on both non-planar indoor and outdoor standard benchmark datasets [11, 54, 55], as well as planar scenes [56, 57]. Each filtering approach, including several combinations of the three proposed modules, has been tested to post-process matches obtained with seven different image matching pipelines and end-to-end networks, also considering distinct RANSAC configurations. Moreover, unlike the mainstream evaluation which has been taken as current standard [14], the proposed benchmark assumes that no camera intrinsics are available, reflecting a

more general, realistic, and practical scenario. On this premise, the pose error accuracy is defined, analyzed, and employed with different protocols intended to highlight the specific complexity of the pose estimation working with fundamental and essential matrices [45], respectively. This analysis reveal the many-sided nature of the image matching problem and of its solutions.

1.4 Paper organization

The rest of the paper is organized as follows. The related work is presented in Sec. 2, the design of MOP, MiHo, and NCC is discussed in Sec. 3, and the evaluation setup and the results are analyzed in Sec. 4. Finally, conclusions and future work are outlined in Sec. 5.

1.5 Additional resources

Code and data are freely available online¹. Data also include high-resolution versions of the images, plots, and tables presented in this paper².

2 Related work

2.1 Disclaimer and further references

The following discussion is far to be exhaustive due to more than three decades of active research and progress in the field, which is still ongoing. The reader can refer to [58–61] for a more comprehensive analysis than that reported below, which is related and covers only the methods discussed in the rest of the paper.

2.2 Non-deep image matching

Traditionally, image matching is divided into three main steps: keypoint detection, description, and proper matching.

2.2.1 Keypoint detectors

Keypoint detection is aimed at finding salient local image regions whose feature descriptor vectors are at the same time-invariant to image transformations, i.e. repeatable, and distinguishable from other non-corresponding descriptors, i.e. discriminant. Clearly, discriminability decreases as long

¹<https://github.com/fb82/MiHo>

²<https://github.com/fb82/MiHo/tree/main/data/paper>

as invariance increases and vice-versa. Keypoints are usually recognized as corner-like and blob-like ones, even if there is no clear separation within them outside ad-hoc ideal images. Corners are predominantly extracted by the Harris detector [62], while blobs by SIFT [19]. Several other handcrafted detectors exist besides the Harris and the SIFT one [63–65], but excluding deep image matching nowadays the former and their extensions are the most commonly adopted. Harris and SIFT keypoint extractors rely respectively on the covariance matrix of the first-order derivatives and the Hessian matrix of the second-order derivatives. Blobs and corners can be considered each other analogues for different derivative orders, as in the end, a keypoint in both cases correspond to a local maxima response to a filter which is a function of the determinant of the respective kind of matrix. Blob keypoint centers tend to be pushed away from edges, which characterize the regions, more than corners due to the usage of high-order derivatives. More recently, the joint extraction and refinement of robust keypoints has been investigated by the Gaussian Mixture Models for Interpretable Keypoint Refinement and Scoring (GMM-IKRS) [66]. The idea is to extract image keypoints after several homography warps and cluster them after back-projection into the input images so as to select the best clusters in terms of robustness and deviation, as another perspective of the Affine SIFT (ASIFT) [67] strategy.

2.2.2 Keypoint descriptors

Feature descriptors aim at embedding the keypoint characterization into numerical vectors. There has been a long research interest in this area, both in terms of handcrafted methods and non-deep machine learning ones, which contributed actively to the current development and the progress made by current SOTA deep image matching. Among non-deep keypoint descriptors, nowadays only the SIFT descriptor is practically still used and widespread due to its balance within computational efficiency, scaling, and matching robustness. SIFT descriptor is defined as the gradient orientation histogram of the local neighborhood of the keypoint, also referred to as patch. Many high-level computer vision applications like COLMAP [4] in the case of SfM are based on SIFT. Besides SIFT keypoint detector

& descriptor, the Oriented FAST and Rotated BRIEF (ORB) [68] is a pipeline surviving still today in the deep era worth to be mentioned. ORB is the core of the popular ORB-SLAM [6], due to its computational efficiency, even if less robust than SIFT. Nevertheless, it seems to be going to be replaced by SIFT with the increased computational capability of current hardware [69].

2.2.3 Patch normalization

Actually, the patch normalization takes place in between the detection and description of the keypoints, and it is critical for effective computation of the descriptor to be associated with the keypoint. Patch normalization is implicitly hidden inside both keypoint extraction and description and its task roughly consists of aligning and registering patches before descriptor computation [19]. The key idea is that complex image deformations can be locally approximated by more simple transformations as long as the considered neighborhood is small. Under these assumptions, SIFT normalizes the patch by a similarity transformation, where the scale is inferred by the detector and the dominant rotation is computed from the gradient orientation histogram. Affine covariant patch normalization [67, 70, 71] was indeed the natural evolution, which can improve the normalization in case of high degrees of perspective distortions. Notice that in the case of only small scene rotation, up-right patches computed neglecting orientation alignment can lead to better matches since a strong geometric constraint limiting the solution space is imposed [72]. Concerning instead patch photometric consistency, affine normalization, i.e. by mean and standard deviation, is usually the preferred choice being sufficiently robust in the general case [19].

2.2.4 Descriptor similarity and global geometric constraints

The last step is the proper matching, which mainly pairs keypoints by considering the distance similarity on the associated descriptors. Nearest Neighbor (NN) and Nearest Neighbor Ratio (NNR) [19] are the common and simple approaches even if additional extensions have been developed [32, 73]. For many tasks descriptor similarity alone does not provide satisfactory

results, which can be achieved instead by including a further filtering post-process by constraining matches geometrically. RANSAC provides an effective method to discard outliers under the more general epipolar geometry constraints of the scene or in the case of planar homographies. The standard RANSAC continues to be extended in several ways [21, 22]. Worth mentioning are the Degenerate SAmpling Consensus (DegenSAC) [24] to avoid degenerate configurations, and the MArGinalized SAmpling Consensus (MAGSAC) [23] for defining a robust inlier threshold which remains the most critical parameter.

2.2.5 Local geometric constraints

RANSAC exploits global geometric constraints. A more general and relaxed geometric assumption than RANSAC is to consider only local neighborhood consistency across the images as done in Grid-based Motion Statistics (GMS) [26] using square neighborhood, but also circular [25] and affine-based [27, 28] neighborhoods or Delaunay triangulation [28, 32] have been employed. In most cases, these approaches require an initial set of robust seed matches for initialization whose selection may become critical [74], while other approaches explicitly exploit descriptor similarities to rank matches [32]. In this respect, the vanilla RANSAC and GMS are pure geometric image filters. Notice that descriptor similarities have been also exploited successfully within RANSAC [75]. Closely connected to local filters, another class of methods is designed instead to estimate and interpolate the motion field upon which to check match consistency [29–31]. Local neighborhood consistency can be framed also into RANSAC as done by Adaptive Locally-Affine Matching (AdaLAM) [33] which runs multiple local affine RANSACs inside the circular neighborhoods of seed matches. AdaLAM design can be related with GroupSAC [76], which draws hypothesis model sample correspondences from different clusters, and with the more general multi-model fitting problem for which several solutions have been investigated [77, 78]. Among these approaches the recent Consensus Clustering (CC) [79] has been developed for the specific case of multiple planar homographies.

2.3 Deep image matching

2.3.1 Standalone pipeline modules

Deep learning evolution has provided a boost to image matching as well as other computer vision research fields thanks to the evolution of the deep architectures, hardware and software computational capability and design, and the huge amount of datasets now available for the training. Hybrid pipelines are raised first, replacing handcrafted descriptors with deep ones, as the feature descriptor module is the most natural and immediate to be replaced in the pipeline evolution. SOTA in this sense is represented by the Hard Network (Hard-Net) [80] and similar networks [81, 82] trained on contrastive learning with hard mining. For what concerns the keypoint extraction, better results with respect to the handcrafted counterparts were achieved by driving the network to mimic hand-crafted detector design as for KeyNet [52]. Deep learning has been successfully applied to design standalone patch normalization modules to estimate the reference patch orientation [83, 84] or more complete affine transformations as in the Affine Network [84]. The mentioned deep modules have been employed successfully in many hybrid matching pipelines, especially in conjunction with SIFT [11] or Harris corners [85].

2.4 Joint detector & descriptor networks

A relevant characteristic in deep image matching which made it able to exceed handcrafted image matching pipelines was gained by allowing concurrently optimizing both the detector & descriptor. SuperPoint [53] integrates both of them in a single network and does not require a separate yet consecutive training of these as [86]. A further design feature that enabled SuperPoint to become a reference in the field is the use of homographic adaptation, which consists of the use of planar homographies to generate corresponding images during the training, to allow self-supervised training. Further solutions were proposed by architectures similar to SuperPoint as in [87]. Moreover, the Accurate and Lightweight Keypoint Detection and Descriptor Extraction (ALIKE) [88] implements a differentiable Non-Maximum Suppression (NMS) for the keypoint selection on the score map, and the DIScrete Keypoints (DISK) [89]

employs reinforcement learning. ALIKE design is further improved by A Lighter Keypoint and descriptor Extraction network with Deformable transformation (ALIKED) [13] using deformable local features for each sparse keypoint instead of dense descriptor maps, resulting in saving computational budget. Alternative rearrangements in the pipeline structure to use the same sub-network for both detector & descriptor (detect-and-describe) [90], or to extract descriptors and then keypoints (describe-then-detect) [91] instead of the common approach (detect-then-describe) have been also investigated. More recently, the idea of decoupling the two blocks by formulating the matching problems in terms of 3D tracks in large-scale SfM has been applied in Detect, Don't Describe-Describe, Don't Detect (DeDoDe) [92] and DeDoDe v2 [93] with interesting results.

2.4.1 Full end-to-end architectures

Full end-to-end deep image matching architectures arose with SuperGlue [94], which incorporates a proper matching network exploiting self and cross attentions through transformers to jointly encode keypoint positions and visual data into a graph structure, and a differentiable form of the Sinkhorn algorithm to provide the final assignments. SuperGlue can represent a breakthrough in the areas and has been extended by the recent LightGlue [12] improving its efficiency, accuracy and training process. Detector-free end-to-end image matching architectures have been also proposed, which avoid explicitly computing a sparse keypoint map, considering instead a semi-dense strategy. The Local Feature Transformer (LoFTR) [14] is a competitive realization of these matching architectures, which deploys a coarse-to-fine strategy using self and cross attention layers on dense feature maps and has been employed as a base for further design extensions [15, 16]. Notice that end-to-end image matching networks are not fully rotational invariant and can handle only relatively small scene rotations, except specific architectures designed with this purpose [95–97]. Coarse-to-fine strategy following LoFTR design has been also applied to hybrid canonical pipelines with only deep patch and descriptor modules, leading to matching results comparable in challenging scenarios at an increased computation

cost [50]. More recently, dense image matching networks that directly estimate the scene as dense point maps [17] or employing Gaussian process [18], achieve SOTA results in many benchmarks but are more computationally expensive than sparse or semi-dense methods.

2.4.2 Outlier rejection with geometric constraints

The first effective deep matching filter module was achieved with the introduction of the context normalization [34], which is the normalization by mean and standard deviation, that guarantees to preserve permutation equivalence. The Attentive Context Network (ACNe) [35] further includes local and global attention to exclude outliers from context normalization, while the Order-Aware Network (OANet) [36] adds additional layers to learn how to cluster unordered sets of correspondences to incorporate the data context and the spatial correlation. The Consensus Learning Network (CLNet) [37] prunes matches by filtering data according a local-to-global dynamic neighborhood consensus graphs in consecutive rounds. The Neighbor Consistency Mining Network (NCMNet) [38] improves CLNet architecture by considering different neighborhoods in the feature space, the keypoint coordinate space, and a further global space that considers both previous ones altogether with cross-attention. More recently, the Multiple Sparse Semantics Dynamic Graph Network (MS²DG-Net) [39] designs the filtering in terms of a neighborhood graph through transformers [98] to capture semantics similar structures in the local topology among correspondences. Unlike previous deep approaches, ConvMatch[40] builds a smooth motion field by making use of Convolutional Neural Network (CNN) layers to verify the consistency of the matches. DeMatch [41] refines ConvMatch motion field estimation for a better accommodation of scene disparities by decomposing the rough motion field into several sub-fields. Finally, notice that deep differentiable RANSAC modules have been investigated as well [99, 100].

2.4.3 Keypoint refinement

The coarse-to-fine strategy trend has pushed the research of solutions focusing on the refinement

of keypoint localization as a standalone module after the coarse assignment of the matches. Worth mentioning is Pixel-Perfect SfM [101] that learns to refine multi-view tracks on their photometric appearance and the SfM structure, while Patch2Pix [42] refines and filters patches exploiting image dense features extracted by the network backbone. Similar to Patch2Pix, Keypoint2Subpx [43] is a recent lightweight module to refine only matches requiring as input the descriptors of the local heat map of the related correspondences beside keypoints position. Finally, the Filtering and Calibrating Graph Neural Network (FC-GNN) [44] is an attention-based Graph Neural Network (GNN) jointly leveraging contextual and local information to both filter and refine matches. Unlike Patch2Pix and Keypoint2Subpx, does not require feature maps or descriptor confidences as input, as also the proposed MOP+MiHo+NCC. Similarly to FC-GNN, the proposed approach uses both global context and local information to refine matches, respectively to warp and check photometric consistency, but differently from FC-GNN it currently only employs global contextual data since does not implement any feedback system to discard matches on patch similarity after the alignment refinement.

3 Proposed approach

3.1 Multiple Overlapping Planes (MOP)

3.1.1 Preliminaries

MOP assumes that motion flow within the images can be piecewise approximated by local planar homography.

Representing with an abuse of notation the reprojection of a point $\mathbf{x} \in \mathbb{R}^2$ through a planar homography $\mathbf{H} \in \mathbb{R}^{3 \times 3}$ with \mathbf{H} non-singular as $\mathbf{H}\mathbf{x}$, a match $m = (\mathbf{x}_1, \mathbf{x}_2)$ within two keypoints $\mathbf{x}_1 \in I_1$ and $\mathbf{x}_2 \in I_2$ is considered an inlier based on the maximum reprojection error

$$\varepsilon_{\mathbf{H}}(m) = \max (\|\mathbf{x}_2 - \mathbf{H}\mathbf{x}_1\|, \|\mathbf{x}_1 - \mathbf{H}^{-1}\mathbf{x}_2\|) \quad (1)$$

For a set of matches $\mathcal{M} = \{m\}$, the inlier subset is provided according to a threshold t as

$$\mathcal{J}_{\mathbf{H},t}^{\mathcal{M}} = \{m \in \mathcal{M} : \varepsilon_{\mathbf{H}}(m) \leq t\} \quad (2)$$

A proper scene planar transformation must be quasi-affine to preserve the convex hull [45] with respect to the minimum sampled model generating \mathbf{H} in RANSAC so the inlier set effectively employed is

$$\mathcal{I}_{\mathbf{H},t}^{\mathcal{M}} = \mathcal{J}_{\mathbf{H},t}^{\mathcal{M}} \cap \mathcal{Q}_{\mathbf{H}}^{\mathcal{M}} \quad (3)$$

where $\mathcal{Q}_{\mathbf{H}}^{\mathcal{M}}$ is the set of matches in \mathcal{M} satisfying the quasi-affinity property with respect to the RANSAC minimum model of \mathbf{H} described later in Eq. 12.

3.1.2 Main loop

MOP iterates through a loop where a new homography is discovered and the match set is reduced for the next iteration. Iterations halt when the counter c_f of the sequential failures at the end of a cycle reaches the maximum allowable value $c_f^* = 3$. If not incremented at the end of the cycle, c_f is reset to 0. As output, MOP returns the set \mathcal{H}^* of found homographies \mathbf{H} which covers the image visual flow.

Starting with $c_f = 0$, $\mathcal{H}^0 = \emptyset$ and the initial set of input matches \mathcal{M}^0 provided by the image matching pipeline, MOP at each iteration k looks for the best planar homography \mathbf{H}^k compatible with the current match set \mathcal{M}^k according to a relaxed inlier threshold $t_l = 15$ px. When the number of inliers provided by t_l is less than the minimum required amount, set to $n = 12$, i.e.

$$\left| \mathcal{I}_{\mathbf{H}^k, t_l}^{\mathcal{M}^k} \right| < n \quad (4)$$

the current \mathbf{H}^k homography is discarded and the failure counter c_f is incremented without updating the iteration counter k , the next match set \mathcal{M}^{k+1} and the output list \mathcal{H}^{k+1} . Otherwise, MOP removes the inlier matches of \mathbf{H}^k for a threshold t^k for the next iteration $k + 1$

$$\mathcal{M}^{k+1} = \mathcal{M}^k \setminus \mathcal{I}^k \quad (5)$$

where $\mathcal{I}^k = \mathcal{I}_{H^k, t^k}^{\mathcal{M}^k}$ and updates the output list

$$\mathcal{H}^{k+1} = \mathcal{H}^k \cup \{H^k\} \quad (6)$$

The threshold t^k adapts to the evolution of the homography search and is equal to a strict threshold $t_h = t_l/2$ in case the cardinality of the inlier set using t_h is greater than half of n , i.e. in the worst case no more than half of the added matches should belong to previous overlapping planes. If this condition does not hold t^k turns into the relaxed threshold t_l and the failure counter c_f is incremented

$$t^k = \begin{cases} t_h & \text{if } |\mathcal{I}_{H^k, t_h}^{\mathcal{M}^k}| > \frac{n}{2} \\ t_l & \text{otherwise} \end{cases} \quad (7)$$

Using the relaxed threshold t_l to select the best homography H^k is required since the real motion flow is only locally approximated by planes, and removing only strong inliers by t_h for the next iteration $k+1$ guarantees smooth changes within overlapping planes and more robustness to noise. Nevertheless, in case of slow convergence or when the homography search gets stuck around a wide overlapping or noisy planar configuration, limiting the search to matches excluded by previous planes can provide a way out. The final set of homography returned is

$$\mathcal{H}^* = \mathcal{H}^{k^*} \quad (8)$$

found by the last iteration k^* when the failure counter reaches c_f^* .

3.1.3 Inside RANSAC

Within each MOP iteration k , a homography H^k is extracted by RANSAC on the match set \mathcal{M}^k . The vanilla RANSAC is modified according to the following heuristics to improve robustness and avoid degenerate cases.

A minimum number $c_{\min} = 50$ of RANSAC loop iterations is required besides the max number of iterations $c_{\max} = 2000$. In addition, a minimum hypothesis sampled model

$$\mathcal{S} = \{(\mathbf{s}_{1i}, \mathbf{s}_{2i})\} \subseteq \mathcal{M}^k, \quad 1 \leq i \leq 4 \quad (9)$$

is discarded if the distance within the keypoints in one of the images is less than the relaxed threshold

t_l , i.e. it must hold

$$\min_{\substack{1 \leq i, j \leq 4 \\ i \neq j \\ w=1,2}} \|\mathbf{s}_{wi} - \mathbf{s}_{wj}\| \geq t_l \quad (10)$$

Furthermore, being H the corresponding homography derived by the normalized 8-point algorithm [45], the smaller singular value found by solving through SVD the 8×9 homogeneous system must be relatively greater than zero for a stable solution not close to degeneracy. According to these observations, the minimum singular value is constrained to be greater than 0.05. Note that an absolute threshold is feasible since data are normalized before SVD.

Next, matches in \mathcal{S} must satisfy quasi-affinity with respect to the derived homography H . This can be verified by checking that the sign of the last coordinate of the reprojection $H\mathbf{s}_{1i}$ in non-normalized homogenous coordinates are the same for $1 \leq i \leq 4$, i.e. for all the four keypoint in the first image. This can be expressed as

$$[H\mathbf{s}_{1i}]_3 \cdot [H\mathbf{s}_{1j}]_3 = 1, \quad \forall 1 \leq i, j \leq 4 \quad (11)$$

where $[\mathbf{x}]_3$ denotes the third and last vector element of the point \mathbf{x} in non-normalized homogeneous coordinates. Following the above discussion, the quasi-affine set of matches $\mathcal{Q}_H^{\mathcal{M}}$ in Eq. 3 is formally defined as

$$\mathcal{Q}_H^{\mathcal{M}} = \{m \in \mathcal{M} : [H\mathbf{x}_1]_3 \cdot [H\mathbf{s}_{11}]_3 = 1\} \quad (12)$$

For better numerical stability, the analogous checks are executed also in the reverse direction through H_S^{-1} .

Lastly, to speed up the RANSAC search, a buffer $\mathcal{B} = \{\tilde{H}_i\}$ with $1 \leq i \leq z$ is globally maintained in order to contain the top $z = 5$ discarded sub-optimal homographies encountered within a RANSAC run. For the current match set \mathcal{M}^k if \tilde{H}_0 is the current best RANSAC model maximizing the number of inliers, $\tilde{H}_i \in \mathcal{B}$ are ordered by the number v_i of inliers excluding those compatible with the previous homographies in the buffer, i.e. it must holds that

$$v_i \geq v_{i+1} \quad (13)$$

where

$$v_i = \left| \mathcal{I}_{H_i}^{\mathcal{M}^k} \setminus \left(\bigcup_{0 \leq j < i} \mathcal{I}_{H_j}^{\mathcal{M}^k} \right) \right| \quad (14)$$

The buffer \mathcal{B} can be updated when the number of inliers of the homography associated with the current sampled hypothesis is greater than the minimum v_i , by inserting in the case the new homography, removing the low-scoring one and resorting to the buffer. Moreover, at the beginning of a RANSAC run inside a MOP iteration, the minimum hypothesis model sampling sets \mathcal{S} corresponding to homographies in \mathcal{B} are evaluated before proceeding with true random samples to provide a bootstrap for the solution search. This also guarantees a global sequential inspection of the overall solution search space within MOP.

3.1.4 Homography assignment

After the final set of homographies \mathcal{H}^* is computed, the filtered match set \mathcal{M}^* is obtained by removing all matches $m \in \mathcal{M}$ for which there is no homography H in \mathcal{H}^* having them as inlier, i.e.

$$\mathcal{M}^* = \{m \in \mathcal{M} : \exists H \in \mathcal{H}^* \ m \in \mathcal{I}_{H,t_l}^{\mathcal{M}}\} \quad (15)$$

Next, a homography must be associated with each survived match $m \in \mathcal{M}^*$, which will be used for patch normalization.

A possible choice is to assign the homography H_m^{ε} which gives the minimum reprojection error, i.e.

$$H_m^{\varepsilon} = \underset{H \in \mathcal{H}^*}{\operatorname{argmin}} \varepsilon_H(m) \quad (16)$$

However, this choice is likely to select homographies corresponding to narrow planes in the image with small consensus sets, which leads to a low reprojection error but more unstable and prone to noise assignment.

Another choice is to assign to the match m the homography $H_m^{\mathcal{I}}$ compatible with m with the wider consensus set, i.e.

$$H_m^{\mathcal{I}} = \underset{H \in \mathcal{H}^*, m \in \mathcal{I}_{H,t_l}^{\mathcal{M}^*}}{\operatorname{argmax}} |\mathcal{I}_{H,t_l}^{\mathcal{M}^*}| \quad (17)$$

which points to more stable and robust homographies but can lead to incorrect patches when the corresponding reprojection error is not among the minimum ones.

The homography H_m actually chosen for the match association provides a solution within the

above. Specifically, for a match m , defining q_m as the median of the number of inliers of the top 5 compatible homographies according to the number of inliers for t_l , H_m is the compatible homography with the minimum reprojection error among those with an inlier number at least equal to q_m

$$H_m = \underset{H \in \mathcal{H}^*, |\mathcal{I}_{H,t_l}^{\mathcal{M}^*}| \geq q_m}{\operatorname{argmin}} \varepsilon_H(m) \quad (18)$$

Figure 1 shows an example of the achieved solution directly in combination with MiHo homography estimation described hereafter in Sec. 3.2, since MOP or MOP+MiHo in visual cluster representation does not present appreciable differences. Keypoint belonging to discarded matches are marked with black diamonds, while the clusters highlighted by other combinations of markers and colors indicate the resulting filtered matches $m \in \mathcal{M}^*$ with the selected planar homography H_m . Notice that clusters are not designed to highlight scene planes but points that move according to the same homography transformation within the image pair.

3.2 Middle Homography (MiHo)

3.2.1 Rationale

The H_m homography estimated by Eq. 18 for the match $m = (\mathbf{x}_1, \mathbf{x}_2)$ allows to reproject the local patch neighborhood of $x_1 \in I_1$ onto the corresponding one centered in $\mathbf{x}_2 \in I_2$. Nevertheless, H_m approximates the true transformation within the images which becomes less accurate as long as the distance from the keypoint center increases. This implies that patch alignment could be invalid for wider, and theoretically more discriminant, patches.

The idea behind MiHo is to break the homography H_m in the middle by two homographies H_{m_1} and H_{m_2} such that $H_m = H_{m_2}H_{m_1}$ so that the patch on \mathbf{x}_1 gets deformed by H_{m_1} less than H_m , and likewise the patch on \mathbf{x}_2 gets less deformed by $H_{m_2}^{-1}$ than H_m^{-1} . This means that visually on the reprojected patch a unit area square should remain almost similar to the original one. As this must hold from both the images, the deformation error must be distributed almost equally between the two homographies H_{m_1} and H_{m_2} . Moreover, since interpolation degrades with up-sampling, MiHo aims to balance the down-sampling of the

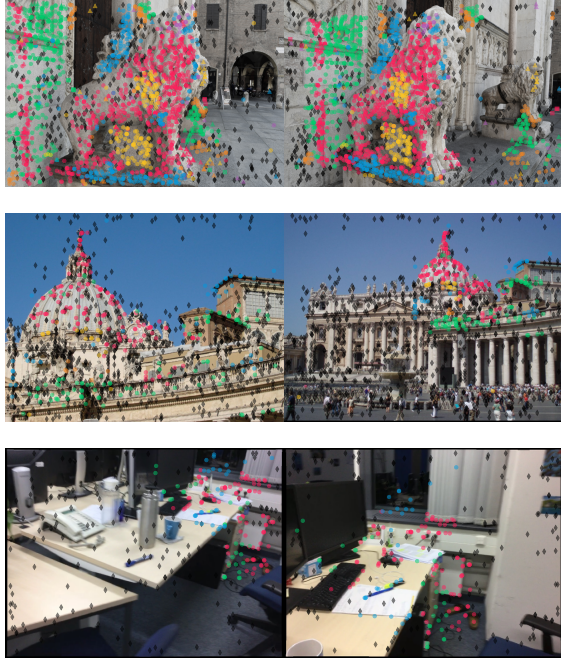


Fig. 1: MOP+MiHo clustering and filtered matches for some image pair examples. Each combination of makers and colors is associated to a unique virtual planar homography as described in Secs. 3.1-3.2, while discarded matches are indicated by black diamonds. The matching pipeline employed is the the one relying on Key.Net described in Sec 4.1.1. The images of the middle and bottom rows belong to MegaDepth and ScanNet respectively, described later in Sec. 4.1.3. Best viewed in color and zoomed in.

patch at finer resolution and the up-sampling of the patch at the coarser resolution.

3.2.2 Implementation

While a strict analytical formulation of the above problem which leads to a practical satisfying solution is not easy to derive, the heuristic found in [51] can be exploited to modify RANSAC within MOP to account for the required constraints. Specifically, each match m is replaced by two corresponding matches $m_1 = (\mathbf{x}_1, \mathbf{m})$ and $m_2 = (\mathbf{m}, \mathbf{x}_2)$ where \mathbf{m} is the midpoint within the two keypoints

$$\mathbf{m} = \frac{\mathbf{x}_1 + \mathbf{x}_2}{2} \quad (19)$$

Hence the RANSAC input match set $\mathcal{M}^k = \{m\}$ for the MOP k -th iteration is split in the two match sets $\mathcal{M}_1^k = \{m_1\}$ and $\mathcal{M}_2^k = \{m_2\}$. Within a RANSAC iteration, a sample \mathcal{S} defined by Eq. 9 is likewise split into

$$\begin{aligned} \mathcal{S}_1 &= \left\{ \left(\mathbf{s}_{1i}, \frac{\mathbf{s}_{1i} + \mathbf{s}_{2i}}{2} \right) \right\} \subseteq \mathcal{M}_1^k \\ \mathcal{S}_2 &= \left\{ \left(\frac{\mathbf{s}_{1i} + \mathbf{s}_{2i}}{2}, \mathbf{s}_{2i} \right) \right\} \subseteq \mathcal{M}_2^k, 1 \leq i \leq 4 \end{aligned} \quad (20)$$

leading to two concurrent homographies H_1 and H_2 to be verified simultaneously with the inlier set in analogous way to Eq. 3

$$\mathcal{I}_{(H_1, H_2), t}^{\mathcal{M}^k} = \left(\mathcal{J}_{H_1, t}^{\mathcal{M}_1^k} \upharpoonright \mathcal{J}_{H_2, t}^{\mathcal{M}_2^k} \right) \cap \left(\mathcal{Q}_{H_1}^{\mathcal{M}_1^k} \upharpoonright \mathcal{Q}_{H_2}^{\mathcal{M}_2^k} \right) \quad (21)$$

where for two generic match set \mathcal{M}_1 , \mathcal{M}_2 , the \upharpoonright operator rejoins splitted matches according to

$$\begin{aligned} \mathcal{M}_1 \upharpoonright \mathcal{M}_2 &= \{(\mathbf{x}_1, \mathbf{x}_2) : (\mathbf{x}_1, \mathbf{m}) \in \mathcal{M}_1 \\ &\quad \wedge (\mathbf{x}_2, \mathbf{m}) \in \mathcal{M}_2\} \end{aligned} \quad (22)$$

All the other MOP steps defined in Sec. 3.1, including RANSAC degeneracy checks, threshold adaptation, and final homography assignment, follow straightly in an analogous way. Overall, the principal difference is that a pair of homography (H_{m_1}, H_{m_2}) is obtained instead of the single H_m homography to be operated simultaneously on split match sets \mathcal{M}_1 and \mathcal{M}_2 instead of the original one \mathcal{M} .

Figure 2 shows the differences in applying MiHo to align to planar scenes with respect to directly reproject in any of the two images considered as reference. It can be noted that the distortion differences are overall reduced, as highlighted by the corresponding grid deformation. Moreover, MiHo homography strongly resembles an affine transformation or even a similarity, i.e. a rotation and scale change only, imposing in some sense a tight constraint on the transformation than the base homography. To balance this additional restrain with respect to the original MOP, in MOP+MiHo the minimum requirement amount of inliers for increasing the failure counter defined by Eq. 4 has been relaxed after experimental validation from $n = 12$ to $n = 8$.

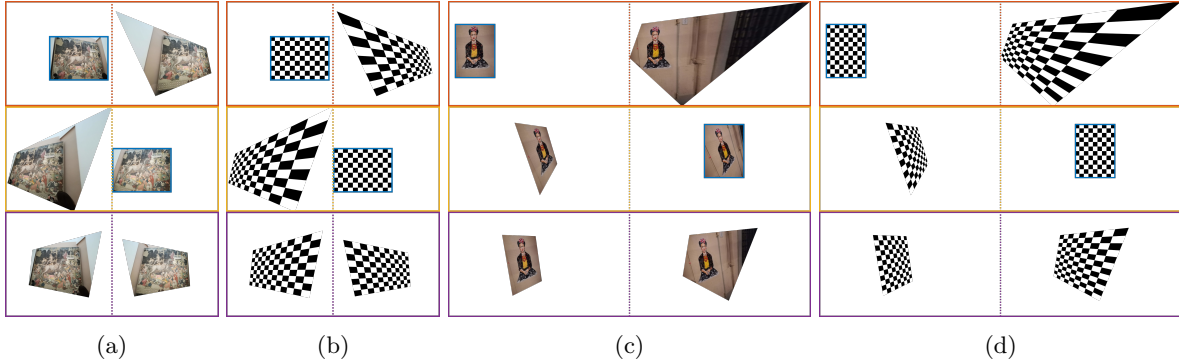


Fig. 2: Visual comparison between the standard planar homography and MiHo tied homographies as defined in Sec. 3.2.1. (a) Two corresponding images, framed in blue, are used in turn as reference in the top and middle rows while the other one is reprojected by a planar homography, show in the same row. In the case of MiHo, both images are warped as shown in the bottom row, yet the overall distortion is reduced. The local transformation is better highlighted in (b) with the related warping of the unit-square representation of the original images. (c,d) The analogous visualization for a more critical configuration with stronger relative viewpoint change. Best viewed in color and zoomed in.

3.2.3 Translation invariance

MiHo is invariant to translations as long as the algorithm used to extract the homography provides the same invariance. This can be easily verified since when translation vectors $\mathbf{t}_a, \mathbf{t}_b$ are respectively added to all keypoints $\mathbf{x}_1 \in I_1$ and $\mathbf{x}_2 \in I_2$ to get $\mathbf{x}'_1 = \mathbf{x}_1 + \mathbf{t}_a$ and $\mathbf{x}'_2 = \mathbf{x}_2 + \mathbf{t}_b$ the corresponding midpoints are of the form

$$\mathbf{m}' = \frac{\mathbf{x}'_1 + \mathbf{x}'_2}{2} = \frac{\mathbf{x}_1 + \mathbf{x}_2}{2} + \frac{\mathbf{t}_a + \mathbf{t}_b}{2} = \mathbf{m} + \mathbf{t} \quad (23)$$

where $\mathbf{t} = \frac{\mathbf{t}_a + \mathbf{t}_b}{2}$ is a fixed translation vector is added to all the corresponding original midpoints \mathbf{m} . Overall, translation keypoints in the respective images have the effect of adding a fixed translation to the corresponding midpoint. Hence MiHo is invariant to translations since the normalization employed by the normalized 8-point algorithm is invariant to similarity transformations [45], including translations.

3.2.4 Fixing rotations

MiHo is not rotation invariant. Figure 3 illustrates how midpoints change with rotations. In the ideal MiHo configuration where the images are upright the area of the image formed in the midpoint plane is within the areas of the original ones, making a single cone when considering the images as stacked. The area of the midpoint plane

is lower than the minimum area between the two images when there is a rotation about 180° , and could degenerate to the apex of the corresponding double cone. A simple strategy to get an almost-optimal configuration was experimentally verified to work well in practice under the observation that images acquired by cameras tend to have a possible relative rotation α of a multiple of 90° .

In detail, let us define a given input match $m_i = (\mathbf{x}_{1i}, \mathbf{x}_{2i}^\alpha) \in \mathcal{M}^\alpha$ and the corresponding midpoint $\mathbf{m}_i^\alpha = \frac{\mathbf{x}_{1i} + \mathbf{x}_{2i}^\alpha}{2}$, where $\mathbf{x}_{1i} \in I_1$ and $\mathbf{x}_{2i}^\alpha \in I_2^\alpha$ being the image I_2 rotated by α . One has to choose $\alpha^* \in \mathcal{A} = \{0, \frac{\pi}{2}, \pi, \frac{3\pi}{2}\}$ to maximize the configuration for which midpoint inter-distances are between corresponding keypoint inter-distances

$$\alpha^* = \underset{\substack{m_i, m_j \in \mathcal{M}^\alpha \\ \alpha \in \mathcal{A}}}{\operatorname{argmax}} \left[\left\| \mathbf{m}_i^\alpha - \mathbf{m}_j^\alpha \right\| \in \left[d_{ij}^{ij}, d_{ij}^{\uparrow} \right] \right] \quad (24)$$

where

$$\begin{aligned} d_{ij}^{ij} &= \min \left(\left\| \mathbf{x}_{1i} - \mathbf{x}_{1j} \right\|, \left\| \mathbf{x}_{2i}^\alpha - \mathbf{x}_{2j}^\alpha \right\| \right) \\ d_{ij}^{\uparrow} &= \max \left(\left\| \mathbf{x}_{1i} - \mathbf{x}_{1j} \right\|, \left\| \mathbf{x}_{2i}^\alpha - \mathbf{x}_{2j}^\alpha \right\| \right) \end{aligned} \quad (25)$$

and $\llbracket \cdot \rrbracket$ is the Iverson bracket. The global orientation estimation α^* can be computed efficiently on the initial input matches \mathcal{M} before running MOP, adjusting keypoints accordingly. Final homographies can be adjusted in turn by removing the rotation given by α^* . Figure 4 shows the

MOP+MiHo result obtained on a set of matches without or with orientation pre-processing, highlighting the better matches obtained in the latter case.

3.3 Normalized Cross Correlation (NCC)

3.3.1 Local image warping

NCC is employed to effectively refine corresponding keypoint localization. The approach assumes that corresponding keypoints have been roughly aligned locally by the transformations provided as a homography pair. In the warped aligning space, template matching [48] is employed to refine translation offsets in order to maximize the NCC peak response when the patch of a keypoint is employed as a filter onto the other image of the corresponding keypoint.

For the match $m = (\mathbf{x}_1, \mathbf{x}_2)$ within images I_1 and I_2 there can be multiple potential choices of the warping homography pair, which are denoted by the set of associated homography pairs $\mathcal{H}_m = \{(\mathbf{H}_1, \mathbf{H}_2)\}$. In detail, according to the previous steps of the matching pipeline, a candidate is the base homography pair $(\mathbf{H}_1^b, \mathbf{H}_2^b)$ defined as

- (\mathbf{I}, \mathbf{I}) , where $\mathbf{I} \in \mathbb{R}^{3 \times 3}$ is the identity matrix, when no local neighborhood data are provided, e.g. for SuperPoint;
- $(\mathbf{A}_1, \mathbf{A}_2)$, where $\mathbf{A}_1, \mathbf{A}_2 \in \mathbb{R}^{3 \times 3}$ are affine or similarity transformations in case of affine covariant detector & descriptor, as for AffNet or SIFT, respectively;

and the other is extended pair $(\mathbf{H}_1^e, \mathbf{H}_2^e)$ defined as

- $(\mathbf{I}, \mathbf{H}_m)$, where \mathbf{H}_m is defined in Eq. 18, in case MOP is used without MiHo;
- $(\mathbf{H}_{m_1}, \mathbf{H}_{m_2})$ as described in Sec. 3.2.1, in case of MOP+MiHo
- $(\mathbf{H}_1^b, \mathbf{H}_2^b)$ as above otherwise.

Since the found transformations are approximated, the extended homography pair is perturbed in practice by small shear factors f and rotation changes ρ through the affine transformations

$$\mathbf{A}_{\rho, f} = \begin{bmatrix} f \cos(\rho) & -f \sin(\rho) & 0 \\ \sin(\rho) & \cos(\rho) & 0 \\ 0 & 0 & 1 \end{bmatrix} \quad (26)$$

with

$$\rho \in \mathcal{R} = \{-\frac{\pi}{6}, -\frac{\pi}{12}, 0, \frac{\pi}{12}, \frac{\pi}{6}\} \quad (27)$$

$$f \in \mathcal{F} = \{\frac{5}{7}, \frac{5}{6}, 1, \frac{6}{5}, \frac{7}{5}\} \quad (28)$$

so that

$$\begin{aligned} \mathcal{H}_m = & \{(\mathbf{H}_1^b, \mathbf{H}_2^b)\} \\ & \cup \{(\mathbf{A}_{\rho, f} \mathbf{H}_1^e, \mathbf{H}_2^e) : (\rho, f) \in \mathcal{R} \times \mathcal{F}\} \\ & \cup \{(\mathbf{H}_1^e, \mathbf{A}_{\rho, f} \mathbf{H}_2^e) : (\rho, f) \in \mathcal{R} \times \mathcal{F}\} \end{aligned} \quad (29)$$

3.3.2 Computation

Let us denote a generic image by I , the intensity values of I for a generic pixel $\mathbf{x} \in \mathbb{R}^2$ as $I(\mathbf{x})$, the window radius extension as

$$\mathcal{W}_r = \{x \in [-r, r] \cap \mathbb{Z}\} \quad (30)$$

such that the squared window set of offsets is

$$\mathcal{W}_r^2 = \mathcal{W}_r \times \mathcal{W}_r \quad (31)$$

and has cardinality equal to

$$|\mathcal{W}_r^2| = (2w + 1)^2 \quad (32)$$

The squared patch of I centered in \mathbf{x} with radius w is the pixel set

$$\mathcal{P}_{\mathbf{x}, r}^I = \{I(\mathbf{x} + \mathbf{w}) : \mathbf{w} \in \mathcal{W}_r^2\} \quad (33)$$

while the mean intensity value of the patch $\mathcal{P}_{\mathbf{x}, r}^I$ is

$$\mu_{\mathbf{x}, r}^I = \frac{1}{|\mathcal{W}_r^2|} \sum_{\mathbf{w} \in \mathcal{W}_r^2} I(\mathbf{x} + \mathbf{w}) \quad (34)$$

and the variance is

$$\sigma_{\mathbf{x}, r}^I = \frac{1}{|\mathcal{W}_r^2|} \sum_{\mathbf{w} \in \mathcal{W}_r^2} (I(\mathbf{x} + \mathbf{w}) - \mu_{\mathbf{x}, r}^I)^2 \quad (35)$$

The normalized intensity value $\bar{I}_{\mathbf{x}, r}(\mathbf{y})$ by the mean and standard deviation of the patch $\mathbf{P}_{\mathbf{x}, r}^I$ for a pixel \mathbf{y} in I is

$$\bar{I}_{\mathbf{x}, r}(\mathbf{y}) = \frac{I(\mathbf{y}) - \mu_{\mathbf{x}, r}^I}{\sqrt{\sigma_{\mathbf{x}, r}^I}} \quad (36)$$

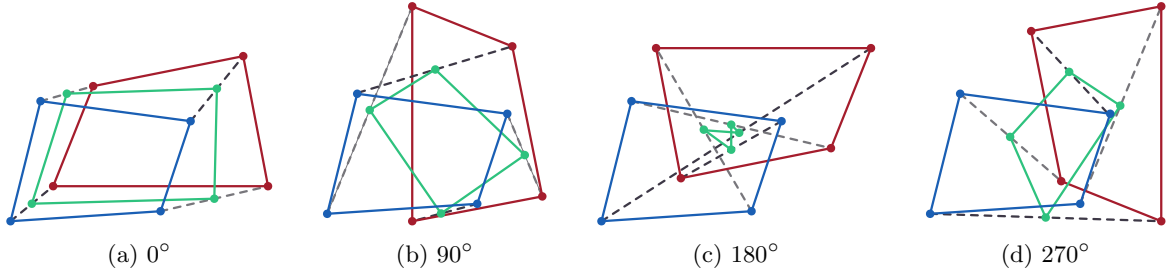


Fig. 3: Midpoints and rotations with MiHo. The blue and red quadrilaterals are linked by a homography which is defined by the four corner correspondences, indicated by dashed gray lines. The midpoints of the corner correspondences identify the reference green quadrilateral and the derived two MiHo planar homographies with the original quadrilaterals. In the optimal MiHo configuration (a) the area of the quadrilateral defined by the midpoints is maximized. Incremental relative rotations within the two original quadrilaterals by 90° decrease the above area through (b) to the minimum (c). From the minimum further rotations increase the area through (d) to the maximum again. As heuristic, in the best configuration the distance of any two midpoint corners should be within the distances of the corresponding original corners of both images as detailed in Sec. 3.2.4. Note that for the specific example, in the worst case there is also a violation of the planar orientation constraints [45]. Best viewed in color and zoomed in.

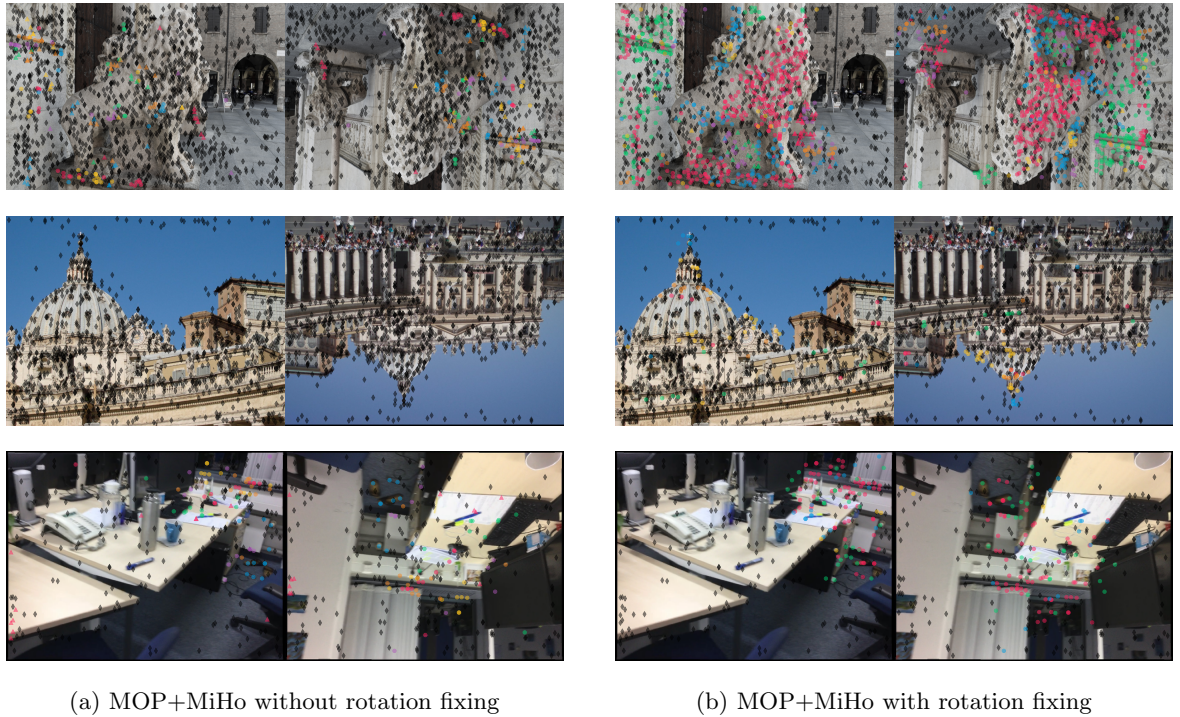


Fig. 4: MOP+MiHo visual clustering (a) without and (b) with rotation handling in the worst case of a 180° relative rotation as described in Sec. 3.2.4. The same notation and image pairs of Fig. 1 are used. Although the results with rotation handling are clearly better, these are not the same of Fig. 1 since the input matches provided by Key.Net are different as OriNet [84] has been further included in the pipeline to compute patch orientations. Notice that the base MOP obtains results similar to (b) without special needs to handle image rotations. Best viewed in color and zoomed in.

which is ideally robust to affine illumination changes [48]. Lastly, the similarity between two patches $\mathcal{P}_{\mathbf{a},r}^A$ and $\mathcal{P}_{\mathbf{b},r}^B$ is

$$S_{\mathbf{a},\mathbf{b},r}^{A,B} = \sum_{\mathbf{w} \in \mathcal{W}_r^2} \bar{A}_{\mathbf{a},r}(\mathbf{a} + \mathbf{w}) \bar{B}_{\mathbf{b},r}(\mathbf{b} + \mathbf{w}) \quad (37)$$

so that, for the match $m = (\mathbf{x}_1, \mathbf{x}_2)$ and a set of associated homography pairs \mathcal{H}_m derived in Eq. 29, the refined keypoint offsets $(\mathbf{t}_1^*, \mathbf{t}_2^*)$ and the best aligning homography pair (H_1^*, H_2^*) are given by

$$\begin{aligned} T_m^{I_1, I_2} &= ((\mathbf{t}_1^*, \mathbf{t}_2^*), (H_1^*, H_2^*)) \\ &= \underset{(\mathbf{t}_1, \mathbf{t}_2) \in \overleftrightarrow{\mathcal{W}}_r^2}{\operatorname{argmax}} \underset{(H_1, H_2) \in \mathcal{H}_m}{S_{H_1 \mathbf{x}_1 + \mathbf{t}_1, H_2 \mathbf{x}_2 + \mathbf{t}_2, r}^{H_1 \circ I_1, H_2 \circ I_2}} \end{aligned} \quad (38)$$

where $H \circ I$ means the warp of the image I by H , $H\mathbf{x}$ is the transformed pixel coordinates and

$$\overleftrightarrow{\mathcal{W}}_r^2 = (\mathbf{0} \times \mathcal{W}_r^2) \cup (\mathcal{W}_r^2 \times \mathbf{0}) \quad (39)$$

is the set of offset translation to check considering in turn one of the images as template since this is not a symmetric process. Notice that $\mathbf{t}_1^*, \mathbf{t}_2^*$ cannot be both different from $\mathbf{0}$ according to $\overleftrightarrow{\mathcal{W}}_r^2$. The final refined match

$$m^* = (\mathbf{x}_1^*, \mathbf{x}_2^*) \quad (40)$$

is obtained by reprojecting back to the original images, i.e.

$$\begin{aligned} \mathbf{x}_1^* &= H_1^{*-1} (H_1 \mathbf{x}_1 + \mathbf{t}_1^*) \\ \mathbf{x}_2^* &= H_2^{*-1} (H_2 \mathbf{x}_2 + \mathbf{t}_2^*) \end{aligned} \quad (41)$$

The normalized cross correlation can be computed efficiently by convolution, where bilinear interpolation is employed to warp images. The patch radius r is also the offset search radius and has been experimentally set to $r = 10 \approx \sqrt{2}t_h$ px. According to preliminary experiments, a wider radius extension can break the planar neighborhood assumption and patch alignment.

3.3.3 Sub-pixel precision

The refinement offset can be further enhanced by parabolic interpolation adding sub-pixel precision [102]. Notice that other forms of interpolations have been investigated but they did not provide any sub-pixel accuracy improvements according to previous experiments [49]. The NCC response map at $\mathbf{u} \in \mathbb{R}^2$ in the best warped space with origin the peak value can be written as

$$S_m^*(\mathbf{u}) = S_{H_1^* \mathbf{x}_1 + \mathbf{t}_1^* + \mathbf{u}, H_2^* \mathbf{x}_2 + \mathbf{t}_2^* + \mathbf{u}, r}^{H_1^* \circ I_1, H_2^* \circ I_2} \quad (42)$$

from $T_m^{I_1, I_2}$ computed by Eq. 38. The sub-pixel refinement offsets in the horizontal direction are computed as the vertex $-\frac{b}{2a}$ of a parabola $ax^2 + bx + c = y$ fitted on the horizontal neighborhood centered in the peak of the maximized NNC response map, i.e.

$$\begin{aligned} a &= \frac{S_m^*([1]) - 2S_m^*([0]) + S_m^*([-1])}{2} \\ b &= \frac{S_m^*([1]) - S_m^*([-1])}{2} \end{aligned} \quad (43)$$

and analogously for the vertical offsets. Explicitly the sub-pixel refinement offset is $\mathbf{p} = \begin{bmatrix} p_x \\ p_y \end{bmatrix}$ where

$$\begin{aligned} p_x &= \frac{S_m^*([-1]) - S_m^*([1])}{2(S_m^*([1]) - 2S_m^*([0]) + S_m^*([-1]))} \\ p_y &= \frac{S_m^*([-1]) - S_m^*([1])}{2(S_m^*([1]) - 2S_m^*([0]) + S_m^*([-1]))} \end{aligned} \quad (44)$$

and from Eq. 41 the final refined match

$$m^{**} = (\mathbf{x}_1^{**}, \mathbf{x}_2^{**}) \quad (45)$$

becomes

$$\begin{aligned} \mathbf{x}_1^{**} &= H_1^{*-1} (H_1 \mathbf{x}_1 + \mathbf{t}_1^* + \llbracket \mathbf{t}_1^* \neq \mathbf{0} \rrbracket \mathbf{p}) \\ \mathbf{x}_2^{**} &= H_2^{*-1} (H_2 \mathbf{x}_2 + \mathbf{t}_2^* + \llbracket \mathbf{t}_2^* \neq \mathbf{0} \rrbracket \mathbf{p}) \end{aligned} \quad (46)$$

where the Iverson bracket zeroes the sub-pixel offset increment \mathbf{p} in the reference image according to Eq. 39.

4 Evaluation

4.1 Setup

To ease the reading, each pipeline module or error measure that will be included in the results is highlighted in bold.

4.1.1 Base pipelines

Seven base pipelines have been tested to provide the input matches to be filtered. For each of these, the maximum number of keypoints was set to 8000 to retain as many as possible matches. This leads to including more outliers and better assessing the filtering potential. Moreover, nowadays benchmarks and deep matching architecture designs assume upright image pairs, where the relative orientation between images is roughly no more than $\frac{\pi}{8}$. This additional constraint allows us to retrieve better initial matches in common user acquisition scenarios. Current general standard benchmark datasets, including those employed in this evaluation, are built so that the image pairs do not violate this constraint. Notice that many SOTA joint and end-to-end deep architectures do not tolerate strong rotations within images by design.

SIFT+NNR [19] is included as the standard and reference handcrafted pipeline. The OpenCV [103] implementation was used for SIFT, exploiting RootSIFT [104] for descriptor normalization, while NNR implementation is provided by Kornia [105]. To stress the match filtering robustness of the successive steps of the matching pipeline, which is the goal of this evaluation, the NNR ratio threshold was set rather high, i.e. to 0.95, while common adopted values range in [0.7, 0.9] depending on the scene complexity, with higher values yielding to less discriminative matches and then possible outliers. Moreover, upright patches are employed by zeroing the dominant orientation for a fair comparison with other recent deep approaches.

Key.Net+^{AffNet}_{HardNet}+NNR [11], a modular pipeline that achieves good results in common benchmarks, is also taken into account. Excluding the NNR stage, it can be considered a modular deep pipeline. The Kornia implementation is used for the evaluation. As for SIFT, the NNR threshold is set very high, i.e. to 0.99, while more common values range in [0.8, 0.95]. The deep orientation estimation module OriNet [84] generally

siding AffNet is not included to provide upright matches.

Other base pipelines considered are SOTA full end-to-end matching networks. In details, these are **SuperPoint+LightGlue**, **DISK+LightGlue** and **ALIKED+LightGlue** as implemented in [12]. The input images are rescaled so the smaller size is 1024 following LightGlue default. For ALIKED the `aliked-n16rot` model weights are employed which according to the authors [13] can handle slight image rotation better and are more stable on viewpoint change.

The last base pipelines added in the evaluation are **DeDoDe v2** [93], which provides an alternative end-to-end deep architecture different from the above, and **LoFTR**, a semi-dense detector-free end-to-end network. These latter pipelines also achieve SOTA results in popular benchmarks. The authors' implementation is employed for DeDoDe v2, setting to matching threshold to 0.01, while LoFTR implementation available through Kornia is used in the latter case.

4.1.2 Match filtering and post-processing

Eleven match filters are applied after the base pipelines and included in the evaluation besides MOP+MiHo+NCC. For the proposed filtering sub-pipeline, all the five available combinations have been tested, i.e. **MOP**, **MOP+NCC**, **NCC**, **MOP+MiHo**, **MOP+MiHo+NCC**, to analyze the behavior of each module. In particular, applying NCC after SIFT+NNR or Key.Net+^{AffNet}_{HardNet}+NNR can highlight the improvement introduced by MOP which uses homography-based patch normalization against similarity or affine patches, respectively. Likewise, applying NCC to the remaining end-to-end architectures should remark the importance of patch normalization. The setup parameters indicated in Sec. 3 is employed, which has worked well in preliminary experiments. Notice that MiHo orientation adjustment described in Sec. 3.2.4 is applied although not required in the case of upright images. This allows us to indirectly assess the correctness of base assumptions and the overall general method robustness since in the case of wrong orientation estimation the consequential failure can only decrease the match quality.

To provide a fair and general comparison, the analysis was restricted to filters that require as input only the keypoint positions of the matches and the image pair. This excludes approaches requiring in addition descriptor similarities [25, 27, 28], related patch transformations [71], intermediate network representations [42, 43] or a SfM framework [101]. The compared methods are **GMS** [26], **AdaLAM** [33] and **CC** [79] as handcrafted filters, and **ACNe** [35], **CLNet** [37], **ConvMatch** [40], **DeMatch** [41], **FC-GNN** [44], **MS²DG-Net** [39], **NCM-Net** [38] and **OANet** [36] as deep modules. The implementations from the respective authors have been employed for all filters with the default setup parameters if not stated otherwise. Except FC-GNN and OANet, deep filters require as input the intrinsic camera matrices of the two images, which is not commonly available in real practical scenarios the proposed evaluation was designed for. To bypass this restriction, the approach presented in ACNe was employed, for which the intrinsic camera matrix

$$K = \begin{bmatrix} f & 0 & c_x \\ 0 & f & c_y \\ 0 & 0 & 1 \end{bmatrix} \quad (47)$$

for the image I with a resolution of $w \times h$ pixel is estimated by setting the focal length to

$$f = \max(h, w) \quad (48)$$

and the camera centre as

$$\mathbf{c} = \begin{bmatrix} c_x \\ c_y \end{bmatrix} = \frac{1}{2} \begin{bmatrix} w \\ h \end{bmatrix} \quad (49)$$

The above focal length estimation f is quite reasonable by the statistics reported in Fig. 5 that have been extracted from the evaluation data and discussed in Sec. 4.1.3. Notice also that most of the deep filters have been trained on SIFT matches, yet to be robust and generalizable they must be able to mainly depend only on the scene and not on the kind of feature extracted by the pipeline.

For AdaLAM, no initial seeds or local similarity or affine clues were used as additional input as discussed above. Nevertheless, this kind of data could have been used only for SIFT+NNR or KeyNet+^{AffNet}_{HardNet}+NNR. For CC, the inliers

threshold was experimental set to $t_h = 7$ px as in Sec. 3.1.2 instead of the value 1.5 px. suggested by authors. Otherwise, CC would not be able to work in general scenes with no planes. Note that AdaLAM and CC are the closest approaches to the proposed MOP+MiHo filtering pipeline. Moreover, among the compared methods, only FC-GNN is able to refine matches as MOP+MiHo+NCC does.

RANSAC is also optionally evaluated as the final post-process to filtering matches according to epipolar or planar constraints. Three different RANSAC implementations were initially considered, i.e. the RANSAC implementation in PoseLib³, DegenSAC⁴ [24] and MAGSAC⁵ [23]. The maximum number of iterations for all RANSACs is set to 10^5 , which is uncommonly high, to provide a more robust pose estimation and to make the whole pipeline only depend on the previous filtering and refinement stages. Five different inlier threshold values t_{SAC} , i.e.

$$t_{SAC} \in \{0.5 \text{ px}, 0.75 \text{ px}, 1 \text{ px}, 3 \text{ px}, 5 \text{ px}\} \quad (50)$$

are considered. After a preliminary RANSAC ablation study⁶ according to proposed benchmark, the best general choice found is MAGSAC with 0.75 px. or 1 px. as inlier threshold t_{SAC} , indicated by **MAGSAC**_↓ and **MAGSAC**_↑ respectively. On one hand, the former and more strict threshold is generally slightly better in terms of accuracy. On the other hand, the latter provides more inliers, so both results will be presented. Matching outputs **without RANSAC** are also reported for a complete analysis.

4.1.3 Datasets

Four different datasets have been employed in the evaluation. These include the **MegaDepth** [54] and **ScanNet** [55] datasets, respectively outdoor and indoor. The same 1500 image pairs for each dataset and Ground-Truth (GT) data indicated in the protocol employed in [14] are used. These datasets are de-facto standard in nowadays image matching benchmarking; sample image pairs for each dataset are shown in Fig. 1. MegaDepth test

³<https://github.com/PoseLib/PoseLib>

⁴<https://github.com/ducha-aiki/pydegensac>

⁵<https://github.com/danini/magsac>

⁶<https://github.com/fb82/MiHo/tree/main/data/results>

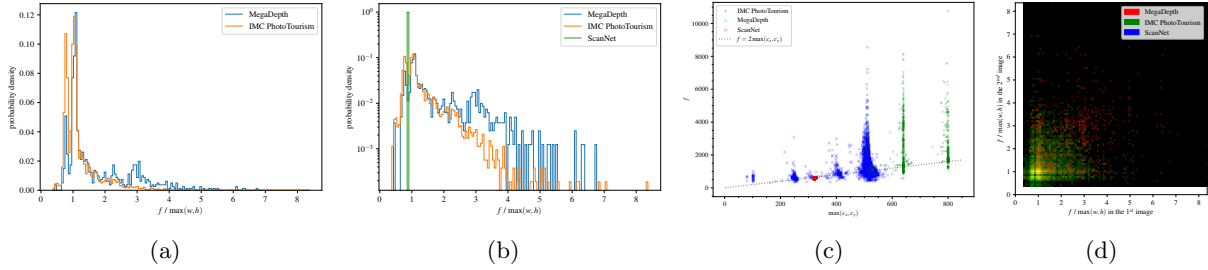


Fig. 5: (a) Probability distribution of the ratio between the GT focal length f and the maximum image dimension $\max(h, w)$ in the non-planar outdoor MegaDepth and IMC PhotoTourism datasets introduced in Sec. 4.1.3. (b) The difference between the outdoor data with respect to the indoor ScanNet dataset, also presented in Sec. 4.1.3, is shown in a logarithmic scale for a more effective visual comparison. For the indoor scenes, the ratio is fixed to 0.9 as images have been acquired by the same iPad Air2 device [55]. For the outdoor data, images have been acquired by different cameras and the ratio values cluster roughly around 1. As a heuristic derived by inspecting the images, the ratio is roughly equal to the zooming factor employed for acquiring the image. (c) Analogous representation as a scatter plot in terms of the GT camera center $[c_x \ c_y]^T$ corroborates previous histograms and the intrinsic camera approximation heuristic used in the experiments described in Sec. 4.1.2. (d) The 2D distribution of the ratios for the image pairs employed in the evaluation as an overlay in RGB color channels. Notice that the distribution overlap of the outdoor datasets with the corresponding indoor dataset is almost null, as one can check in (b) and by inspecting the cross shape in the bottom left side of (d). Best viewed in color and zoomed in.

image pairs belong to only 2 different scenes and are resized proportionally so that the maximum size is equal to 1200 px, while ScanNet image pairs belong to 100 different scenes and are resized to 640×480 px. Although according to previous evaluation [12] LightGlue provides better results when the images are rescaled so that the maximum dimension is 1600 px, in this evaluation the original 1200 px resize was maintained since more outliers and minor keypoint precision are achieved in the latter case, providing a configuration in which the filtering and refinement of the matches can be better revealed. For deep methods, the best weights that fit the kind of scene, i.e. indoor or outdoor, are used when available.

To provide further insight into the case of outdoor scenes the Image Matching Challenge (IMC) PhotoTourism dataset⁷ is also employed. The **IMC PhotoTourism (IMC-PT)** dataset is a curated collection of sixteen scenes derived by the SfM models of the Yahoo Flickr Creative Commons 100 Million (YFCC100M) dataset [106]. For each scene 800 image pairs have been randomly chosen, resulting in a total of 12800 image

pairs. These scenes also provide 3D model scale as GT data so that metric evaluations are possible. Note that MegaDepth data are is roughly a subset of IMC-PT. Furthermore, YFCC100M has been often exploited to train deep image matching methods so it can be assumed that some of the compared deep filters are advantaged on this dataset, but this information cannot be retrieved or elaborated. Nevertheless, the proposed modules are handcrafted and not positively biased so the comparison is still valid for the main aim of the evaluation.

Lastly, the **Planar** dataset contains 135 image pairs from 35 scenes collected from HPatches [56], the Extreme View dataset (EVD) [57] and further datasets aggregated from [32, 50, 70]. Each scene usually includes five image pairs except those belonging to EVD consisting of a single image pair. The planar dataset includes scenes with challenging viewpoint changes possibly paired with strong illumination variations. All image pairs are adjusted to be roughly non-upright. Outdoor model weights are preferred for deep modules in the case of planar scenes. A thumbnail gallery for the scenes of the Planar dataset is shown in Fig. 6.

⁷ <https://www.kaggle.com/competitions/image-matching-challenge-2022/data>

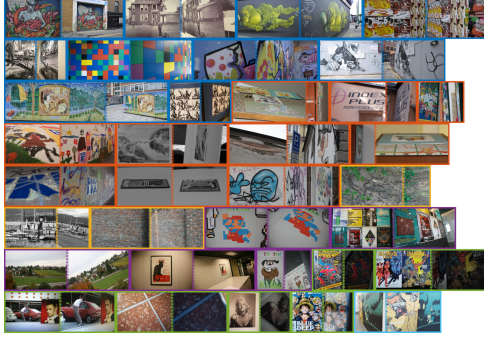


Fig. 6: Examples of image pair for each scene in the planar dataset introduced in Sec. 4.1.3. Frame colors refer in order to the original dataset of the scene: HPatches [56], EVD [57], Oxford [70], [32] and [50]. Best viewed in color and zoomed in.

4.1.4 Error metrics

For non-planar datasets, unlike most common benchmarks [14], it is assumed that no GT camera intrinsic parameters are available. This is the general setting that occurs in most practical SfM scenarios, especially in outdoor environments. For a given image pair, the fundamental matrix F can be estimated as

$$F = K_2^{-T} E K_1^{-1} = K_2^{-T} [t]_{\times} R K_1^{-1} \quad (51)$$

where $E, R, K_1, K_2, [t]_{\times} \in \mathbb{R}^{3 \times 3}$ are respectively the essential matrix, the rotation matrix, the intrinsic camera matrices and the skew-symmetric matrix corresponding to the translation vector $t \in \mathbb{R}^3$ [45]. The maximum epipolar error for a match $m = (\mathbf{x}_1, \mathbf{x}_2)$ according to F is

$$\varepsilon_F(m) = \max \left(\frac{\mathbf{x}_2^T F \mathbf{x}_1}{\| [F \mathbf{x}_1]_{[1:2]} \|^2}, \frac{\mathbf{x}_1^T F^T \mathbf{x}_2}{\| [F^T \mathbf{x}_2]_{[1:2]} \|^2} \right) \quad (52)$$

where $[\mathbf{x}]_{[1:2]}$ denotes the vector obtained by the first two elements of \mathbf{x} . In the case of planar images, the reprojection error $\varepsilon_H(m)$ defined in Eq. 1 will be used instead.

Given a set of matches $\mathcal{M}_b = \{m\}$ obtained by a base pipeline of those presented in Sec. 4.1.1 and the final refined match set \mathcal{M} according to one of the successive post-processing listed in Sec. 4.1.2, the GT fundamental matrix \tilde{F} is estimated according to Eq. 51 from the GT intrinsic

and extrinsic camera parameters⁸ in the case of the non-planar scene, or the GT homography \tilde{H} is provided for planar scenes. The notation \tilde{F}/\tilde{H} indicates the usage of the GT matrix according to the scene kind. The **recall** is computed as

$$\text{recall}_{\tilde{F}/\tilde{H}}^{\mathcal{M}_b}(\mathcal{M}) = \frac{\sum_{\substack{m \in \mathcal{M} \\ t \in \mathcal{T}}} [\varepsilon_{\tilde{F}/\tilde{H}}(m) < t]}{\sum_{\substack{m' \in \mathcal{M}_b \\ t' \in \mathcal{T}}} [\varepsilon_{\tilde{F}/\tilde{H}}(m') < t']} \quad (53)$$

and the **precision** as

$$\text{precision}_{\tilde{F}/\tilde{H}}(\mathcal{M}) = \frac{1}{|\mathcal{M}| |\mathcal{T}|} \sum_{\substack{m \in \mathcal{M} \\ t \in \mathcal{T}}} [\varepsilon_{\tilde{F}/\tilde{H}}(m) < t] \quad (54)$$

where the common definitions have been modified following the MAGSAC strategy to consider a set of threshold values

$$\mathcal{T} = \{t \in [1, t_{\varepsilon}] \cap \mathbb{Z}\} \quad (55)$$

limited by $t_{\varepsilon} = 16$. As additional statistic measurement the number of **filtered** matches is computed as

$$\text{filtered}_{\mathcal{M}_b}(\mathcal{M}) = 1 - \frac{|\mathcal{M}|}{|\mathcal{M}_b|} \quad (56)$$

For a zero denominator in Eq. 53 the recall is forced to 0. Notice that in the case of a nonzero denominator, the recall is less than or equal to 1 only when $\mathcal{M} \subseteq \mathcal{M}_b$ which does not hold for pipelines where the keypoint refinement step effectively improves the matches. The number of filtered matches and the precision are less than or equal to 1 in any case by pipeline design. The final aggregated measurement for each error and dataset is provided by averaging on all dataset image pairs. It should be remarked that for non-planar scenes both precision and recall are non-perfect measures since epipolar error constraints can hold also for outliers in specific and common scene configurations [32].

To provide more reliable measures also in view of the final aim of the image matching, the relative pose error is employed for the non-planar scenes. Two alternative estimations of the

⁸actually these are quasi or pseudo GT data estimated from wide and reliable SfM models.

pose are given in terms of rotation and translation matrices. In the first one, the fundamental matrix is estimated from the matches in \mathcal{M} by the 8-point algorithm using the normalized Direct Linear Transformation (DLT) [45] by the OpenCV function `findFundamentalMat` as $\mathbf{F}_{\mathcal{M}}$ and then the essential matrix is obtained as

$$\mathbf{E}_{\mathcal{M}} = \tilde{\mathbf{K}}_2^T \mathbf{F}_{\mathcal{M}} \tilde{\mathbf{K}}_1 \quad (57)$$

given the GT intrinsic cameras $\tilde{\mathbf{K}}_1$ and $\tilde{\mathbf{K}}_2$. The four possible choice of camera rotation and translation pairs are then obtained by SVD decomposition [45] using the OpenCV `decomposeEssentialMat` function as

$$\mathcal{E}_{\mathcal{M}} = \{\mathbf{R}_{\mathcal{M}}^1, \mathbf{R}_{\mathcal{M}}^2\} \times \{\pm \mathbf{t}_{\mathcal{M}}\} \quad (58)$$

The second alternative follows the standard benchmarks. After having normalized keypoint matches according to the GT intrinsic cameras $\tilde{\mathbf{K}}_1$ and $\tilde{\mathbf{K}}_2$ so that

$$\widehat{\mathcal{M}} = \left\{ \left(\tilde{\mathbf{K}}_1 \mathbf{x}_1, \tilde{\mathbf{K}}_2 \mathbf{x}_2 \right) : (\mathbf{x}_1, \mathbf{x}_2) \in \mathcal{M} \right\} \quad (59)$$

the essential matrix is computed directly as $\mathbf{E}_{\widehat{\mathcal{M}}}$ by the OpenCV function `findEssentialMat` using the 5-point algorithm [107] embedded into RANSAC with a normalized threshold $t_E = 0.5$ [14] and the maximum number of iteration equal to 10^4 . The two possible solutions for the camera rotation and translation components are recovered by the OpenCV function `recoverPose` as

$$\mathcal{E}_{\widehat{\mathcal{M}}} = \{\mathbf{R}_{\widehat{\mathcal{M}}}\} \times \{\pm \mathbf{t}_{\widehat{\mathcal{M}}}\} \quad (60)$$

Notice that this second approach makes it easier to find a correct solution since five points are required instead of eight for the minimum model and $\tilde{\mathbf{K}}_1$ and $\tilde{\mathbf{K}}_2$ are used earlier stage of the process. Nevertheless, these conditions are more unlikely to be met in practical real situations, especially in outdoor environments. Notice that the translation vectors in both $\mathcal{E}_{\mathcal{M}}$ and $\mathcal{E}_{\widehat{\mathcal{M}}}$ are defined up to scale. The final pose accuracy is provided in terms of the Area Under the Curve (AUC) of the best maximum angular error estimation for each dataset image pair and a given angular threshold

$$\theta \in \{5^\circ, 10^\circ, 20^\circ\} \quad (61)$$

The maximum angular error for an image pair is

$$\rho(\mathcal{M}) = \min_{(\mathbf{R}, \mathbf{t}) \in \mathcal{E}_{\mathcal{M}} / \mathcal{E}_{\widehat{\mathcal{M}}}} \max \left(\rho(\tilde{\mathbf{t}}, \mathbf{t}), \rho(\tilde{\mathbf{R}}, \mathbf{R}) \right) \quad (62)$$

with $\mathcal{E}_{\mathcal{M}} / \mathcal{E}_{\widehat{\mathcal{M}}}$ indicating the use of one of the two options between Eq. 58 and Eq. 60 for the estimated pose components, $\tilde{\mathbf{t}}$ and $\tilde{\mathbf{R}}$ being the respective GT translation, defined again up to scale, and rotation. In the above formula, the angular error for the translation and rotation are respectively computed as

$$\rho(\tilde{\mathbf{t}}, \mathbf{t}) = \text{acos} \left(\frac{\tilde{\mathbf{t}}^T \mathbf{t}}{\|\tilde{\mathbf{t}}\| \|\mathbf{t}\|} \right) \quad (63)$$

$$\rho(\tilde{\mathbf{R}}, \mathbf{R}) = \text{acos} \left(\frac{1}{2} \left(1 - \cos \left(\tilde{\mathbf{R}}^T \mathbf{R} \right) \right) \right) \quad (64)$$

The two obtained AUC values for the chosen pose estimation between Eq. 58 and Eq. 60 and a fixed threshold θ will be denoted by AUC_{θ}^F , AUC_{θ}^E respectively, with the superscript indicating the kind of error estimator employed, i.e. ‘ F ’ for fundamental matrix as in Eq. 58, ‘ E ’ for essential matrix as in Eq. 60. The final aggregated pose accuracy measures are their average over the θ values, indicated as AUC_{\angle}^F and AUC_{\angle}^E , where the subscript ‘ \angle ’ refers to the use of an angular translation error according to Eq. 63 to differentiate with respect to the metric translation error introduced hereafter.

In the case of IMC-PT dataset, a fully metric estimation of the translation component of the pose is possible since the real GT reconstruction scale is available, i.e. $\|\tilde{\mathbf{t}}\|$ is the real metric measurement. Inspired by the IMC 2022 benchmark⁷, Eq. 63 can be replaced by

$$\rho^+(\tilde{\mathbf{t}}, \mathbf{t}) = z \left\| \tilde{\mathbf{t}} - \|\tilde{\mathbf{t}}\| \frac{\mathbf{t}}{\|\mathbf{t}\|} \right\| \quad (65)$$

so that both the unit vectors are rescaled according to the GT baseline length $\|\tilde{\mathbf{t}}\|$. The fixed factor $z = 10$ is used to translate errors from meters to angles when directly plugging ρ^+ into Eq. 62 instead of ρ in the AUC calculation. This corresponds to replace the angular thresholds θ of Eq. 61 implicitly by pairs of thresholds

$$(\theta, t_+) \in \{(5^\circ, 0.5 \text{ m}), (10^\circ, 1 \text{ m}), (20^\circ, 2 \text{ m})\} \quad (66)$$

The translation thresholds t_+ are reasonable since the 3D scene extensions are roughly of the order of 100 m. This metric pose accuracy estimation provides a reasonable choice able to discriminate when the real baseline is negligible with respect to the whole scene so that the viewpoint change appears as rotation only. In this case, the translation angular component can be quite high as noise but it does not affect the pose estimation effectively. Using Eq. 63 would stress this error without a real justification [108]. Likewise above, the corresponding AUC values for the chosen pose estimation between Eq. 58 and Eq. 60 will be denoted by $\text{AUC}_{\text{@}(\theta, t_+)}^F$, $\text{AUC}_{\text{@}(\theta, t_+)}^E$ respectively, for the given threshold pair (θ, t_+) . The final metric accuracy scores are given by the average over the (θ, t_+) value pairs and indicated AUC_{\square}^F and AUC_{\square}^E , respectively, where the ‘ \square ’ subscript indicates the metric translation error according to Eq. 65.

For the planar dataset, the homography accuracy is measured analogously by AUC. The pose error is replaced by the maximum of the average reprojection error in the common area when using one of the two images as a reference. In detail, assuming that both images have the same resolution of $w \times h$ px., the shared pixel sets for each image are respectively

$$\mathcal{X}_{1 \rightarrow 2} = \left\{ \mathbf{x} \in \mathbb{Z}^2 : \tilde{\mathbf{H}}\mathbf{x} \in [1, w] \times [1, h] \right\} \quad (67)$$

$$\mathcal{X}_{2 \rightarrow 1} = \left\{ \mathbf{x} \in \mathbb{Z}^2 : \tilde{\mathbf{H}}^{-1}\mathbf{x} \in [1, w] \times [1, h] \right\} \quad (68)$$

where $\tilde{\mathbf{H}}$ is the GT homography matrix. The homography estimated by the OpenCV function `findHomography` from the pipeline matches is denoted as $\mathbf{H}_{\mathcal{M}}$ and the maximum average reprojection error is given by

$$\pi(\mathcal{M}) = \max \left(\pi_{\mathcal{X}_{1 \rightarrow 2}}^{\mathbf{H}_{\mathcal{M}}, \tilde{\mathbf{H}}}, \pi_{\mathcal{X}_{2 \rightarrow 1}}^{\mathbf{H}_{\mathcal{M}}^{-1}, \tilde{\mathbf{H}}^{-1}} \right) \quad (69)$$

where the average reprojection error in a single image is estimated as

$$\pi_{\mathcal{X}}^{\mathbf{H}_1, \mathbf{H}_2} = \frac{1}{|\mathcal{X}|} \sum_{\mathbf{x} \in \mathcal{X}} \|\mathbf{H}_1\mathbf{x} - \mathbf{H}_2\mathbf{x}\| \quad (70)$$

The AUC of the maximum average reprojection error in the common area for each image pair in

the dataset and a fixed angular threshold

$$t_{\text{H}} \in \{5 \text{ px}, 10 \text{ px}, 15 \text{ px}\} \quad (71)$$

is denoted by $\text{AUC}_{\text{@}t_{\text{H}}}^H$. The final homography accuracy is provided as the mean AUC over the different thresholds and is indicated by AUC_{\square}^H to be consistent with the previous AUC notation adopted in the case of non-planar images, where the superscript ‘ H ’ clearly stands for homography. Accuracy estimation considering the common area is more reliable than an accuracy estimation by averaging the reprojection error only in the four image corners as in [14]. This can be understood by observing that the GT planar homography is a pseudo GT estimated from correspondences, which lie inside the boundaries of both images. As an image point gets reprojected in the other image outside and far from the boundaries, which generally happens with the image corners as depicted in Fig. 2, there is no way to check the real error, which also increases going away from the key-point matches being employed to estimate the GT homography.

4.2 Results

4.2.1 Prelude

Tables 1-7 report the results obtained according to the setup presented in Sec. 4.1 for the different base pipelines. The left aligned shift in the pipeline column indicates incremental inclusions of the modules as in the folder-tree style visualization. All the values in the tables are expressed in percentages. Extended tables including AUCs values in the non-aggregated form, i.e. for the different thresholds, are reported as online resources⁶. In any case, non-aggregated AUC ranks are almost stable and well correlated with the corresponding aggregated measure.

The proposed pipeline modules are in bold. For the other numeric columns, the three highest values are also in bold, with the displayed bars normalized within the minimum and maximum value of the column. Increasing color shades of the bars identify the value range among the four incremental percentage intervals with exponentially decreasing length contained in $[0, 50, 75, 82.5, 100]\%$ after the value has been normalized by the minimum and maximum of

each column. Darker shades indicate exponentially better ranks.

In the next discussion, the base pipelines will be referred to for brevity by the first component, e.g. Key.Net will refer to Key.Net+^{AffNet}_{HardNet}+NNR. CC filtering was not evaluated on IMC-PT since it experienced a high number of unreasonable crashes for this dataset.

Referring to the tables, pose estimation from the fundamental matrix is harder than that from the essential matrix. This can be observed by the value differences in the sided green and yellow columns. Moreover, using MAGSAC before RANSAC-based essential matrix estimation in general does not affect or even slightly decreases the accuracy. According to these observations, the behavior of the different matching filters is stressed when the pose is estimated from the fundamental matrix. For IMC-PT the corresponding angular (green and yellow columns) and metric (purple and olive green columns) AUC scores maintain the same relative order even if metric scores are lower in terms of absolute value, thus highlighting that real pose solution is still far to be solved.

The previous observations are further confirmed by the analysis of the correlation within the employed error measures, reported in Table 8 for each dataset. On one hand, after the MAGSAC geometric constraints, for both planar and non-planar scenes there is a high correlation within recall, pose estimation accuracy as AUC, regardless of the estimation is derived from the fundamental or essential matrix, respectively indicated by the ‘*F*’ and ‘*E*’ superscripts, and these both are highly anti-correlated with the percentage of filtered matches. On the other hand, without MAGSAC in the non-planar scenes the recall and the pose accuracy estimated by the essential matrix are highly correlated and both strongly anti-correlated with the number of filtered matches, while precision has an almost moderate correlation with the pose accuracy estimated from the fundamental matrix only. Metric and angular AUC for the same kind of pose estimation have also high correlation levels. For the planar case, without MAGSAC the pose accuracy is only moderately correlated with both precision and recall, as well as anti-correlated with the percentages of the filtered matches within a similar degree.

For the sake of completeness, Table 9 reports the average number of input matches for each base method and dataset under evaluation. This information can be used together with the percentage of filtered matches to get an absolute estimation of the filtered matches. According to the reported values, SuperPoint and ALIKED provide the lower number of matches followed by SIFT and Key.Net, while DISK, LoFTR and DeDoDe v2 the highest number.

To summarize, it is better to have more matches for pose registration even with higher levels of outlier contamination when the camera intrinsic parameters are available, the opposite holds when camera parameters are missing. Moreover, RANSAC flattens scores and strongly influences the final matches. Nevertheless, one error measure cannot replace another, although highly correlated, since they highlight different properties and behaviors of the matching pipeline.

4.2.2 SIFT+NNR

Table 1 reports the results for SIFT. MOP+MiHo obtains the best pose estimation on Megadepth when this is computed from the essential matrix (AUC_{\angle}^E , yellow column), while adding NCC slightly decreases the accuracy. MOP-based filters, FC-GNN, and ACNe pose estimation are more accurate than the base SIFT even if the improvement is incremental. Other matching filters yield minimal degradation of the base accuracy in this specific setup. When the pose is derived from the fundamental matrix (AUC_{\angle}^F , green column), FC-GNN attains the highest score followed by MOP, which is almost unaltered by MiHo and again negatively altered by NCC. The improvement with respect to the base SIFT is more evident for AUC_{\angle}^F than for AUC_{\angle}^E . All filters generally improve on SIFT considering AUC_{\angle}^F , but only MOP-base filters, FC-GG, ACNe, and CC are really remarkable in terms of the accuracy gain. This behavior is also reflected in the recall (red column) and precision (blue column). In particular, MOP+MiHo seems to provide a better recall and FC-GNN more precision, where the recall is more correlated with AUC_{\angle}^E and the precision with AUC_{\angle}^F as discussed in Sec. 4.2.1.

Similar considerations hold for ScanNet even if the absolute scores are lower due to a major scene complexity, yet NCC improves MOP+MiHo

Table 1: SIFT+NNR pipeline evaluation results. All values are percentages, please refer to Sec. 4.2.2. Best viewed in color and zoomed in.

Pipeline	MegaDepth					ScanNet					Planar					IMC Photo/Tourism						
	Filtered	Precision	Recall	AUC $_{\square}^F$	AUC $_{\square}^E$	Filtered	Precision	Recall	AUC $_{\square}^F$	AUC $_{\square}^E$	Filtered	Precision	Recall	AUC $_{\square}^H$	Filtered	Precision	Recall	AUC $_{\square}^F$	AUC $_{\square}^E$	AUC $_{\square}^F$	AUC $_{\square}^E$	
SIFT+NNR	0.00	53.52	100.00	0.30	61.47	0.00	25.21	99.12	0.15	20.42	0.00	44.38	99.42	22.88	0.00	39.31	99.04	0.21	56.57	0.26	31.24	
+MAGSAC $_{\top}$	51.10	93.20	56.00	44.29	61.92	78.15	53.30	46.02	14.43	22.54	69.07	13.35	50.94	48.19	63.48	83.04	76.51	33.21	57.97	17.07	31.28	
+MAGSAC $_{\perp}$	54.52	93.83	79.32	46.86	62.20	80.84	55.24	49.60	14.74	22.36	75.34	75.43	39.88	45.12	66.19	85.60	70.76	34.08	57.33	18.43	30.84	
+ACNe	47.98	92.51	90.88	29.25	62.56	67.72	55.42	71.03	12.71	25.73	54.05	66.12	70.87	35.07	61.26	84.45	84.77	22.71	61.01	8.51	32.27	
+MAGSAC $_{\top}$	53.64	96.39	83.30	54.34	62.83	79.85	60.96	47.76	19.31	25.59	72.80	74.25	44.48	44.42	66.56	89.79	75.67	45.17	60.79	23.08	32.10	
+MAGSAC $_{\perp}$	56.55	96.89	78.35	54.70	62.05	82.11	60.98	42.28	19.48	25.26	77.78	74.17	35.81	41.45	68.51	90.12	71.18	48.08	60.62	23.72	31.97	
+AdaLAM	82.59	93.53	27.39	16.72	52.79	92.38	53.61	15.17	3.61	14.44	80.67	63.16	25.89	91.08	83.75	16.71	14.07	39.98	6.93	21.33		
+MAGSAC $_{\top}$	83.65	92.40	26.08	17.31	51.16	93.05	46.42	12.23	10.56	13.69	84.95	60.73	20.41	91.53	73.33	15.77	30.39	39.30	17.66	20.81		
+MAGSAC $_{\perp}$	84.25	92.64	25.22	17.45	50.38	94.88	46.41	11.32	11.12	14.36	87.28	69.99	17.28	91.75	73.42	15.36	30.59	39.34	17.84	20.84		
+CC	46.83	92.78	89.32	26.91	59.83	40.87	52.01	81.18	5.08	18.12	27.33	66.77	89.92	85.26	n/a	n/a	n/a	n/a	n/a	n/a	n/a	
+MAGSAC $_{\top}$	54.12	96.28	80.70	52.23	59.36	81.21	59.26	41.56	12.68	18.59	69.29	73.36	49.55	47.48	n/a	n/a	n/a	n/a	n/a	n/a	n/a	
+MAGSAC $_{\perp}$	57.00	96.69	75.85	52.94	60.12	83.30	59.14	36.73	12.67	18.20	75.61	73.44	39.61	44.77	n/a	n/a	n/a	n/a	n/a	n/a	n/a	
+CLNet	48.86	91.30	87.88	8.97	58.19	77.09	58.23	52.82	3.10	19.98	50.71	68.34	76.41	39.66	62.34	85.58	83.07	16.37	59.17	5.05	30.61	
+MAGSAC $_{\top}$	55.64	96.13	79.14	43.23	56.75	83.33	61.54	39.84	10.99	19.37	69.31	74.19	49.16	47.42	67.41	90.32	73.95	39.88	58.80	20.18	30.24	
+MAGSAC $_{\perp}$	58.52	96.59	74.21	43.90	57.72	85.15	61.33	35.34	10.96	19.02	75.56	74.24	39.01	43.39	69.38	90.66	69.44	40.97	58.65	20.87	29.98	
+ConvMatch	57.48	88.99	79.30	28.58	56.66	69.50	56.86	70.05	8.74	23.95	71.07	63.96	50.96	33.32	63.69	84.05	83.00	25.99	60.45	10.92	31.26	
+MAGSAC $_{\top}$	62.89	92.85	71.30	46.47	57.05	80.86	61.77	46.67	17.24	22.85	84.62	70.11	30.68	33.72	69.50	90.27	72.00	43.36	59.95	22.40	30.98	
+MAGSAC $_{\perp}$	65.25	93.24	67.01	47.30	57.43	83.00	61.77	41.37	17.50	23.08	87.40	70.32	25.19	32.65	71.33	90.62	67.59	44.22	59.97	23.08	31.04	
+DeMatch	52.87	91.38	88.69	26.05	57.69	70.09	55.89	67.66	6.82	22.22	64.33	65.16	57.95	39.07	63.59	83.19	81.96	24.13	59.60	9.82	30.69	
+MAGSAC $_{\top}$	58.86	95.94	75.29	44.95	58.01	81.27	60.89	45.11	14.82	22.95	82.92	72.74	36.09	40.02	69.61	89.57	70.95	41.51	58.94	21.19	30.26	
+MAGSAC $_{\perp}$	61.43	96.47	70.74	45.17	58.03	83.38	60.81	39.80	15.04	22.25	82.65	70.06	30.00	35.64	71.45	88.56	66.56	42.58	58.85	21.94	30.16	
+FC-GNN	50.51	95.34	85.52	26.90	63.37	79.49	64.92	48.23	11.06	24.54	54.32	72.08	71.04	46.44	65.09	89.13	74.92	17.95	60.00	8.84	33.13	
+MAGSAC $_{\top}$	52.15	97.19	83.91	53.34	61.34	82.19	66.61	44.57	19.75	24.46	63.57	74.51	57.22	47.40	66.60	91.39	73.07	46.57	59.17	27.16	32.53	
+MAGSAC $_{\perp}$	52.91	97.31	82.60	60.24	63.69	82.11	42.62	19.82	24.55	68.94	74.69	48.61	45.04	67.16	91.52	71.84	47.12	59.09	27.58	32.26		
+GMS	54.25	87.80	64.67	13.59	51.11	86.83	51.91	25.92	3.98	11.82	65.03	61.20	46.28	48.20	88.40	74.74	78.84	48.20	8.80	41.78	3.97	22.28
+MAGSAC $_{\top}$	63.16	89.73	59.01	47.74	50.22	89.63	49.75	22.95	8.26	12.04	76.34	62.86	32.64	37.44	76.94	83.53	44.54	30.30	41.40	16.89	22.07	
+MAGSAC $_{\perp}$	65.38	90.04	59.13	47.13	50.76	89.60	47.80	19.03	8.52	11.82	63.03	26.75	48.00	48.55	85.89	68.56	42.36	30.91	41.67	17.27	22.15	
+MS ² DG-Net	65.84	81.23	58.09	0.90	52.16	68.15	43.36	57.34	0.20	18.70	70.84	58.69	44.68	11.17	68.76	68.35	59.78	0.52	48.69	0.29	24.83	
+MAGSAC $_{\top}$	72.88	91.21	52.22	49.19	51.17	85.11	56.79	35.62	11.87	18.94	85.42	71.66	27.93	33.57	77.23	80.26	51.84	31.06	47.85	16.00	24.37	
+MAGSAC $_{\perp}$	74.47	91.62	49.24	42.79	50.69	86.68	56.73	31.66	11.66	18.18	87.76	71.92	23.30	34.49	78.55	80.58	48.82	32.36	47.46	16.78	24.04	
+NCMNet	48.30	91.24	88.72	10.54	58.90	76.16	58.45	54.53	5.16	20.86	50.91	68.41	76.44	39.95	62.07	86.37	84.67	19.40	60.22	6.65	31.31	
+MAGSAC $_{\top}$	55.23	96.03	70.74	44.46	58.49	82.52	61.43	41.22	12.34	20.87	60.57	62.32	49.00	47.42	67.16	90.86	75.22	40.47	59.68	20.29	30.72	
+MAGSAC $_{\perp}$	58.12	96.44	74.78	45.30	58.48	84.40	61.38	36.74	12.42	19.90	75.66	74.98	39.33	45.10	69.16	91.20	70.61	41.43	59.39	20.89	30.44	
+OANet	66.81	94.67	63.81	28.67	54.59	80.43	60.92	50.75	12.22	22.10	78.02	68.40	41.67	28.41	73.00	89.41	66.58	31.68	56.42	14.01	27.99	
+MAGSAC $_{\top}$	69.20	96.50	59.00	40.99	54.51	84.85	62.94	38.99	15.58	23.00	85.81	72.54	26.65	36.59	74.99	91.46	61.49	39.63	56.11	18.80	27.62	
+MAGSAC $_{\perp}$	70.91	96.87	56.68	41.90	54.72	86.33	62.63	31.87	14.72	22.14	88.30	72.87	22.06	35.43	76.24	85.81	40.56	36.21	59.49	19.49	27.79	
+MOP	44.18	89.57	92.50	10.20	62.05	70.50	52.42	61.97	3.30	23.12	50.12	60.08	66.18	49.83	61.15	81.01	79.03	8.49	57.20	3.61	31.22	
+MOP+MiHo	52.29	95.02	83.43	55.92	62.46	81.18	58.70	43.71	17.73	23.12	69.68	71.61	47.93	47.22	66.65	85.80	71.36	42.46	56.83	23.86	30.87	
+MOP+MiHo+NCC	51.63	95.03	84.32	53.88	62.49	80.28	58.91	45.86	18.15	23.96	61.70	71.58	62.41	50.87	66.62	85.64	71.16	41.30	56.49	23.10	30.83	
+MOP+MiHo+NCC	51.63	95.35	80.95	54.61	62.63	81.97	58.92	41.74	17.83	23.75	67.14	71.79	54.12	48.31	68.77	68.33	42.07	56.42	23.65	30.63		
+MOP+MiHo+NCC	51.79	84.49	95.05	3.58	64.47	59.34	45.24	74.68	0.94	24.80	46.99	63.77	78.60	41.52	55.98	76.16	84.02	3.62	59.96	1.76	33.18	
+MOP+MiHo+NCC	51.68	95.72	53.17	52.89	54.46	78.57	59.97	50.18	18.38	25.49	69.47	72.91	49.26	46.73	65.42	86.81	74.78	41.74	58.78	23.35	32.12	
+MOP+MiHo+NCC	51.05	95.69	86.17	53.29	52.84	78.30	55.18	46.59	13.51	22.32	69.76	73.47	55.16	49.32	67.01	86.83	74.20	41.20	57.94	22.97	31.43	
+NCC	0.00	52.70	98.00	0.30	60.61	0.00	24.93	99.88	0.14	21.31	0.00	43.61	89.65	29.69	0.00	38.65	97.02	0.21	54.86	0.26	29.91	
+MAGSAC $_{\$																						

IMC-PT, respectively. Moreover, although training data used to compute FC-GNN weights and the validation data are different for Megadepth, the kinds of scenes are similar. For SIFT as well as other base pipelines discussed next, the gap within AUC accuracy computed with fundamental and essential matrix estimations of FG-CNN is quite limited for MegaDepth and increases in order with IMC-PT and ScanNet. This suggests, together with the analysis of the intrinsic camera parameters reported in Fig. 5, the possibility that FC-GNN implicitly learned the camera intrinsic priors for the specific MegaDepth dataset, partially overlapping with IMC-PT, that cannot be always exploited in other non-planar datasets. Differently, MOP is not tuned on the data being handcrafted.

4.2.3 Key.Net+AffNet+HardNet+NNR

Table 2 reports the the results for Key.Net. Differently from SIFT, only MOP-based filtering and FC-GNN achieve better pose accuracy than the base Key.Net in the case of AUC_{\angle}^F and AUC_{\angle}^E , respectively, in the all non-planar datasets with or without MAGSAC. AUC_{\angle}^E score is higher for MOP+MiHo+NCC than FC-GNN and vice-versa in the case of AUC_{\angle}^F . This consideration also holds for the metric scores AUC_{\square}^F and AUC_{\square}^E . CC and MOP-based filter provide the best AUC_{\square}^H scores in the planar dataset as for SIFT.

Overall, the best score achieved by any Key.Net pipeline is lower than the corresponding SIFT one with the relevant exception of Key.Net with MOP-based filtering and NCC. For this pipeline, Key.Net plus MOP+MiHo+NCC obtains the best absolute scores also among SIFT-based pipelines when pose accuracy is estimated from the essential matrix. This indirectly supports the different nature of the SIFT blobs and Key.Net corners. From the authors' experience, on one hand, blobs are characterized to be more flat-symmetric and hence less discriminative than corners. However, on the other hand, for the same reasons keypoint localization is more stable for blobs than corners. A proper refinement step as NCC thus improves the matching process for corner-like features. Notice also that the recall improvement obtained by adding NCC with respect to the same pipeline without NCC, and in minor part also the precision, give indications

of previous matches that were outliers due to a low keypoint accuracy and have been turned into inliers.

Moreover, filters yield worse scores than the base pipeline plus MAGSAC for Key.Net, with the exception of FC-GNN and MOP-based filtering. This highlights a critical aspect of learning-based methods, that need an appropriate tuning and training on the base of the other pipeline components. Notice also that the difference between the corresponding AUC_{\angle}^F and AUC_{\angle}^E for FC-GNN on MegaDepth is more limited than with other datasets, and in particular with respect to IMC-PT. A possible justification is that the network is able to learn camera intrinsic priors of the MegaDepth images, which have less variability as outdoor scenes than IMC-PT. As discussed in the evaluation setup, all deep filters have been trained on SIFT, including FC-GNN, suggesting less generalization to different image features with respect to handcrafted approaches based on geometric constraints like MOP.

Finally, unlike SIFT, directly applying NCC after the base pipeline without MOP provides some improvements, even if these are inferior to when NCC is preceded by MOP-base filtering, confirming the original assumption that affine patch normalization is better than normalization by similarity for the refinement, but not as good as planar patch normalization.

4.2.4 SuperPoint+LightGlue

Table 3 reports the results for SuperPoint. Overall, the relative rank among the datasets and pipelines for SuperPoint is comparable with Key.Net. This is not accidental since both Key.Net and SuperPoint are based on corner-like keypoints so the same considerations and observations done for Key.Net hold for SuperPoint. Moreover, in terms of absolute score, SuperPoint with MOP+MiHo+NCC achieves on MegaDepth the top AUC_{\angle}^E value among all the evaluated pipelines, or a value almost equal to the best absolute AUC_{\angle}^E provided by LoFTR for ScanNet. Finally, the improvement in adding NCC in terms of recall and precision with respect to Key.Net is inferior but still relevant, implying a more accurate base corner relocalization of SuperPoint.

Table 2: Key.Net+_{HardNet}^{AffNet}+NNR pipeline evaluation results. All values are percentages, please refer to Sec. 4.2.3. Best viewed in color and zoomed in.

Pipeline	MegaDepth					ScanNet					Planar					IMC Photo/Tourism						
	Filtered	Precision	Recall	AUC ₂ ^F	AUC ₂ ^E	Filtered	Precision	Recall	AUC ₂ ^F	AUC ₂ ^E	Filtered	Precision	Recall	AUC ₂ ^H	Filtered	Precision	Recall	AUC ₂ ^F	AUC ₂ ^E	AUC ₂ ^F	AUC ₂ ^E	
Key.Net+ _{HardNet} ^{AffNet} +NNR	0.00	55.25	100.00	0.28	58.64	0.00	35.32	99.14	0.41	23.12	0.00	61.39	97.68	26.29	0.00	49.95	99.08	0.56	61.28	0.50	32.42	
+MAGSAC ₊	56.23	92.17	74.07	44.51	59.92	70.66	60.02	48.81	16.24	24.26	69.38	84.35	43.67	52.58	59.19	88.39	12.45	38.89	61.91	19.12	32.88	
+MAGSAC ₋	61.91	92.95	64.99	45.92	59.79	74.80	60.51	42.62	16.26	23.86	75.55	85.17	30.71	48.30	64.40	88.99	63.53	40.04	61.13	19.87	32.43	
+ACN ₊	44.49	88.17	89.73	23.71	58.00	57.15	58.68	71.79	9.99	24.04	39.88	75.03	76.36	43.88	52.28	87.51	85.05	20.94	62.10	7.59	31.58	
+MAGSAC ₊	58.65	94.88	72.18	46.29	59.43	74.24	64.58	46.79	17.32	23.71	73.41	84.85	38.13	47.58	63.20	93.91	69.45	43.70	61.93	20.30	31.34	
+MAGSAC ₋	63.78	95.58	63.78	45.98	59.87	77.67	64.54	40.44	17.06	24.33	81.25	86.18	26.91	41.66	74.39	87.49	14.41	61.66	44.37	62.11	20.74	31.59
+AdaLAM	94.16	89.61	8.72	18.21	29.07	98.86	43.96	4.36	1.89	3.89	87.24	69.75	14.92	30.08	97.26	77.95	4.21	9.16	17.12	5.06	9.12	
+MAGSAC ₊	94.83	73.42	7.72	22.14	27.60	97.72	27.00	3.22	2.74	3.78	67.11	96.9	31.63	97.58	50.08	3.65	10.07	16.47	5.76	8.78		
+MAGSAC ₋	95.20	73.66	7.22	22.28	28.23	97.69	26.96	2.97	2.78	3.61	94.11	77.55	7.31	30.48	97.71	50.15	3.47	10.14	16.57	5.79	8.94	
+CC	43.30	88.22	88.13	22.78	57.12	44.18	58.68	74.80	5.80	18.29	18.88	75.06	96.56	61.29	n/a	n/a	n/a	n/a	n/a	n/a	n/a	
+MAGSAC ₊	59.28	95.09	69.70	46.14	56.70	76.00	65.09	42.71	11.73	18.34	69.24	84.47	43.38	52.12	n/a	n/a	n/a	n/a	n/a	n/a	n/a	
+MAGSAC ₋	64.27	96.75	61.71	45.94	57.36	79.11	65.11	37.20	11.98	18.50	78.60	85.03	30.41	48.65	n/a	n/a	n/a	n/a	n/a	n/a	n/a	
+CLNet	46.58	87.22	84.85	6.50	53.69	70.26	62.57	52.58	2.87	17.24	31.70	76.53	86.03	51.14	54.46	88.22	81.60	10.85	57.83	3.22	28.22	
+MAGSAC ₊	61.14	94.55	66.88	35.07	54.08	79.49	65.69	37.92	7.79	17.06	69.95	84.08	42.18	51.02	65.27	94.04	65.61	36.06	58.33	16.35	28.48	
+MAGSAC ₋	66.01	95.26	59.00	35.76	53.71	82.09	65.51	33.11	7.58	16.94	78.99	84.89	29.78	47.71	69.33	94.51	58.20	36.31	58.06	16.50	28.26	
+ConvMatch	57.31	86.27	71.90	23.32	51.80	65.30	63.01	65.15	8.08	21.42	76.05	69.98	37.41	30.45	50.83	87.73	77.27	26.08	58.39	9.41	28.10	
+MAGSAC ₊	68.56	91.76	59.26	36.07	52.50	77.95	66.65	42.85	13.98	23.69	80.65	71.94	18.21	23.34	69.55	93.46	61.43	40.12	58.78	17.40	28.17	
+MAGSAC ₋	72.51	92.39	52.28	36.31	52.66	80.77	66.58	37.29	13.99	22.31	92.46	72.21	13.21	29.94	73.15	93.95	54.37	40.45	58.97	17.57	28.47	
+DeMatch	51.71	87.83	80.18	20.59	52.43	65.89	61.71	62.60	6.46	19.87	61.52	76.10	52.04	40.66	55.34	87.40	77.96	23.99	58.83	8.91	28.65	
+MAGSAC ₊	64.47	94.67	83.18	43.95	52.27	78.37	65.74	41.41	12.16	20.66	82.03	83.60	26.97	41.14	68.48	93.66	61.97	39.19	58.66	17.43	28.71	
+MAGSAC ₋	68.90	95.29	55.81	35.64	53.47	81.18	65.71	35.95	12.22	20.11	86.97	84.94	19.24	20.07	72.20	94.16	54.87	39.36	58.63	17.62	28.45	
+FC-GNN	50.48	94.36	84.27	26.41	63.06	72.49	49.91	10.21	25.52	36.22	81.78	85.89	57.59	56.45	92.47	79.84	21.11	66.27	10.60	36.39		
+MAGSAC ₊	53.48	96.74	80.97	59.39	62.61	75.83	69.67	45.03	18.25	25.10	52.89	84.58	65.55	53.75	59.11	95.43	76.76	51.24	65.84	27.96	35.94	
+MAGSAC ₋	54.82	96.98	78.76	60.05	62.73	77.10	64.71	42.76	18.80	25.25	61.49	80.92	53.93	52.69	60.24	95.85	74.71	51.86	65.07	28.35	35.73	
+GMS	53.37	81.82	67.79	10.74	50.61	78.99	57.76	33.96	4.94	13.12	50.28	76.57	42.79	11.77	58.20	6.03	49.05	0.34	22.63			
+MAGSAC ₊	65.89	86.38	53.61	43.95	51.27	85.31	55.68	24.85	8.78	13.21	76.67	76.05	29.42	42.74	72.42	86.59	46.48	32.80	47.48	16.53	24.42	
+MAGSAC ₋	70.04	86.94	47.51	35.72	52.14	87.09	55.67	21.95	8.62	12.91	83.45	76.77	21.17	40.66	75.52	86.98	41.87	32.96	47.38	16.70	24.16	
+MS ² DG-Net	66.10	78.94	54.24	0.25	46.85	64.34	52.34	55.52	0.24	16.46	72.55	70.11	36.57	9.14	65.93	76.79	58.20	0.63	49.05	0.34	22.63	
+MAGSAC ₊	77.91	91.45	43.00	36.60	46.70	81.94	64.02	34.44	9.30	16.20	88.95	83.81	18.20	34.90	76.63	88.14	46.25	31.70	48.61	13.70	24.48	
+MAGSAC ₋	79.99	92.06	38.10	37.02	47.47	84.09	63.83	30.25	9.76	16.69	91.88	84.14	13.58	33.60	79.27	88.61	41.18	32.10	48.50	13.83	22.49	
+NCMNet	46.21	87.41	85.76	7.08	54.16	69.70	61.60	52.19	4.17	17.72	31.96	76.36	85.77	51.58	53.75	88.72	83.73	13.10	58.80	3.98	28.82	
+MAGSAC ₊	60.83	94.64	67.61	35.84	53.48	78.97	64.38	37.65	9.02	17.42	60.96	84.05	42.36	51.22	64.75	94.31	67.13	36.65	58.68	16.20	28.37	
+MAGSAC ₋	65.73	95.34	59.69	35.78	53.48	81.56	64.37	33.04	9.12	17.32	79.05	84.62	29.90	43.03	68.88	94.81	59.50	36.96	58.62	16.48	28.62	
+OANet	68.16	89.98	56.89	17.42	49.57	81.07	59.83	35.22	6.58	14.51	81.87	75.55	28.75	28.75	72.65	98.84	55.55	20.98	52.50	7.01	23.25	
+MAGSAC ₊	74.91	94.58	47.17	30.25	39.36	86.20	61.84	26.14	8.96	15.59	90.61	83.61	15.81	31.11	77.50	94.11	46.80	31.72	52.41	12.50	23.17	
+MAGSAC ₋	77.96	95.48	41.75	30.28	39.68	87.64	61.71	23.32	9.24	15.37	91.62	85.96	11.62	29.90	79.98	94.55	41.79	31.99	52.50	12.68	23.26	
+MOP	38.34	83.94	93.61	8.96	54.02	56.68	54.02	55.59	4.01	24.46	26.64	75.28	91.72	59.09	46.48	84.12	89.41	9.92	61.68	4.17	32.71	
+MAGSAC ₊	57.18	93.69	72.89	50.96	60.89	74.24	64.17	46.86	17.01	24.42	69.50	84.36	43.06	52.00	61.42	92.39	47.91	34.95	61.64	22.68	32.75	
+MAGSAC ₋	61.59	94.27	63.43	51.66	60.40	77.90	64.28	40.36	16.98	27.16	84.10	84.24	74.70	53.23	58.21	93.07	77.51	45.53	64.66	23.98	35.24	
+MOP+NCC	38.34	84.51	95.58	8.24	63.67	54.02	55.59	58.17	3.93	27.20	26.64	78.54	99.50	61.15	46.48	83.71	89.89	8.98	65.60	3.80	36.13	
+MAGSAC ₊	51.89	94.45	83.19	52.52	61.98	70.95	64.99	53.70	16.88	26.44	71.74	85.08	52.05	57.08	62.61	91.78	72.39	44.14	62.65	22.68	33.36	
+MAGSAC ₋	54.75	94.89	78.53	53.98	62.95	73.64	65.06	48.80	19.08	26.44	75.55	85.42	66.94	57.47	59.71	93.07	74.90	46.03	65.46	24.26	35.69	
+MOP+MiHo+NCC	33.27	80.15	98.83	3.47	61.83	40.56	50.18	57.34	1.46	28.19	24.30	73.88	93.49	50.86	40.44	77.40	94.30	4.10	66.99	2.07	36.92	
+MAGSAC ₊	51.30	94.96	85.05	53.45	63.91	68.69	65.17	58.15	19.37	27.85	47.43	85.08	85.26	57.08	92.61	79.57	44.99	65.78	23.61	35.90		
+MAGSAC ₋	54.20	95.46	80.34	54.75	63.77	71.64	65.23	52.50</td														

Table 3: SuperPoint+LightGlue pipeline evaluation results. All values are percentages, please refer to Sec. 4.2.4. Best viewed in color and zoomed in.

Pipeline	MegaDepth				ScanNet				Planar				IMC PhotoTourism								
	Filtered	Precision	Recall	AUC F	AUC E	Filtered	Precision	Recall	AUC F	AUC E	Filtered	Precision	Recall	AUC $^H_{\square}$	Filtered	Precision	Recall	AUC F	AUC $^E_{\square}$	AUC $^F_{\square}$	AUC $^E_{\square}$
SuperPoint+LightGlue	0.00	88.68	99.92	48.33	61.67	0.00	68.94	94.64	17.51	33.70	0.00	74.77	90.77	63.45	0.00	89.40	99.59	43.01	66.78	20.14	35.89
+MAGSAC $_{\square}$	33.98	94.26	71.95	54.18	63.44	33.86	71.40	65.35	25.78	34.49	63.71	82.23	37.16	51.93	33.51	94.37	71.24	51.76	68.12	26.38	37.28
+MAGSAC $_{\square}$	45.45	95.24	60.50	54.83	63.34	43.51	71.59	55.69	26.29	34.52	74.53	93.94	25.24	49.00	44.75	95.11	59.98	51.91	68.55	26.57	37.56
+ACN $_{\square}$	42.49	89.55	58.25	32.63	47.95	45.93	70.40	51.60	13.75	24.69	54.28	76.67	43.05	46.10	42.75	90.57	57.89	34.62	56.34	14.95	26.51
+MAGSAC $_{\square}$	60.33	93.99	43.11	36.41	51.90	61.81	71.22	38.24	16.08	25.39	81.57	82.22	19.55	41.63	59.59	94.15	43.24	38.02	58.37	16.99	27.88
+MAGSAC $_{\square}$	67.00	94.77	36.43	36.27	52.63	66.68	71.28	33.20	16.31	25.31	86.99	82.73	13.58	40.14	66.01	94.84	36.78	38.38	58.72	17.09	28.04
+AdaLAM	0.00	88.68	99.92	48.33	61.67	0.00	68.94	94.64	17.51	33.70	0.00	74.77	90.77	63.45	0.00	89.40	99.59	43.01	66.78	20.14	35.89
+MAGSAC $_{\square}$	33.98	94.36	71.95	54.18	63.44	33.86	71.40	65.35	25.78	34.49	63.71	82.23	37.16	51.93	33.51	94.37	71.24	51.76	68.12	26.38	37.28
+MAGSAC $_{\square}$	45.45	95.24	60.50	54.83	63.34	43.51	71.59	55.69	26.29	34.52	74.53	93.94	25.24	49.00	44.75	95.11	59.98	51.91	68.55	26.57	37.56
+CC	17.52	85.07	83.18	35.16	52.77	32.10	61.08	64.01	15.72	26.61	75.86	13.28	16.05	8.48	n/a	n/a	n/a	n/a	n/a	n/a	n/a
+MAGSAC $_{\square}$	44.41	89.75	60.53	41.00	54.46	52.82	62.21	46.48	18.06	26.92	91.30	14.91	5.86	6.29	n/a	n/a	n/a	n/a	n/a	n/a	n/a
+MAGSAC $_{\square}$	54.02	90.57	50.91	41.50	56.66	59.37	62.39	39.87	18.89	27.14	93.00	14.94	3.92	5.60	n/a	n/a	n/a	n/a	n/a	n/a	n/a
+CLNet	19.20	89.47	81.49	27.70	49.75	46.48	71.37	51.09	9.28	20.75	13.37	75.24	81.23	61.27	25.55	90.51	75.15	26.94	56.19	11.32	26.16
+MAGSAC $_{\square}$	45.11	93.99	59.50	33.41	53.10	60.81	70.31	39.25	11.30	20.02	66.23	81.83	34.40	50.27	48.06	94.04	55.50	32.60	57.83	14.21	27.27
+MAGSAC $_{\square}$	54.58	94.80	50.03	33.48	54.19	65.79	70.38	34.17	11.03	21.19	76.18	82.71	23.64	47.02	56.56	94.70	46.96	32.87	58.09	14.26	27.31
+ConvMatch	64.74	89.98	35.96	22.44	35.49	64.00	71.19	35.31	10.88	20.11	61.77	76.39	36.15	42.02	63.05	90.79	37.64	25.88	45.39	10.68	19.88
+MAGSAC $_{\square}$	74.00	92.76	27.93	25.11	37.60	73.27	70.15	27.66	11.84	19.74	83.57	91.41	17.16	37.88	72.57	93.20	29.23	27.92	47.04	11.69	20.92
+DoMatch	64.49	89.69	36.03	22.06	33.45	67.95	71.35	31.57	6.68	15.36	67.00	76.28	30.72	39.30	65.02	90.67	35.56	22.92	40.67	9.05	16.88
+MAGSAC $_{\square}$	74.23	92.95	27.62	23.69	36.34	75.65	70.78	25.29	7.80	15.85	85.90	81.37	14.45	35.94	74.12	93.35	27.51	24.57	42.58	10.04	17.68
+MAGSAC $_{\square}$	78.41	93.93	23.73	24.43	38.58	76.37	70.20	24.45	11.95	20.26	88.39	92.69	11.96	36.94	76.82	93.75	24.94	27.38	47.52	11.83	21.21
+FC-GNN	21.75	96.68	89.40	62.64	66.20	29.05	72.34	68.78	22.54	32.69	10.93	80.58	94.31	65.54	24.98	95.84	82.67	54.65	70.79	29.37	40.47
+MAGSAC $_{\square}$	23.84	97.16	87.58	56.19	66.02	38.07	72.90	62.31	25.89	32.62	35.67	72.84	59.95	27.90	96.47	80.19	59.02	70.81	32.74	40.26	32.99
+MAGSAC $_{\square}$	25.59	97.32	85.79	41.49	66.46	73.03	78.00	26.31	33.09	46.14	83.11	61.40	57.54	30.06	86.63	77.98	59.36	70.78	60.61	21.69	32.40
+GMS	25.29	85.09	75.11	43.61	54.54	51.88	68.80	48.55	14.98	23.29	38.01	75.89	61.98	54.59	29.78	88.76	70.83	38.78	58.40	18.15	30.00
+MAGSAC $_{\square}$	49.69	88.28	54.39	48.16	55.82	63.35	67.33	37.44	17.03	23.94	76.38	81.07	26.53	44.64	51.36	91.82	51.96	43.63	60.24	21.64	31.69
+MAGSAC $_{\square}$	58.28	89.02	45.81	56.89	63.08	74.20	71.97	23.64	13.61	18.77	88.47	82.64	8.93	36.64	81.15	94.68	20.27	30.92	44.92	13.16	19.38
+MS ^D Net	71.11	90.02	29.50	33.55	34.68	62.08	71.06	34.26	13.01	18.54	66.27	76.71	28.04	40.29	69.75	90.97	30.59	30.41	41.96	12.91	17.58
+MAGSAC $_{\square}$	79.64	94.31	22.24	32.30	38.50	72.38	72.00	26.74	13.59	18.31	84.72	81.98	13.03	37.29	77.93	94.10	23.49	30.90	43.89	13.24	18.74
+MAGSAC $_{\square}$	82.92	95.07	18.94	31.73	40.30	75.29	71.97	23.64	13.61	18.77	88.47	82.64	8.93	36.64	81.15	94.68	20.27	30.92	44.92	13.16	19.38
+NCMNet	16.76	89.49	83.97	27.43	50.79	41.91	71.05	55.77	10.33	22.43	12.10	75.30	82.95	62.22	21.88	90.58	78.93	28.26	56.70	11.91	26.52
+MAGSAC $_{\square}$	43.53	93.89	61.29	34.26	53.51	57.43	70.06	42.81	13.52	22.62	65.96	81.21	34.70	50.48	45.62	94.08	58.17	33.66	58.25	14.72	27.58
+MAGSAC $_{\square}$	53.25	94.70	51.54	34.43	54.08	63.07	70.13	37.09	13.00	22.84	76.23	82.15	23.58	47.81	54.56	94.74	49.20	33.73	58.57	14.74	27.74
+OANet	90.17	96.66	10.17	10.38	16.93	68.31	70.07	10.96	4.19	7.28	88.66	90.23	2.23	25.48	89.00	91.05	10.30	10.30	11.75	23.38	4.71
+MAGSAC $_{\square}$	92.08	91.54	8.43	9.75	17.49	91.76	62.88	8.21	3.70	7.30	94.45	79.91	4.75	27.23	91.72	8.50	11.43	24.05	4.55	9.17	1.67
+MAGSAC $_{\square}$	93.02	91.84	7.48	9.79	17.82	62.91	71.71	53.41	25.77	33.23	77.37	89.87	3.41	25.24	89.81	45.34	50.47	51.19	68.47	2.66	37.48
+MOP	0.90	88.79	99.29	48.18	61.99	6.48	68.85	89.16	33.41	7.89	74.95	90.37	64.11	1.66	83.16	92.48	28.21	71.12	11.80	40.46	
+MAGSAC $_{\square}$	34.31	94.32	71.63	53.93	63.51	38.02	71.09	62.97	25.31	33.73	66.70	82.24	37.21	51.86	33.87	94.30	70.72	51.07	68.05	25.94	37.32
+MAGSAC $_{\square}$	25.98	96.22	84.15	61.06	66.42	40.63	71.10	60.91	97.95	34.93	38.77	82.77	72.88	60.22	33.41	95.30	73.25	54.56	70.56	24.05	37.64
+MOP+NCC	0.90	85.68	98.49	35.29	55.73	10.20	65.79	86.66	14.22	34.64	7.89	75.81	98.83	64.35	1.66	83.16	92.48	28.21	71.12	11.80	40.46
+MAGSAC $_{\square}$	34.07	94.35	71.87	53.93	63.38	36.02	71.27	64.18	25.48	34.44	66.55	82.24	37.21	51.86	33.87	94.34	70.93	51.50	68.17	26.28	37.56
+MAGSAC $_{\square}$	45.57	95.25	60.39	54.40	63.19	45.52	71.44	54.57	25.80	34.54	77.27	82.82	25.26	48.99	45.09	95.07	59.68	51.60	68.47	26.36	37.64
+MOP+MiHo+NCC	0.30	85.90	99.36	35.88	55.06	6.48	68.50	89.20	14.45	35.21	6.98	76.09	97.97	64.40	0.98	83.38	93.29	29.15	71.02	11.95	40.31
+MAGSAC $_{\square}$	23.40	96.32	84.95	63.05	68.00	38.78	71.35	61.95	26.45	35.50	38.61	82.87	73.00	60.33	30.03	95.46	73.71	55.61	70.78	30.06	40.10
+MAGSAC $_{\square}$	29.81	96.76	80.53	63.85	67.48	44.78	71.48	55.94	26.61	36.09	48.20	83.41	61.91	57.4							

Table 4: ALIKED+SuperGlue pipeline evaluation results. All values are percentages, please refer to Sec. 4.2.5. Best viewed in color and zoomed in.

Pipeline	MegaDepth					ScanNet					Planar					IMC Photo/Tourism					
	Filtered	Precision	Recall	AUC $^F_{\triangle}$	AUC $^E_{\triangle}$	Filtered	Precision	Recall	AUC $^F_{\triangle}$	AUC $^E_{\triangle}$	Filtered	Precision	Recall	AUC $^H_{\square}$	Filtered	Precision	Recall	AUC $^F_{\triangle}$	AUC $^E_{\triangle}$	AUC $^F_{\square}$	AUC $^E_{\square}$
ALIKED+LightGlue	0.00	92.05	99.72	54.83	61.79	0.00	65.30	93.08	12.72	26.70	0.00	76.17	90.91	60.79	0.00	93.63	99.75	47.72	67.17	23.37	36.09
+MAGSAC $_{\top}$	15.88	95.63	95.88	61.86	61.82	33.48	68.44	63.40	19.55	26.98	49.92	81.77	32.63	53.40	15.81	96.29	86.75	58.68	67.78	31.35	36.58
+MAGSAC $_{\perp}$	23.71	96.49	79.40	61.79	63.35	40.67	66.40	57.83	19.90	26.82	61.56	80.39	50.52	23.19	96.74	79.58	58.91	68.17	31.60	36.87	
+ACN $_{\top}$	39.70	93.67	60.76	34.39	49.70	42.98	67.49	54.59	9.90	18.34	52.20	77.15	44.12	45.24	41.51	94.59	59.05	39.32	58.98	16.70	27.58
+MAGSAC $_{\top}$	47.23	95.55	54.51	39.15	50.64	58.87	67.69	41.04	11.91	18.85	72.64	80.77	28.14	43.06	48.84	96.33	52.78	45.15	59.22	20.58	27.79
+MAGSAC $_{\perp}$	51.60	96.65	90.32	39.46	51.73	62.63	67.70	37.10	12.07	18.92	78.24	81.20	22.17	41.86	52.76	96.71	48.94	45.64	59.65	20.90	28.30
+AdaLAM	0.00	92.95	99.72	54.83	61.79	0.00	65.50	93.08	12.72	26.70	0.00	76.17	90.91	60.79	0.00	93.63	99.75	47.72	67.17	23.37	36.09
+MAGSAC $_{\top}$	15.88	95.63	86.88	61.86	61.82	33.48	68.44	65.40	19.55	26.98	49.92	81.77	52.73	53.40	15.81	96.29	86.75	58.68	67.78	31.35	36.58
+MAGSAC $_{\perp}$	23.72	96.23	79.40	61.79	63.35	40.67	66.40	57.83	19.90	26.82	61.56	80.39	50.52	23.19	96.74	79.58	58.91	68.17	31.60	36.87	
+CC	17.59	86.24	82.54	43.16	53.84	33.98	54.91	61.10	10.39	19.04	79.33	10.37	12.65	7.57	n/a	n/a	n/a	n/a	n/a	n/a	n/a
+MAGSAC $_{\top}$	29.82	88.36	72.49	48.27	54.97	54.56	55.91	44.51	12.35	18.91	92.81	11.14	6.78	6.09	n/a	n/a	n/a	n/a	n/a	n/a	n/a
+MAGSAC $_{\perp}$	36.19	88.86	66.33	48.47	54.98	58.99	55.92	39.78	12.63	18.98	94.12	11.25	5.39	5.59	n/a	n/a	n/a	n/a	n/a	n/a	n/a
+CLNet	14.87	93.37	85.31	35.30	52.86	46.80	68.60	50.87	6.09	16.60	17.63	77.43	80.43	55.22	19.67	94.49	80.87	36.07	59.50	15.51	28.05
+MAGSAC $_{\top}$	26.62	95.41	75.64	41.56	53.98	60.40	64.41	39.42	8.74	16.28	55.66	81.63	47.42	51.44	29.96	96.22	72.03	43.68	60.12	19.97	28.74
+MAGSAC $_{\perp}$	33.00	95.03	69.53	41.54	54.66	64.07	64.51	35.67	8.98	15.42	66.01	82.23	36.30	47.88	35.55	96.62	66.60	44.09	60.30	20.14	28.73
+ConvMatch	65.67	93.06	34.30	26.47	40.50	65.97	67.98	33.09	6.72	14.24	62.92	76.76	34.06	41.41	64.47	94.35	35.83	31.57	50.94	12.56	22.91
+MAGSAC $_{\top}$	69.64	94.31	31.20	28.21	40.97	75.33	64.30	25.40	7.51	15.52	77.70	79.28	22.15	39.21	68.53	94.45	32.37	35.71	51.74	15.37	23.18
+MAGSAC $_{\perp}$	72.07	94.71	29.87	29.19	41.17	77.38	64.34	23.22	7.39	13.59	82.13	79.59	17.51	33.07	70.91	95.81	30.05	36.16	51.45	15.44	23.01
+DeMatch	64.63	93.35	35.44	24.51	40.23	68.01	67.36	31.01	4.37	11.01	66.67	76.40	29.59	36.16	65.18	94.39	35.10	28.42	47.54	10.90	20.20
+MAGSAC $_{\top}$	68.65	94.79	32.16	26.79	40.43	76.15	64.28	24.39	5.14	10.97	79.83	79.85	19.60	36.54	69.12	96.26	31.71	32.35	48.09	13.09	20.31
+MAGSAC $_{\perp}$	71.12	95.21	29.79	27.15	40.04	78.13	64.34	22.34	5.29	11.17	83.69	80.20	15.59	43.76	71.39	96.12	29.50	32.84	48.19	13.40	20.22
+FC-GNN	13.69	96.89	90.93	63.46	64.75	32.30	70.66	65.88	16.71	25.28	13.04	77.93	82.53	55.93	13.63	95.25	87.70	53.11	65.92	27.17	34.55
+MAGSAC $_{\top}$	15.66	97.24	89.35	65.62	65.38	40.67	70.76	59.67	18.82	25.68	51.61	81.27	49.65	52.03	22.25	96.54	80.21	57.74	66.60	30.56	35.59
+MAGSAC $_{\perp}$	17.31	97.35	87.69	65.70	65.05	43.23	70.79	56.96	18.93	25.64	62.53	81.93	38.09	49.00	28.30	96.74	74.32	37.85	66.74	30.67	35.29
+GMS	20.69	90.93	79.57	51.23	56.55	54.20	64.58	46.40	9.34	16.76	38.96	75.70	61.70	51.11	20.11	93.69	80.89	46.52	62.58	22.48	32.51
+MAGSAC $_{\top}$	31.61	92.02	70.44	55.77	56.69	63.94	60.87	36.63	11.24	16.49	63.74	79.12	38.84	45.79	30.65	95.23	71.31	53.21	62.83	27.23	32.43
+MAGSAC $_{\perp}$	37.44	92.49	64.85	55.75	52.75	67.54	60.92	32.94	11.29	16.82	72.27	79.02	29.93	47.55	36.24	95.63	65.87	53.42	63.15	27.40	32.70
+MS ² DG-Net	70.80	93.83	29.36	36.82	37.72	59.15	67.82	35.97	7.45	11.77	65.87	77.95	27.91	41.45	70.10	94.70	30.12	34.37	45.40	14.35	18.96
+MAGSAC $_{\top}$	74.76	95.64	26.19	37.23	38.15	69.82	68.28	27.92	8.35	11.35	81.41	83.21	38.12	73.66	96.16	27.13	37.33	45.53	16.59	19.23	
+MAGSAC $_{\perp}$	76.84	96.13	24.18	37.56	38.81	71.81	68.19	25.96	7.89	11.46	84.69	81.72	14.78	37.42	75.55	96.50	25.31	37.60	45.72	16.69	19.30
+NCINet	13.49	93.44	86.78	36.15	53.66	44.51	67.92	52.75	7.34	16.99	15.98	76.62	80.94	55.86	17.09	94.58	83.54	36.70	59.38	15.71	28.22
+MAGSAC $_{\top}$	25.51	95.38	76.85	41.77	53.33	58.85	63.73	40.79	9.68	16.50	53.86	80.26	48.51	50.65	27.79	96.26	74.33	43.45	59.76	19.69	28.28
+MAGSAC $_{\perp}$	32.03	95.00	70.62	42.51	55.06	62.69	63.79	36.83	9.45	17.02	64.78	80.75	37.07	43.39	66.66	96.68	44.03	60.18	19.97	28.61	
+OANet	89.60	94.35	10.53	12.24	23.76	88.14	67.35	11.04	2.87	5.90	89.91	76.42	9.21	27.86	90.20	94.90	10.93	15.46	32.57	5.54	12.40
+MAGSAC $_{\top}$	90.44	94.73	9.85	13.08	24.04	92.89	52.54	7.12	2.66	5.82	94.03	77.88	6.01	27.55	90.13	95.24	10.14	17.26	32.60	6.44	12.44
+MAGSAC $_{\perp}$	90.94	94.97	9.36	13.72	23.64	93.31	52.52	6.79	2.70	6.04	95.17	78.04	4.86	27.13	95.05	95.46	9.61	17.36	32.68	6.43	12.63
+MOP	1.05	92.99	99.02	55.50	62.22	17.92	64.46	82.25	13.76	26.17	11.47	77.20	92.41	61.77	1.05	86.79	91.65	25.69	67.85	9.87	37.03
+MAGSAC $_{\top}$	16.29	95.65	86.82	61.56	62.02	41.40	66.82	60.03	18.59	25.99	16.23	84.48	51.62	52.82	16.13	96.29	86.49	58.28	67.02	31.04	36.38
+MAGSAC $_{\perp}$	22.05	96.09	81.58	56.91	63.49	43.30	66.70	58.99	18.51	26.42	13.38	83.84	81.66	73.71	59.69	86.43	96.21	51.35	67.03	26.94	36.67
+MOP+NCC	1.05	87.74	98.81	33.18	63.06	17.92	62.01	80.76	8.52	27.29	11.47	77.20	92.41	61.77	1.05	86.79	91.65	25.69	67.85	9.87	37.03
+MAGSAC $_{\top}$	26.22	96.49	77.62	57.28	62.94	47.93	66.72	54.06	18.81	26.73	13.10	82.00	63.53	57.33	30.72	96.56	71.97	52.11	66.81	27.42	36.36
+MOP+MiHo+NCC	0.52	88.00	94.50	34.22	63.86	11.29	62.91	86.28	8.81	27.50	9.82	77.08	93.31	60.10	0.55	93.73	99.48	48.81	67.76	9.80	36.86
+MAGSAC $_{\top}$	21.47	96.29	82.26	58.07	64.09	39.72	68.00	61.91	18.95	20.51	13.55	83.54	81.59	73.66	26.14	96.29	74.44	52.04	66.98	26.94	36.42
+MAGSAC $_{\perp}$	25.54	96.94	78.37	59.01	62.86	44.73	68.13	56.75	19.34	22.52	13.74	82.11	63.89								

Table 5: DISK+LighGlue pipeline evaluation results. All values are percentages, please refer to Sec. 4.2.6. Best viewed in color and zoomed in.

Pipeline	MegaDepth				ScanNet				Planar				IMC PhotoTourism									
	Filtered	Precision	Recall	AUC ^F	AUC ^E	Filtered	Precision	Recall	AUC ^F	AUC ^E	Filtered	Precision	Recall	AUC ^H	Filtered	Precision	Recall	AUC ^F	AUC ^E	AUC ^F	AUC ^E	
DISK+LightGlue	0.00	92.27	99.93	58.22	64.70	0.00	63.40	89.67	12.05	24.96	0.00	72.89	88.47	89.26	0.00	93.33	99.59	56.11	51.11	71.98	29.97	40.91
+MAGSAC _T	20.27	95.36	83.11	63.27	64.97	37.07	64.24	85.45	18.98	25.26	55.05	77.47	43.73	49.87	17.92	95.03	84.44	63.70	72.37	36.04	41.46	31.47
+MAGSAC _I	31.13	98.11	72.68	63.14	65.32	45.54	64.58	51.00	18.77	24.59	67.08	78.21	31.03	47.28	28.09	96.55	74.66	63.75	72.33	36.19	41.47	31.47
+ACN _T	46.64	92.95	53.85	37.56	53.13	48.36	65.26	46.54	8.74	17.02	58.26	74.01	36.20	41.33	51.14	94.36	49.15	46.17	63.76	21.19	32.01	
+MAGSAC _T	56.04	95.25	45.84	40.99	53.54	67.25	63.39	31.84	11.13	17.27	79.69	77.57	20.46	38.97	58.58	95.37	42.66	49.82	64.24	23.94	32.29	
+MAGSAC _I	61.72	98.36	40.39	41.43	54.23	71.26	63.50	27.71	10.86	17.98	84.91	88.11	14.99	37.27	63.33	96.93	38.07	50.01	64.24	23.91	32.22	
+AdlAM	0.00	92.27	99.93	58.22	64.79	0.00	63.40	89.67	12.05	24.96	0.00	72.89	88.47	59.26	0.00	93.38	99.59	56.11	51.11	71.98	29.97	40.91
+MAGSAC _T	20.27	95.36	83.11	63.27	64.97	37.08	64.24	60.05	18.98	25.26	55.05	77.47	43.73	49.87	17.92	95.03	84.44	63.70	72.37	36.04	41.46	31.47
+MAGSAC _I	31.13	98.11	72.68	63.14	65.32	45.54	64.58	51.00	18.77	24.59	67.08	78.21	31.03	47.28	28.09	96.55	74.66	63.75	72.33	36.19	41.47	31.47
+CC	16.37	85.47	83.94	46.76	56.25	23.68	52.79	66.68	11.13	20.06	72.38	10.70	14.29	7.38	n/a	n/a	n/a	n/a	n/a	n/a	n/a	
+MAGSAC _T	32.81	87.99	70.01	50.14	58.16	52.00	52.62	45.09	14.26	20.62	90.64	11.49	5.02	5.11	n/a	n/a	n/a	n/a	n/a	n/a	n/a	
+MAGSAC _I	41.90	88.68	61.28	50.68	58.21	58.08	52.78	39.09	14.57	19.97	92.00	11.61	3.62	4.86	n/a	n/a	n/a	n/a	n/a	n/a	n/a	
+CLNet	13.94	92.83	86.48	36.78	56.00	34.98	65.74	58.37	6.72	18.73	8.94	23.50	81.78	58.97	19.32	94.16	80.91	43.14	65.77	19.91	33.94	
+MAGSAC _T	30.14	95.26	72.61	41.92	56.95	57.80	61.43	40.60	9.59	18.47	57.48	77.55	41.87	49.59	32.37	95.85	69.56	48.26	66.06	23.15	33.93	
+MAGSAC _I	39.51	96.00	63.61	41.95	57.74	63.39	61.55	35.00	9.43	18.15	68.95	78.05	29.80	46.38	40.49	96.44	61.73	48.56	66.20	23.45	34.21	
+ConvMatch	64.76	92.87	35.72	26.06	43.06	65.35	65.33	31.80	7.07	15.88	60.31	23.93	34.98	40.48	63.16	94.19	37.06	37.72	55.75	15.87	26.00	
+MAGSAC _T	70.23	94.26	39.09	30.35	42.66	78.22	60.33	21.89	8.06	15.18	80.45	76.47	19.66	37.95	68.29	53.37	32.59	40.95	56.19	17.86	26.49	
+MAGSAC _I	73.90	94.99	27.45	30.86	43.09	80.88	60.39	19.08	8.83	15.97	85.48	76.85	14.38	36.79	71.82	96.88	29.18	41.23	56.22	18.11	26.33	
+DoMatch	64.91	92.73	35.35	26.59	42.63	67.46	64.84	29.57	4.92	12.31	66.10	23.56	29.01	35.74	65.10	94.16	35.05	35.01	53.39	14.14	24.11	
+MAGSAC _T	70.55	94.64	30.49	28.97	42.64	79.04	60.69	20.88	6.03	12.03	83.22	76.73	16.78	35.31	70.08	96.52	30.72	38.17	53.85	15.96	24.47	
+MAGSAC _I	74.23	95.26	26.96	28.99	42.35	81.60	61.74	18.18	6.22	13.01	87.53	77.11	12.15	37.34	74.03	96.03	27.48	38.69	53.67	16.27	24.10	
+FC-GNN	9.99	97.04	96.66	65.53	65.62	20.88	67.10	72.61	16.88	25.39	5.74	76.15	87.54	60.21	10.29	97.00	93.86	64.51	73.68	37.45	43.85	
+MAGSAC _T	11.58	97.33	95.29	67.61	67.26	35.09	66.01	63.56	20.99	25.38	33.10	77.50	68.97	56.37	12.25	97.30	92.25	67.51	73.63	39.73	43.49	
+MAGSAC _I	13.11	97.45	93.80	67.79	66.88	38.13	66.08	41.00	21.00	25.44	42.59	78.23	59.22	53.66	13.95	97.40	90.59	67.56	73.84	39.79	43.90	
+GMS	13.70	90.59	86.54	56.85	59.93	34.62	60.51	64.55	12.92	23.51	24.01	72.59	75.84	57.24	12.29	93.33	87.89	56.82	69.76	30.55	39.33	
+MAGSAC _T	30.39	92.74	72.30	59.24	61.80	53.51	59.67	45.99	16.95	22.86	62.32	76.83	40.13	49.28	26.91	95.19	75.15	61.05	70.21	33.89	39.80	
+MAGSAC _I	39.64	93.44	63.40	59.39	62.73	60.62	61.68	37.55	10.77	19.36	68.62	78.14	36.66	48.94	35.81	95.76	66.59	61.06	70.32	33.91	39.78	
+MS ^D Net	75.84	93.65	24.65	41.98	38.84	57.11	65.05	33.56	7.72	12.83	63.61	74.41	23.80	36.96	74.52	94.62	25.55	42.68	51.13	19.61	23.09	
+MAGSAC _T	79.77	95.51	21.32	42.49	40.02	72.95	64.03	23.40	9.84	12.99	83.14	77.11	13.00	36.33	78.18	95.83	22.45	46.06	50.95	21.87	22.88	
+MAGSAC _I	82.24	96.18	18.91	42.64	41.11	75.35	64.17	21.07	9.55	12.75	86.40	77.67	9.65	35.76	80.51	96.35	20.20	46.24	51.43	22.06	23.14	
+NCNNet	12.44	92.76	87.97	36.25	55.12	31.04	65.40	62.14	8.43	18.50	7.23	74.42	83.52	59.63	16.35	94.18	83.91	43.52	65.42	20.29	33.32	
+MAGSAC _T	28.92	95.08	73.87	41.26	57.18	54.86	61.57	43.66	10.58	18.56	56.98	77.51	42.81	49.99	29.06	95.87	72.06	48.52	65.71	23.33	33.62	
+MAGSAC _I	38.44	95.83	64.74	41.79	55.63	60.90	61.68	37.55	10.77	19.36	68.62	78.14	36.67	46.94	38.43	96.46	63.90	48.76	66.01	23.53	33.85	
+OANet	69.94	87.70	10.34	17.22	27.62	66.70	64.39	10.77	8.30	8.30	87.82	73.24	8.37	28.32	98.49	94.59	10.55	21.23	38.68	7.97	15.67	
+MAGSAC _T	91.19	94.70	9.18	17.00	28.00	62.60	56.01	6.66	4.30	8.03	94.31	52.28	5.24	28.24	90.80	95.24	9.41	22.47	38.97	8.58	15.65	
+MAGSAC _I	92.08	95.14	8.32	17.57	28.49	63.26	56.02	5.99	4.62	10.37	95.59	53.75	5.23	38.25	91.68	95.64	8.55	22.91	39.35	8.74	15.98	
+MOP	0.67	92.39	99.53	39.10	64.04	23.90	59.81	75.39	12.79	23.88	15.86	72.70	83.65	58.91	1.22	93.58	98.82	57.86	72.09	31.26	41.10	
+MAGSAC _T	20.47	95.32	82.93	63.12	64.90	46.66	61.53	53.21	18.53	24.80	59.48	77.47	43.51	49.94	18.38	95.81	84.05	63.41	72.21	35.97	41.19	
+MAGSAC _I	31.34	96.11	72.54	62.62	66.11	54.79	61.63	44.92	18.84	24.08	71.42	74.07	30.82	47.88	28.51	96.43	74.29	63.52	72.16	36.11	41.39	
+MOP+NCC	0.67	84.83	91.69	31.72	62.89	23.90	56.30	74.04	8.34	24.43	15.86	72.66	83.65	58.91	0.85	93.60	99.08	57.33	72.02	30.81	40.93	
+MAGSAC _T	28.17	95.86	75.93	55.66	63.23	51.17	61.35	48.99	18.28	24.71	42.05	77.48	62.50	55.05	33.48	95.59	72.29	36.03	63.51	41.40		
+MAGSAC _I	32.85	96.34	72.66	63.06	65.35	51.89	63.43	47.76	18.83	24.71	41.60	77.47	30.87	47.24	28.34	96.51	74.45	63.60	72.28	36.19	41.42	
+MOP+MiHo+NCC	0.34	85.06	92.27	33.73	63.47	19.62	57.84	78.37	8.10	24.44	15.81	71.29	82.90	57.77	0.85	84.03	88.71	29.40	70.53	11.65	39.76	
+MAGSAC _T	27.72	96.00	76.50	56.43	61.51	48.65	62.98	51.31	18.08	24.72	41.60	77.40	63.04	54.90	33.19	95.90	69.01	54				

Table 6: LoFTR pipeline evaluation results. All values are percentages, please refer to Sec. 4.2.7. Best viewed in color and zoomed in.

Pipeline	MegaDepth					ScanNet					Planar					IMC Photo/Tourism					
	Filtered	Precision	Recall	AUC ₂ ^F	AUC ₂ ^E	Filtered	Precision	Recall	AUC ₂ ^F	AUC ₂ ^E	Filtered	Precision	Recall	AUC ₂ ^F	AUC ₂ ^E	Filtered	Precision	Recall	AUC ₂ ^F	AUC ₂ ^E	AUC ₂ ^E
LoFTR	0.00	82.27	99.95	16.00	56.97	0.00	58.84	98.82	2.40	36.12	0.00	69.29	92.10	40.09	0.00	79.88	99.95	15.36	62.72	5.81	32.81
+MAGSAC _T	42.45	80.59	64.37	54.87	61.80	48.83	69.72	59.34	30.35	35.64	80.21	74.42	23.88	41.09	47.20	89.44	60.07	51.94	66.51	27.36	36.60
+MAGSAC _L	56.68	91.20	53.36	56.05	62.78	56.06	69.88	51.12	30.37	36.03	85.77	74.04	16.84	39.23	55.66	89.91	50.65	52.85	67.02	27.90	36.98
+ACN _E	41.70	85.75	61.20	25.89	43.29	50.04	65.47	55.50	7.93	27.50	52.17	64.56	50.85	39.06	42.03	85.12	62.27	25.51	51.54	10.31	23.90
+MAGSAC _T	62.94	90.28	41.26	35.99	48.09	66.65	69.38	38.81	18.14	27.84	86.80	73.54	15.70	33.83	65.51	90.07	39.64	38.24	56.05	17.03	26.62
+MAGSAC _L	67.88	90.77	35.81	36.64	48.89	71.02	69.51	33.71	18.41	27.40	90.10	73.73	11.46	32.53	70.70	90.46	33.75	38.57	56.05	17.25	26.85
+AdaLAN	0.00	82.27	99.95	16.00	56.97	0.00	58.84	98.82	2.40	36.12	0.00	60.29	92.10	40.13	0.00	79.88	99.95	15.36	62.69	5.82	32.88
+MAGSAC _T	42.45	90.59	64.37	54.87	61.80	48.83	69.72	59.34	30.35	35.64	80.21	74.42	23.88	41.09	47.20	89.44	60.07	51.94	66.51	27.36	36.60
+MAGSAC _L	56.68	91.20	53.36	56.05	62.78	56.06	69.88	51.12	30.37	36.03	85.77	74.04	16.84	39.23	55.66	89.91	50.65	52.85	67.02	27.90	36.98
+CC	18.43	84.61	85.01	35.38	48.06	27.41	66.75	80.09	14.31	31.16	28.15	49.93	70.97	42.70	n/a	n/a	n/a	n/a	n/a	n/a	n/a
+MAGSAC _T	49.51	89.56	56.25	42.76	54.29	54.21	70.16	53.42	25.19	32.34	85.16	58.09	18.13	30.00	n/a	n/a	n/a	n/a	n/a	n/a	n/a
+MAGSAC _L	56.30	90.07	48.79	43.95	55.27	60.40	70.29	46.18	25.35	31.41	89.12	58.30	13.35	32.54	84.29	58.91	n/a	n/a	n/a	n/a	n/a
+CLNet	19.18	85.42	88.88	20.50	45.60	50.68	67.83	56.28	4.55	24.98	30.33	63.87	73.82	50.51	30.08	85.12	74.48	18.34	50.34	7.56	23.41
+MAGSAC _T	50.24	90.50	53.30	33.70	51.06	64.14	70.13	41.69	12.43	23.94	80.58	71.66	22.66	33.75	58.35	89.74	47.20	31.17	54.99	14.02	26.57
+MAGSAC _L	57.03	90.96	47.84	34.70	52.52	68.71	70.13	36.35	12.80	23.90	86.17	71.95	16.10	32.72	64.57	90.12	40.25	31.74	55.34	14.29	26.81
+ConvMatch	73.11	86.01	26.71	19.28	28.97	77.09	66.71	29.16	7.55	18.21	73.82	63.75	27.60	28.98	74.21	85.78	28.97	22.17	36.68	8.47	15.07
+MAGSAC _T	82.85	87.69	19.15	21.33	30.11	83.61	66.57	21.02	9.24	17.75	92.07	70.99	8.30	24.13	83.19	87.56	19.75	24.01	39.23	9.64	16.43
+MAGSAC _L	85.19	88.03	16.58	21.22	31.50	85.57	66.68	18.39	9.98	18.75	94.86	71.24	5.92	23.68	85.76	87.87	16.77	24.15	39.51	9.71	16.55
+DeMatch	62.46	86.21	89.81	22.54	33.88	65.80	67.56	40.23	7.00	21.59	69.06	63.78	32.65	31.80	63.83	85.42	39.46	23.48	40.36	8.96	17.18
+MAGSAC _T	74.70	89.46	28.00	26.16	37.33	75.20	69.53	29.48	10.74	21.13	90.93	71.76	10.59	28.14	76.79	88.86	26.54	34.11	42.11	11.34	18.46
+MAGSAC _L	78.01	89.85	24.38	26.19	38.22	78.30	69.56	25.71	11.16	20.73	93.20	72.96	7.86	21.44	80.21	89.18	22.68	34.33	41.57	11.29	18.29
+FC-GNN	20.82	93.18	99.03	40.76	66.01	35.61	68.20	73.02	11.47	34.78	31.26	73.37	111.36	61.76	29.50	93.02	89.67	39.30	71.29	20.55	41.68
+MAGSAC _T	86.79	95.38	90.97	64.15	67.32	49.78	71.66	59.17	29.74	34.95	56.14	77.19	79.09	57.18	36.10	95.19	83.69	60.44	71.27	34.82	41.62
+MAGSAC _L	33.53	95.65	86.53	64.44	66.34	54.26	71.63	53.93	29.87	34.22	64.91	77.70	64.16	53.74	39.17	95.45	80.87	50.51	71.20	35.10	41.54
+GMS	16.40	82.84	85.76	36.34	52.68	39.20	66.48	67.45	11.87	31.10	30.91	63.02	73.13	49.71	21.72	84.15	82.53	33.21	58.08	14.86	30.16
+MAGSAC _T	50.45	88.25	55.21	50.49	58.25	58.82	69.20	47.59	25.89	30.96	82.51	71.65	20.96	39.43	55.86	89.46	50.42	48.30	62.77	24.92	33.84
+MAGSAC _L	57.35	88.73	47.63	51.43	58.53	64.34	69.33	41.22	25.47	31.60	87.36	72.11	15.13	32.54	62.74	89.31	42.69	48.91	63.16	25.31	34.25
+MS ² DG-Net	79.12	84.38	22.04	10.61	26.69	71.03	66.45	33.76	1.39	19.26	75.34	62.50	22.95	11.77	75.42	84.08	26.62	10.56	32.36	3.88	13.45
+MAGSAC _T	86.53	88.55	15.20	26.72	31.68	81.09	70.82	23.12	13.67	19.37	95.16	72.30	5.90	23.35	85.25	88.82	19.75	24.01	39.23	9.64	16.43
+MAGSAC _L	88.20	88.93	13.33	27.01	31.93	83.33	70.93	20.35	13.67	19.00	95.29	72.87	4.70	22.65	87.30	89.11	14.80	27.03	37.78	11.68	16.19
+NCINet	17.90	85.69	85.44	19.65	46.39	48.03	67.90	59.37	6.77	27.42	25.68	64.20	78.87	46.07	26.59	85.51	78.54	19.06	51.61	7.82	23.99
+MAGSAC _T	69.34	90.66	56.37	34.15	51.48	62.09	69.92	43.97	14.75	26.65	80.32	73.42	23.65	40.16	56.52	90.09	49.54	31.91	55.90	14.25	26.86
+MAGSAC _L	56.24	91.13	48.80	34.92	51.18	66.96	70.04	38.31	14.80	26.13	85.88	73.62	16.98	33.56	63.07	90.48	42.17	32.30	56.30	14.51	27.29
+OANet	85.69	86.28	15.28	12.63	22.50	84.58	65.07	17.35	4.09	13.25	69.83	62.50	13.12	16.02	86.17	85.15	15.13	11.39	25.55	4.40	9.97
+MAGSAC _T	88.74	88.73	11.31	15.93	24.03	88.04	66.62	18.32	6.66	12.01	95.54	69.14	4.32	19.34	90.51	87.58	10.77	14.79	27.17	5.69	10.48
+MAGSAC _L	90.99	89.02	9.96	16.40	25.14	88.28	66.61	12.27	6.82	12.11	96.77	69.63	3.23	19.48	91.75	87.87	9.37	15.02	27.06	5.71	10.47
+MOP	2.40	83.54	99.37	26.54	56.38	15.45	62.83	90.78	5.84	34.70	16.21	62.50	89.79	51.52	4.13	82.17	98.80	23.50	62.74	9.73	33.07
+MAGSAC _T	42.60	90.73	64.28	54.49	62.29	50.01	70.30	58.60	29.91	36.05	80.27	74.21	24.32	49.84	47.56	89.84	59.88	52.36	66.62	27.43	36.49
+MAGSAC _L	50.77	91.27	53.30	55.54	62.19	57.05	70.48	50.38	29.91	33.57	85.93	74.58	17.42	39.36	55.94	90.31	50.51	52.98	67.39	27.89	37.44
+MOP+NCC	2.40	81.59	11.00	22.98	66.13	15.45	58.09	86.17	5.30	34.23	16.21	62.50	89.79	51.52	4.13	82.17	98.80	23.50	62.74	9.73	33.07
+MAGSAC _T	43.01	95.39	91.16	58.90	66.07	59.36	69.72	48.16	26.72	34.14	49.97	81.91	108.28	64.60	39.36	94.59	84.09	53.80	70.94	30.01	40.61
+MAGSAC _L	38.98	95.65	85.37	60.00	66.09	64.53	69.83	42.03	26.51	33.56	57.99	82.23	93.25	61.93	41.26	85.12	78.18	54.60	70.79	30.39	40.53
+MOP+MiHo+NCC	1.12	82.81	99.83	21.94	56.69	7.96	67.72	98.09	3.82	34.97	11.30	61.59	89.40	46.21	1.93	80.87	99.48	18.88	62.92	7.44	33.14
+MAGSAC _T	42.52	90.64	64.30	54.51	62.52	49.08	69.96	59.54	29.58	35.32	80.03	74.32	24.18	40.97	47.34	89.62	60.02	52.13	66.83	27.49	36.

Table 7: DeDoDe v2 pipeline evaluation results. All values are percentages, please refer to Sec. 4.2.8. Best viewed in color and zoomed in.

Pipeline	MegaDepth				ScanNet				Planar				IMC PhotoTourism									
	Filtered	Precision	Recall	AUC $^F_{\triangle}$	AUC $^E_{\square}$	Filtered	Precision	Recall	AUC $^F_{\square}$	AUC $^E_{\square}$	Filtered	Precision	Recall	AUC $^H_{\square}$	Filtered	Precision	Recall	AUC $^F_{\triangle}$	AUC $^E_{\triangle}$	AUC $^F_{\square}$	AUC $^E_{\square}$	
DeDoDe v2	0.00	68.13	99.99	1.45	65.52	0.00	45.81	99.20	0.50	23.80	0.00	61.15	94.22	26.05	0.00	65.00	100.00	1.43	99.75	0.90	39.93	
+MAGSAC $_{\triangle}$	41.07	92.08	79.43	54.70	65.19	55.42	57.43	59.08	18.48	25.67	63.94	51.71	47.91	51.41	44.09	89.64	77.33	48.58	67.23	26.70	38.01	
+MAGSAC $_{\square}$	47.33	99.73	72.49	96.12	65.46	60.83	56.95	42.74	18.46	24.58	73.76	93.57	35.35	48.55	49.71	90.16	69.92	49.95	66.57	27.57	37.42	
+ACNet	36.27	88.65	83.77	26.57	61.72	50.15	55.36	56.91	6.76	22.56	42.86	72.71	69.10	42.09	41.83	88.89	80.26	23.27	65.59	8.50	33.92	
+MAGSAC $_{\triangle}$	49.19	94.44	71.22	53.89	61.19	64.63	58.01	39.69	15.23	21.99	69.64	80.53	40.75	46.35	53.27	94.17	68.12	51.49	64.99	25.80	33.65	
+MAGSAC $_{\square}$	53.54	94.95	65.44	54.19	61.38	68.48	57.87	34.39	15.34	21.91	77.33	81.00	30.81	43.98	57.32	94.61	62.43	52.12	64.89	26.14	33.50	
+AdaLAM	0.00	68.13	99.99	1.45	65.52	0.00	45.81	99.20	0.50	23.80	0.00	61.15	94.22	26.95	0.00	65.00	100.00	1.43	99.75	0.90	39.93	
+MAGSAC $_{\triangle}$	41.97	92.08	79.43	54.70	65.19	55.42	57.43	50.08	18.48	25.67	63.94	51.71	47.91	51.41	44.09	89.64	77.33	48.58	67.23	26.70	38.01	
+MAGSAC $_{\square}$	47.33	99.73	72.49	96.12	65.46	60.83	56.95	42.74	18.46	24.58	73.76	93.57	35.35	48.55	49.71	90.16	69.92	49.95	66.57	27.57	37.42	
+CC	28.94	87.92	91.15	27.05	64.50	31.95	51.89	74.22	1.99	21.95	54.70	71.75	91.78	52.78	n/a	n/a	n/a	n/a	n/a	n/a	n/a	
+MAGSAC $_{\triangle}$	44.82	94.39	76.46	61.62	64.99	58.93	56.31	45.47	16.02	22.32	63.88	82.26	48.52	51.98	n/a	n/a	n/a	n/a	n/a	n/a	n/a	
+MAGSAC $_{\square}$	49.51	94.96	70.37	62.45	63.95	63.58	55.80	39.06	15.92	22.09	73.53	92.83	35.89	48.41	n/a	n/a	n/a	n/a	n/a	n/a	n/a	
+CLNet	37.67	86.80	79.56	9.05	58.55	60.14	60.30	50.42	2.27	19.43	34.27	72.80	79.12	49.27	43.20	87.73	77.00	11.72	62.85	3.67	32.06	
+MAGSAC $_{\triangle}$	50.61	92.63	67.22	45.63	58.21	71.32	62.43	36.05	9.66	18.89	65.91	80.23	45.16	50.09	54.97	93.15	64.44	44.47	62.10	21.98	31.62	
+MAGSAC $_{\square}$	54.82	93.19	61.88	46.37	58.42	74.61	62.36	31.47	10.16	18.21	74.93	80.75	33.74	47.09	58.98	93.35	58.93	44.92	61.95	22.32	31.60	
+ConvMatch	63.98	85.97	50.05	25.37	47.63	67.44	64.24	46.67	8.78	20.49	78.52	68.37	31.49	40.83	61.92	89.17	58.11	29.81	57.49	10.40	26.31	
+MAGSAC $_{\triangle}$	72.17	88.24	42.96	37.62	47.74	76.91	65.59	32.28	13.18	21.21	88.64	73.33	18.48	28.68	69.21	92.45	48.89	42.64	57.31	17.88	26.16	
+MAGSAC $_{\square}$	74.50	88.65	39.55	38.05	47.64	79.63	63.62	27.58	12.76	20.42	91.15	73.92	14.83	27.85	71.94	92.85	44.66	43.15	57.44	18.24	26.39	
+DoMatch	51.58	88.40	65.18	25.71	55.70	62.96	61.26	48.90	5.93	20.56	63.15	73.22	46.84	37.89	54.50	88.96	65.11	27.37	60.98	10.51	29.96	
+MAGSAC $_{\triangle}$	60.86	93.17	55.48	43.23	55.20	73.43	63.02	33.97	11.25	20.06	79.35	80.49	28.83	40.20	63.47	93.60	54.64	45.13	60.41	21.40	29.52	
+MAGSAC $_{\square}$	64.13	93.66	51.05	44.58	55.29	76.48	63.05	29.51	11.40	21.74	84.09	81.07	22.44	37.50	66.70	94.03	49.94	45.51	60.40	21.65	29.64	
+FC-GNN	35.70	88.47	84.89	5.81	67.65	46.24	55.08	63.54	1.46	28.24	31.79	73.66	84.25	42.00	39.90	86.27	80.50	7.35	70.72	3.69	41.18	
+MAGSAC $_{\triangle}$	42.00	98.01	81.14	62.33	66.52	62.27	67.21	48.62	21.20	27.65	52.83	81.32	61.91	54.72	46.79	63.21	76.07	66.34	69.54	32.72	40.13	
+MAGSAC $_{\square}$	43.61	98.28	79.07	63.77	66.86	64.99	62.61	41.75	21.76	61.19	81.30	51.32	51.79	48.43	63.47	79.85	57.23	69.30	33.33	39.72		
+GMS	35.28	84.67	79.47	20.52	63.31	34.47	52.34	72.11	1.66	22.20	35.76	71.53	74.96	43.60	41.39	84.78	75.61	15.59	65.32	6.55	36.27	
+MAGSAC $_{\triangle}$	50.03	92.41	66.79	60.34	63.82	61.27	56.99	43.55	16.42	21.47	67.33	80.04	42.77	48.08	55.34	92.37	62.59	64.45	29.57	35.61		
+MAGSAC $_{\square}$	54.28	92.94	61.47	60.70	63.26	65.71	56.33	37.11	16.26	21.74	76.02	80.50	31.60	45.53	59.31	92.27	57.27	53.34	64.15	29.83		
+MS ² DG-Net	72.45	83.39	37.19	1.26	47.41	70.63	54.46	34.68	0.23	12.31	77.04	66.53	27.37	6.84	71.35	80.62	38.93	0.81	48.92	0.39	21.26	
+MAGSAC $_{\triangle}$	79.49	91.85	31.19	44.19	46.00	81.00	57.11	21.56	7.08	12.00	88.92	77.26	16.02	30.00	78.81	88.87	32.30	35.14	48.26	14.38	21.04	
+MAGSAC $_{\square}$	81.11	92.37	28.85	44.85	46.90	82.81	56.63	18.79	7.30	91.34	78.02	12.52	27.83	80.56	89.25	29.69	36.13	47.95	15.12	20.88		
+NCNNet	36.94	87.89	81.66	8.97	58.90	60.19	61.93	52.13	4.17	21.60	32.51	72.49	80.82	49.74	41.67	89.05	80.63	12.81	63.42	4.23	32.30	
+MAGSAC $_{\triangle}$	49.86	93.73	69.12	47.03	58.91	71.50	64.25	37.63	12.21	20.63	64.81	80.00	46.39	50.52	53.57	94.10	67.48	44.75	62.73	21.47	31.54	
+MAGSAC $_{\square}$	54.12	94.22	63.57	47.67	58.75	74.98	64.17	32.65	12.17	21.07	74.28	80.16	34.18	47.16	57.68	94.54	61.71	45.03	62.61	21.74	31.66	
+OANet	71.66	87.03	38.28	11.25	49.22	70.95	48.08	19.35	2.15	20.91	80.47	71.27	25.80	15.23	74.87	88.18	36.17	12.63	51.54	3.46	22.58	
+MAGSAC $_{\triangle}$	76.92	92.92	32.98	35.82	47.97	88.80	49.99	11.59	5.35	9.75	88.91	79.18	15.73	33.77	79.38	92.73	31.02	33.43	50.90	13.61	22.20	
+MAGSAC $_{\square}$	73.79	93.36	30.42	36.47	48.33	61.37	57.29	42.67	18.45	24.60	73.90	82.96	35.85	49.14	50.38	94.04	69.99	53.09	67.40	30.05	37.90	
+MOP	16.42	78.18	97.59	3.24	66.52	13.11	49.21	63.08	0.93	24.28	21.44	67.83	89.58	38.81	17.97	67.35	97.24	4.81	69.97	2.41	39.89	
+MAGSAC $_{\triangle}$	42.39	93.44	79.74	57.82	65.85	56.17	55.72	54.79	45.01	18.17	25.71	63.87	82.06	48.71	52.47	45.01	91.13	77.20	51.89	67.93	29.28	38.28
+MAGSAC $_{\square}$	47.61	94.06	72.90	59.56	65.59	61.01	57.22	42.99	17.86	24.74	73.61	82.50	35.81	48.52	49.93	90.82	70.09	51.49	66.77	29.02	37.76	
+MOP+NCC	16.42	74.90	95.46	2.09	66.60	7.12	47.60	46.70	0.96	0.69	24.90	16.32	65.17	90.76	32.89	10.71	71.24	98.92	2.66	70.07	1.44	40.06
+MAGSAC $_{\triangle}$	42.13	92.63	79.61	55.86	65.73	55.72	54.79	50.10	18.17	25.71	63.87	82.06	48.71	52.47	45.01	90.30	77.44	50.29	67.55	28.08	38.03	
+MAGSAC $_{\square}$	47.44	93.33	72.79	57.01	65.23	61.01	57.22	42.99	17.86	24.74	73.61	82.50	35.81	48.52	49.93	90.82	70.09	51.49	66.77	29.02	37.76	
+MOP+MH Θ +NCC	9.62	73.39	99.19	2.13	67.04	7.12	47.60	46.70	0.96	0.69	24.90	16.32	65.17	90.76	33.79	10.71	71.24	98.92	2.66	70.07	1.44	40.06
+MAGSAC $_{\triangle}$	44.22	93.50	77.88	53.33	65.29	54.59	57.63	51.95	17.94	25.60	49.00	81.65	6									

Table 9: Average number of matches per image pair for the base matching pipelines, the highest value for each dataset is in bold. Please refer to Sec. 4.2.1.

	MegaDepth	ScanNet	Planar	IMC-PT
SIFT+NNR	1187	406	1038	871
Key.Net+ ^{AffNet} _{HardNet} +NNR	1212	282	1190	866
SuperPoint+LightGlue	758	195	993	599
ALIKED+LightGlue	910	171	998	880
DISK+LightGlue	2424	823	2472	2286
LoFTR	3258	807	2662	1968
DeDoDe v2	2246	1196	2205	1832

also that deep-architecture is parallel by design while MOP-based computation inherits RANSAC serialization. Nevertheless, better optimization to adaptively determine the stopping criteria and to avoid redundant computation dynamically or in a coarse-to-fine manner are planned as future work.

Overall, according to the running time data, it turns out that the default value $c_{\max}=2000$ used for the main comparative evaluation in Tables 1-7 is optimal in terms of matching quality only for SIFT and Key.Net, while it slightly decreases the matching results for the other pipelines with respect to $c_{\max}=500$, which also improves the running times. In detail, moving from $c_{\max}=500$ to $c_{\max}=2000$ causes an increment of around 2% of the recall and of about 1% for the AUC pose estimation in the case of SIFT and Key.Net, which contain as initial configuration a higher number of outliers than other pipelines, for which both recall and pose AUC remain instead stable or even worsen. This can be motivated by observing that the next homography discovered in MOP-based approaches is more noisy or even not correct in the long run than the previous ones, and high c_{\max} values force to retrieve a plane and delay the iteration stops. According to these considerations, it is reasonable that forcing the homography retrieval by increasing c_{\max} starts to degrade the found solutions as the initial outlier ratio decreases.

Notice also that MiHo can take part in the MOP early stopping since it introduces further constraints in the homography to be searched, justifying higher running times for MOP than those of MOP+MiHo in some configurations, although MiHo should ideally need more computational resources as two tied homographies are estimated at each step instead of only one. In particular, MOP+MiHo running time equals MOP one for LoFTR and DeDoDe v2, it is greater for SuperPoint, ALIKED, and DISK, and it is

lower for SIFT and Key.Net. Excluding SIFT and Key.Net, MOP+MiHo find more homographies than MOP, suggesting the reliability of the organization of input matches within the scene as almost-similarity transformations.

5 Conclusions and future work

This paper presented a novel handcrafted modular approach to filtering and refining image matches relying on the principle that the scene flow can be approximated as virtual local and overlapping planar homographies. Extensive evaluation shows that the approach is valid and robust.

MOP+MiHo+NCC is able to effectively discard outliers and to improve the match localization as well as the pose accuracy with Key.Net, SuperPoint, and LoFTR. MOP+MiHo without NCC filtering is able to remove outliers within SIFT providing a better RANSAC estimation as well. In the case of ALIKED, DISK, and DeDoDe v2, where the base pipeline only contains accurate matches, the proposed pipeline does not alter the final output. Nevertheless, in terms of absolute accuracy, LoFTR and SuperPoint reached the overall best results among all the evaluated pipelines when boosted by the proposed approach in three of the evaluated datasets, while in the remaining IMC-PT dataset, the best is reached by DISK with FC-GNN, which is the current deep competitor and alternative to MOP+MiHo+NCC.

Overall, the above behavior suggests that current end-to-end deep base matching architecture are in general too strict in removing non-accurate matches which could be refined. In this sense, the proposed analysis and the designed approaches provide further insight that can be used for developing better deep image matching networks. FC-GNN provides better pose estimation than

the proposed method for unknown camera intrinsics, with a minimal gap with respect to the pose estimation with known camera intrinsics in MegaDepth. Future research will involve the inclusion of camera intrinsic statistics and heuristics within the RANSAC framework.

MOP has proved to be effective in finding spatial planar clusters. As future work these clusters could be organized and exploited more in-depth to further filter matches as well as to expand them within the framework described in [50]. Moreover, planar clusters could be used also to characterize the scene structure at higher levels in terms of object segmentation and the relative positions and occlusions of the found elements.

MiHo is able to improve the alignment in almost-planar motion, yet it lacks a rigorous mathematical formulation which would help to better understand its properties and limitations. Future development in this direction will be explored, as well as its possible applications to current image stitching solutions.

NCC inherits the strengths and weaknesses of the base template matching approach it is based on. NCC is effective on corner-like patches but on strong edge-like structures or flat homogeneous regions, more typical of blobs, NCC can mislead the alignment refinement. More elaborated and robust approaches based on the gradient orientation histogram correlation, on the Iterative Closest Point (ICP) [110] or variational methods will be taken in consideration for future developments. Match densification through local patch homographies will be investigated too.

MOP+MiHo+NCC shifts the same initial keypoint belonging to an image in different directions when this image is paired with other images of the same scene. This implies that the proposed method cannot be embedded directly within current SfM pipelines since it would prevent the generation of keypoint tracks. Solutions for handling multiple keypoint shifts in SfM, for instance by constraint keypoint refinement to only one image by a greedy strategy as more images are added to the model, will be evaluated in future work.

MOP+MiHo+NCC offers the advantage of handcrafted design with respect to deep architectures, including explainability, direct design tuning, and adaptability for specific tasks and no training data dependence. Nevertheless,

MOP+MiHo+NCC sequential nature inherited by RANSAC makes it less efficient in terms of computation in nowadays parallel hardware and programming infrastructures exploited straightly by deep networks. Future works will investigate design approaches and optimization strategies to speed up the computational times.

Finally, the reported comprehensive comparative analysis highlighted several critical aspects in current image matching methods, including the dependency of the filtering methods on the specific dataset and the base pipeline, as well as the pose estimation performance drop observed when camera intrinsic are unknown, quite common in real scenarios. This evaluation will be extended to additional approaches and further complex datasets.

References

- [1] Brown M, Lowe DG. Automatic Panoramic Image Stitching using Invariant Features. *International Journal of Computer Vision*. 2007;74:59–73.
- [2] Szeliski R. *Computer Vision: Algorithms and Applications*. 2nd ed. Springer-Verlag; 2022.
- [3] Snavely N, Seitz SM, Szeliski R. Modeling the World from Internet Photo Collections. *International Journal of Computer Vision*. 2008;80(2):189–210.
- [4] Schönberger J, Frahm JM. Structure-from-Motion Revisited. In: *Proceedings of the IEEE Conference on Computer Vision and Pattern Recognition (CVPR)*; 2016. p. 4104–4113.
- [5] Pan L, Barath D, Pollefeys M, Schönberger J. Global Structure-from-Motion Revisited. In: *Proceedings of the European Conference on Computer Vision (ECCV)*; 2024. p. 4104–4113.
- [6] Mur-Artal R, Montiel JMM, Tardos JD. ORB-SLAM: a Versatile and Accurate Monocular SLAM System. *IEEE Transactions on Robotics*. 2015;31(5):1147–1163.

[7] Mildenhall B, Srinivasan PP, Tancik M, Barron JT, Ramamoorthi R, Ng R. NeRF: Representing Scenes as Neural Radiance Fields for View Synthesis. In: Proceedings of the European Conference on Computer Vision (ECCV); 2020. p. 405–421.

[8] Gao K, Gao Y, He H, Lu D, Xu L, Li J. NeRF: Neural Radiance Field in 3D Vision, A Comprehensive Review. In: arXiv:2210.00379; 2023. .

[9] Kerbl B, Kopanas G, Leimkuehler T, Dretak G. 3D Gaussian Splatting for Real-Time Radiance Field Rendering. ACM Transactions on Graphics. 2023;42(4):1–14.

[10] Chen G, Wang W. A Survey on 3D Gaussian Splatting. In: arXiv:2401.03890; 2024. .

[11] Jin Y, Mishkin D, Mishchuk A, Matas J, Fua P, Yi KM, et al. Image Matching across Wide Baselines: From Paper to Practice. International Journal of Computer Vision. 2021;129(2):517–547.

[12] Lindenberger P, Sarlin PE, Pollefeys M. LightGlue: Local Feature Matching at Light Speed. In: Proceedings of the International Conference on Computer Vision (ICCV); 2023. p. 17627–17638.

[13] Zhao X, Wu X, Chen W, Chen PCY, Xu Q, Li Z. ALIKED: A Lighter Keypoint and Descriptor Extraction Network via Deformable Transformation. IEEE Transactions on Instrumentation and Measurement. 2023;72:1–16.

[14] Sun J, Shen Z, Wang Y, Bao H, Zhou X. LoFTR: Detector-Free Local Feature Matching with Transformers. In: Proceedings of the IEEE Conference on Computer Vision and Pattern Recognition (CVPR); 2021. p. 8922–8931.

[15] Tang S, Zhang J, Zhu S, Tan P. QuadTree Attention for Vision Transformers. In: Proceedings of the International Conference on Learning Representations (ICLR); 2022. .

[16] Wang Q, Zhang J, Yang K, Peng K, Stiefelhagen R. MatchFormer: Interleaving Attention in Transformers for Feature Matching. In: Proceedings of the Asian Conference on Computer Vision (ACCV); 2022. p. 2746–2762.

[17] Wang S, Leroy V, Cabon Y, Chidlovskii B, Revaud J. DUSt3R: Geometric 3D Vision Made Easy. In: Proceedings of the IEEE/CVF Conference on Computer Vision and Pattern Recognition (CVPR); 2024. p. 20697–20709.

[18] Edstedt J, Sun Q, Bökman G, Wadenbäck M, Felsberg M. RoMa: Robust Dense Feature Matching. In: Proceedings of the IEEE/CVF Conference on Computer Vision and Pattern Recognition (CVPR); 2024. p. 19790–19800.

[19] Lowe DG. Distinctive Image Features from Scale-invariant Keypoints. International Journal of Computer Vision. 2004;60(2):91–110.

[20] Fischler M, Bolles R. Random Sample Consensus: A Paradigm for Model Fitting with Applications to Image Analysis and Automated Cartography. Communications of the ACM. 1981;24(6):381–395.

[21] Raguram R, Chum O, Pollefeys M, Matas J, Frahm J. USAC: A Universal Framework for Random Sample Consensus. IEEE Transactions on Pattern Analysis and Machine Intelligence. 2013;35(8):2022–2038.

[22] Barath D, Matas J. Graph-cut RANSAC. In: Proceedings of the IEEE Conference on Computer Vision and Pattern Recognition (CVPR); 2018. p. 6733–6741.

[23] Barath D, Matas J, Noskova J. MAGSAC: Marginalizing Sample Consensus. In: Proceedings of the IEEE Conference on Computer Vision and Pattern Recognition (CVPR); 2019. p. 10197–10205.

[24] Chum O, Werner T, Matas J. Two-View Geometry Estimation Unaffected by a Dominant Plane. In: Proceedings of the IEEE

Conference on Computer Vision and Pattern Recognition (CVPR). vol. 1; 2005. p. 772–779.

[25] Ma J, Zhao J, Jiang J, Zhou H, Guo X. Locality Preserving Matching. International Journal of Computer Vision. 2019;127(5):512–531.

[26] Bian JW, Lin WY, Liu Y, Zhang L, Yeung SK, Cheng MM, et al. GMS: Grid-Based Motion Statistics for Fast, Ultra-robust Feature Correspondence. International Journal of Computer Vision. 2020;128:1580–1593.

[27] Cho M, Lee KM. Progressive graph matching: Making a move of graphs via probabilistic voting. In: Proceedings of the IEEE Conference on Computer Vision and Pattern Recognition (CVPR); 2012. p. 398–405.

[28] Lee S, Lim J, Suh IH. Progressive Feature Matching: Incremental Graph Construction and Optimization. IEEE Transactions on Image Processing. 2020;29:6992–7005.

[29] Ma J, Zhao J, Tian J, Yuille AL, Tu Z. Robust point matching via vector field consensus. IEEE Transactions on Image Processing. 2014;23(4):1706–1721.

[30] Lin W, Wang F, Cheng M, Yeung S, Torr PHS, Do MN, et al. CODE: Coherence Based Decision Boundaries for Feature Correspondence. IEEE Transactions on Pattern Analysis and Machine Intelligence. 2018;40(1):34–47.

[31] Lin WYD, Cheng MM, Lu J, Yang H, Do MN, Torr P. Bilateral Functions for Global Motion Modeling. In: Proceedings of the European Conference on Computer Vision (ECCV); 2014. p. 341–356.

[32] Bellavia F. SIFT Matching by Context Exposed. IEEE Transactions on Pattern Analysis and Machine Intelligence. 2023;45(2):2445–2457.

[33] Cavalli L, Larsson V, Oswald MR, Sattler T, Pollefeys M. AdALAM: Handcrafted Outlier Detection Revisited. In: Proceedings of the European Conference on Computer Vision (ECCV); 2020. p. 770–787.

[34] Yi KM, Trulls E, Ono Y, Lepetit V, Salzmann M, Fua P. Learning to Find Good Correspondences. In: Proceedings of the IEEE Conference on Computer Vision and Pattern Recognition (CVPR); 2018. p. 2666–2674.

[35] Sun W, Jiang W, Trulls E, Tagliasacchi A, Yi KM. ACNe: Attentive Context Normalization for Robust Permutation-Equivariant Learning. In: Proceedings of the IEEE Conference on Computer Vision and Pattern Recognition (CVPR); 2020. p. 11286–11295.

[36] Zhang J, Sun D, Luo Z, Yao A, Zhou L, Shen T, et al. Learning Two-View Correspondences and Geometry Using Order-Aware Network. In: Proceedings of the IEEE/CVF International Conference on Computer Vision (ICCV); 2019. p. 5844–5853.

[37] Zhao C, Ge Y, Zhu F, Zhao R, Li H, Salzmann M. Progressive Correspondence Pruning by Consensus Learning. In: Proceedings of the IEEE International Conference on Computer Vision (ICCV); 2021. p. 6464–6473.

[38] Liu X, Qin R, Yan J, Yang J. NCM-Net: Neighbor Consistency Mining Network for Two-View Correspondence Pruning. IEEE Transactions on Pattern Analysis and Machine Intelligence. 2024; p. 1–19.

[39] Dai L, Liu Y, Ma J, Wei L, Lai T, Yang C, et al. MS²DG-Net: Progressive Correspondence Learning via Multiple Sparse Semantics Dynamic Graph. In: Proceedings of the IEEE/CVF Conference on Computer Vision and Pattern Recognition (CVPR); 2022. p. 8973–8982.

[40] Zhang S, Ma J. ConvMatch: Rethinking Network Design for Two-View Correspondence Learning. IEEE Transactions on Pattern Analysis and Machine Intelligence. 2023;46:2920–2935.

[41] Zhang S, Li Z, Gao Y, Ma J. DeMatch: Deep Decomposition of Motion Field for Two-View Correspondence Learning. In: Proceedings of the IEEE/CVF Conference on Computer Vision and Pattern Recognition (CVPR); 2024. p. 20278–20287.

[42] Zhou Q, Sattler T, Leal-Taixe L. Patch2Pix: Epipolar-Guided Pixel-Level Correspondences. In: Proceedings of the IEEE/CVF Conference on Computer Vision and Pattern Recognition (CVPR); 2021. p. 4669–4678.

[43] Kim S, Pollefeys M, Barath D. Learning to Make Keypoints Sub-Pixel Accurate. In: Proceedings of the European Conference on Computer Vision (ECCV); 2024. .

[44] Xu H, Zhou J, Yang H, Pan R, Li C. FC-GNN: Recovering Reliable and Accurate Correspondences from Interferences. In: Proceedings of the IEEE/CVF Conference on Computer Vision and Pattern Recognition (CVPR); 2024. p. 25213–25222.

[45] Hartley RI, Zisserman A. Multiple View Geometry in Computer Vision. Cambridge University Press; 2000.

[46] Kanazawa Y, Kawakami H. Detection of Planar Regions with Uncalibrated Stereo using Distributions of Feature Points. In: Proceedings of the British Machine Vision Conference (BMVC); 2004. p. 1–10.

[47] Vincent E, Laganiere R. Detecting planar homographies in an image pair. In: Proceedings of the International Symposium on Image and Signal Processing and Analysis; 2001. p. 182–187.

[48] Gonzales R, Woods RE. Digital Image Processing. 4th ed. Pearson College Division; 2017.

[49] Bellavia F, Morelli L, Colombo C, Remondino F. Progressive Keypoint Localization and Refinement in Image Matching. In: Proceeding of the Image Analysis and Processing Workshops (ICIAPW); 2023. p. 322–334.

[50] Bellavia F. Image Matching by Bare Homography. *IEEE Transactions on Image Processing*. 2024;33:696–708.

[51] Bellavia F, Colombo C. Estimating the best reference homography for planar mosaics from videos. In: Proceedings International Conference on Computer Vision Theory and Applications (VISAPP); 2015. p. 512–519.

[52] Barroso-Laguna A, Riba E, Ponsa D, Mikolajczyk K. KeyNet: Keypoint Detection by Handcrafted and Learned CNN Filters. In: Proceedings of the International Conference on Computer Vision (ICCV); 2019. p. 5836–5844.

[53] DeTone D, Malisiewicz T, Rabinovich A. SuperPoint: Self-Supervised Interest Point Detection and Description. In: Proceedings of the IEEE Conference on Computer Vision and Pattern Recognition (CVPR); 2018. p. 224–236.

[54] Li Z, Snavely N. MegaDepth: Learning Single-View Depth Prediction from Internet Photos. In: Proceedings of the IEEE Conference on Computer Vision and Pattern Recognition (CVPR); 2018. p. 2041–2050.

[55] Dai A, Chang AX, Savva M, Halber M, Nießner TFM. ScanNet: Richly-Annotated 3D Reconstructions of Indoor Scenes. In: Proceedings of the IEEE Conference on Computer Vision and Pattern Recognition (CVPR); 2017. p. 5828–5839.

[56] Balntas V, Lenc K, Vedaldi A, Mikolajczyk K. HPatches: A Benchmark and Evaluation of Handcrafted and Learned Local Descriptors. In: Proceedings of the IEEE Conference on Computer Vision and Pattern Recognition (CVPR); 2017. p. 3852–3861.

[57] Mishkin D, Matas J, Perdoch M. MODS: Fast and robust method for two-view matching. *Computer Vision and Image Understanding*. 2015;141:81–93.

[58] Ma J, Jiang J, Fan A, Jiang J, Yan J. Image Matching from Handcrafted to Deep Features: A Survey. *International Journal of*

Computer Vision. 2021;129(7):23–79.

[59] Xu S, Chen S, Xu R, Wang C, Lu P, Guo L. Local Feature Matching Using Deep Learning: A Survey. *Information Fusion*. 2024;107:102344.

[60] Tuytelaars T, Mikolajczyk K. Local Invariant Feature Detectors: A Survey. vol. 3. *Foundations and Trends in Computer Graphics and Vision*; 2008.

[61] Fan B, Wang Z, Wu F. Local Image Descriptor: Modern Approaches. vol. 108. Springer; 2016.

[62] Harris C, Stephens M. A Combined Corner and Edge Detector. In: *Proceedings of the 4th Alvey Vision Conference*; 1988. p. 147–151.

[63] Alcantarilla PF, Nuevo J, Bartoli A. Fast Explicit Diffusion for Accelerated Features in Nonlinear Scale Space. In: *Proceedings of the British Machine Vision Conference (BMVC)*. vol. 34; 2013. p. 1281–1298.

[64] Bay H, Ess A, Tuytelaars T, Van Gool L. Speeded-Up Robust Features (SURF). *Computer Vision and Image Understanding*. 2008;110(3):346–359.

[65] Rosten E, Drummond T. Machine Learning for High-Speed Corner Detection. In: *Proceedings of the European Conference on Computer Vision (ECCV)*; 2006. p. 430–443.

[66] Santellani E, Zach M, Sormann C, Rossi M, Kuhn A, Fraundorfer F. GMM-IKRS: Gaussian Mixture Models for Interpretable Keypoint Refinement and Scoring. In: *arXiv:2408.17149*; 2024. .

[67] Morel JM, Yu G. ASIFT: A New Framework for Fully Affine Invariant Image Comparison. *SIAM Journal on Imaging Sciences*. 2009;2(2):438–469.

[68] Rublee E, Rabaud V, Konolige K, Bradski G. ORB: An efficient alternative to SIFT or SURF. In: *Proceedings of the IEEE International Conference on Computer Vision (ICCV)*; 2011. p. 2564–2571.

[69] R Elvira JMM M J D Tardós. CudaSIFT-SLAM: multiple-map visual SLAM for full procedure mapping in real human endoscopy. In: *arXiv:2405.16932*; 2024. .

[70] Mikolajczyk K, Schmid C. Scale & affine invariant interest point detectors. *International Journal of Computer Vision*. 2004;60(1):63–86.

[71] Barath D. On Making SIFT Features Affine Covariant. *International Journal of Computer Vision*. 2023;131(9):2316–2332.

[72] Bellavia F, Colombo C. Rethinking the SGLOH Descriptor. *IEEE Transactions on Pattern Analysis and Machine Intelligence*. 2018;40(4):931–944.

[73] Lenc K, Matas J, Mishkin D. A Few Things One Should Know About Feature Extraction, Description and Matching. In: *Proceedings of the Computer Vision Winter Workshop (CVWW)*; 2014. p. 67–74.

[74] Ma J, Jiang J, Zhou H, Zhao J, Guo X. Guided Locality Preserving Feature Matching for Remote Sensing Image Registration. *IEEE Transactions on Geoscience and Remote Sensing*. 2018;56(8):4435–4447.

[75] Chum O, Matas J. Matching with PROSAC - progressive sample consensus. In: *Proceedings of the IEEE Conference on Computer Vision and Pattern Recognition (CVPR)*; 2005. p. 220–226.

[76] Ni N, Hailin J, Dellaert F. GroupSAC: Efficient consensus in the presence of groupings. In: *Proceedings of the IEEE International Conference on Computer Vision (ICCV)*; 2009. p. 2193–2200.

[77] Toldo R, Fusiello A. Robust Multiple Structures Estimation with J-Linkage. In: *Proceedings of the European Conference on Computer Vision (ECCV)*; 2008. p. 537–547.

[78] Barath D, Matas J. Progressive-X: Efficient, Anytime, Multi-Model Fitting Algorithm. In: Proceedings of the IEEE International Conference on Computer Vision (ICCV); 2019. p. 3780–3788.

[79] Barath D, Rozumnyi D, Eichhardt I, Hajder L, Matas J. Finding Geometric Models by Clustering in the Consensus Space. In: Proceedings of the IEEE/CVF Conference on Computer Vision and Pattern Recognition (CVPR); 2023. p. 5414–5424.

[80] Mishchuk A, Mishkin D, Radenovic F, Matas J. Working Hard to Know Your Neighbor’s Margins: Local Descriptor Learning Loss. In: Proceedings of the Conference on Neural Information Processing Systems (NeurIPS); 2017. .

[81] Tian Y, Yu X, Fan B, Wu F, Heijnen H, Balntas V. SOSNet: Second Order Similarity Regularization for Local Descriptor Learning. In: Proceedings of the IEEE Conference on Computer Vision and Pattern Recognition (CVPR); 2019. p. 11016–11025.

[82] Tian Y, Laguna AB, Ng T, Balntas V, Mikolajczyk K. HyNet: Learning Local Descriptor with Hybrid Similarity Measure and Triplet Loss. In: Proceedings of the Conference on Neural Information Processing Systems (NeurIPS). vol. 33; 2020. p. 7401–7412.

[83] Yi KM, Verdie Y, Fua P, Lepetit V. Learning to Assign Orientations to Feature Points. In: Proceedings of the IEEE Conference on Computer Vision and Pattern Recognition (CVPR); 2016. p. 107–116.

[84] Mishkin D, Radenovic F, Matas J. Repeatability Is Not Enough: Learning Affine Regions via Discriminability. In: Proceedings of the European Conference on Computer Vision (ECCV); 2018. p. 284–300.

[85] Bellavia F, Mishkin D. HarrisZ⁺: Harris Corner Selection for Next-Gen Image Matching Pipelines. Pattern Recognition Letters. 2022;158:141–147.

[86] Yi KM, Trulls E, Lepetit V, Fua P. LIFT: Learned Invariant Feature Transform. In: Proceedings of the European Conference on Computer Vision (ECCV); 2016. p. 467–483.

[87] Revaud J, Weinzaepfel P, de Souza CR, Humenberger M. R2D2: Repeatable and Reliable Detector and Descriptor. In: Proceedings of the 32nd Conference on Neural Information Processing Systems (NeurIPS). vol. 32; 2019. .

[88] Zhao X, Wu X, Miao J, Chen W, Chen PCY, Li Z. ALIKE: Accurate and Lightweight Keypoint Detection and Descriptor Extraction. IEEE Transactions on Multimedia. 2022;25:3101–3112.

[89] Tyszkiewicz MJ, Fua P, Trulls E. DISK: Learning local features with policy gradient. In: Proceedings of the 32nd Conference on Neural Information Processing Systems (NeurIPS). vol. 33; 2020. p. 14254–14265.

[90] Dusmanu M, Rocco I, Pajdla T, Pollefeys M, Sivic J, Torii A, et al. D2-Net: A Trainable CNN for Joint Detection and Description of Local Features. In: Proceedings of the 2019 IEEE/CVF Conference on Computer Vision and Pattern Recognition (CVPR); 2019. p. 8084–8093.

[91] Tian Y, Balntas V, Ng T, Laguna AB, Demiris Y, Mikolajczyk K. D2D: Keypoint Extraction with Describe to Detect Approach. In: Proceedings of the 15th Asian Conference on Computer Vision (ACCV); 2020. p. 223–240.

[92] Edstedt J, Bökman G, Wadenbäck M, Felsberg M. DeDoDe: Detect, Don’t Describe — Describe, Don’t Detect for Local Feature Matching. In: International Conference on 3D Vision (3DV); 2024. p. 148–157.

[93] Edstedt J, Bökman G, Zhao Z. DeDoDe v2: Analyzing and Improving the DeDoDe Keypoint Detector. In: Proceedings of the IEEE/CVF Conference on Computer Vision and Pattern Recognition (CVPR); 2024. p. 4245–4253.

[94] Sarlin PE, DeTone D, Malisiewicz T, Rabинovich A. SuperGlue: Learning Feature Matching with Graph Neural Networks. In: Proceedings of the IEEE Conference on Computer Vision and Pattern Recognition (CVPR); 2020. p. 4938–4947.

[95] Bökman G, Kahl F. A case for using rotation invariant features in state of the art feature matchers. In: Proceedings of the IEEE/CVF Conference on Computer Vision and Pattern Recognition (CVPR); 2022. p. 5110–5119.

[96] Bökman G, Edstedt J, Felsberg M, Kahl F. Steerers: A framework for rotation equivariant keypoint descriptors. In: Proceedings of the IEEE/CVF Conference on Computer Vision and Pattern Recognition (CVPR); 2024. p. 4885–4895.

[97] Santellani E, Sormann C, Rossi M, Kuhn A, Fraundorfer F. S-TREK: Sequential Translation and Rotation Equivariant Keypoints for local feature extraction. In: Proceedings of the IEEE International Conference on Computer Vision (ICCV); 2023. p. 9694–9703.

[98] Vaswani A, Shazeer N, Parmar N, Uszkoreit J, Jones L, Gomez AN, et al. Attention is all you need. In: Proceedings of the International Conference on Neural Information Processing Systems (NeurIPS); 2017. .

[99] Brachmann E, Rother C. Neural-Guided RANSAC: Learning Where to Sample Model Hypotheses. In: Proceedings of the IEEE/CVF International Conference on Computer Vision (ICCV); 2019. p. 4321–4330.

[100] Wei T, Patel Y, Shekhovtsov A, Matas J, Barath D. Generalized differentiable RANSAC. In: Proceedings of the IEEE/CVF International Conference on Computer Vision (ICCV); 2023. p. 17649–17660.

[101] Lindenberger P, Sarlin PE, Larsson V, Pollefeys M. Pixel-Perfect Structure-from-Motion with Featuremetric Refinement. In: Proceedings of the IEEE International Conference on Computer Vision (ICCV); 2021. p. 5987–5997.

[102] Trucco E, Verri A. Introductory Techniques for 3-D Computer Vision. Prentice Hall; 1998.

[103] Bradski G. The OpenCV Library. Dr Dobb's Journal of Software Tools. 2000;.

[104] Arandjelović R, Zisserman A. Three things everyone should know to improve object retrieval. In: Proceedings of the IEEE Conference on Computer Vision and Pattern Recognition (CVPR); 2012. p. 2911–2918.

[105] Riba E, Mishkin D, Ponsa D, Rublee E, Bradski G. Kornia: an Open Source Differentiable Computer Vision Library for PyTorch. In: Winter Conference on Applications of Computer Vision; 2020. p. 3674–3683.

[106] Heinly J, Schönberger JL, Dunn E, Frahm JM. Reconstructing the World* in Six Day *(As Captured by the Yahoo 100 Million Image Dataset). In: Proceedings of the IEEE Conference on Computer Vision and Pattern Recognition (CVPR); 2015. p. 3287–3295.

[107] Nister D. An efficient solution to the five-point relative pose problem. IEEE Transactions on Pattern Analysis and Machine Intelligence. 2004;26(6):756–770.

[108] Barath D, Mishkin D, and W Förstner MP, Matas J. A Large Scale Homography Benchmark. In: Proceedings of the IEEE Conference on Computer Vision and Pattern Recognition (CVPR); 2023. p. 21360–21370.

[109] Chum O, Matas J, Kittler J. Locally Optimized RANSAC. In: Pattern Recognition, 25th DAGM Symposium; 2003. p. 236–243.

[110] Besl PJ, McKay ND. A method for registration of 3-D shapes. IEEE Transactions on Pattern Analysis and Machine Intelligence. 1992;14:239–256.

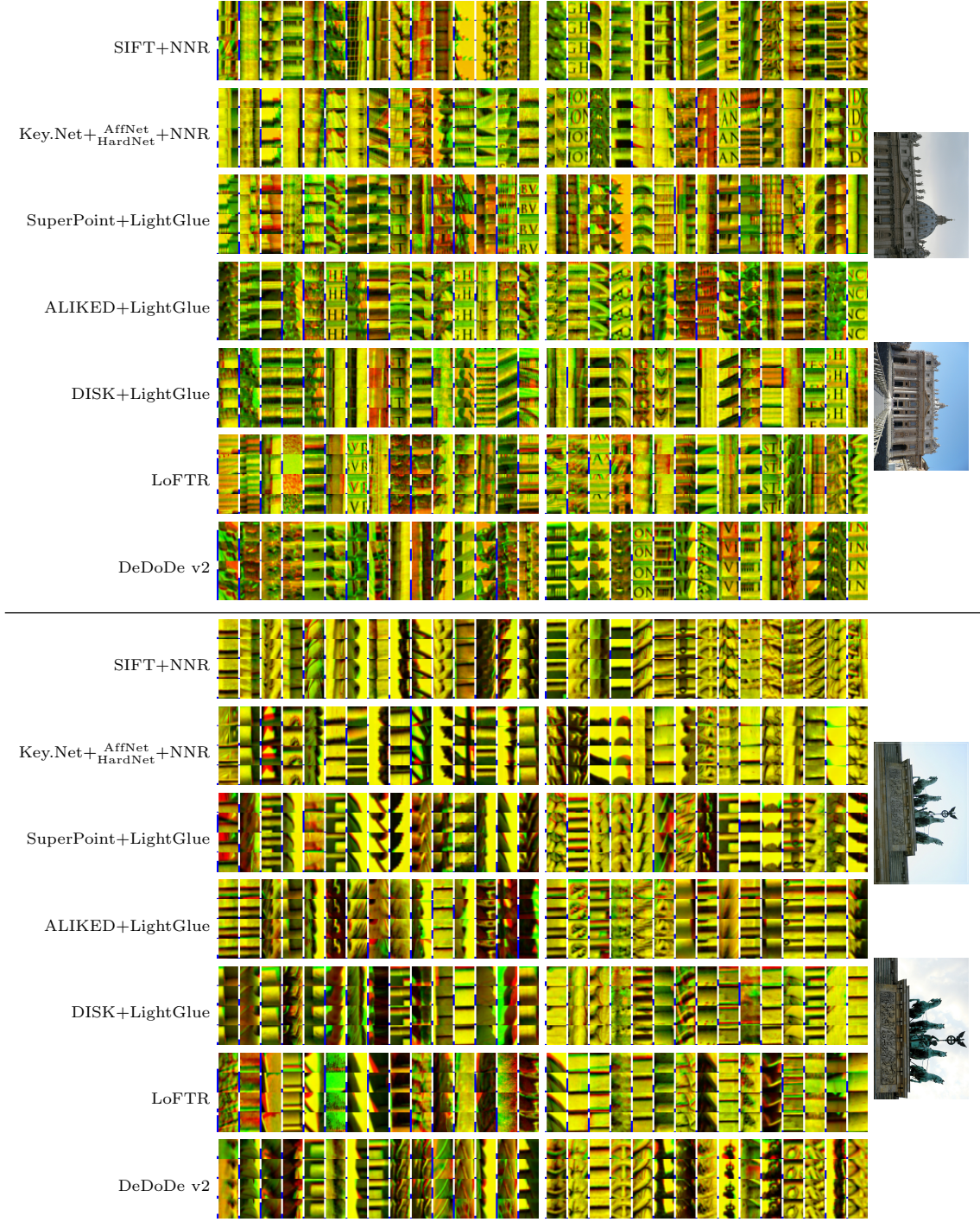


Fig. 7: Overlapped patches as red-green stereographs for 30 random matches for the MegaDepth image pairs shown in the rightmost column of the table. For each base pipeline, the original patches without NCC, with NCC, MOP+MiHo, and MOP+MiHo+NCC are shown from the top to the bottom rows, respectively. The left and right patch clusters correspond to the case where NCC correlation is higher without and with MOP+MiHo, respectively. The blue bar on the left of each patch indicates the maximum epipolar error with respect to the GT up to 10 px, i.e. the patch radius. Please refer to Sec. 4.2.9. Best viewed in color and zoomed in.

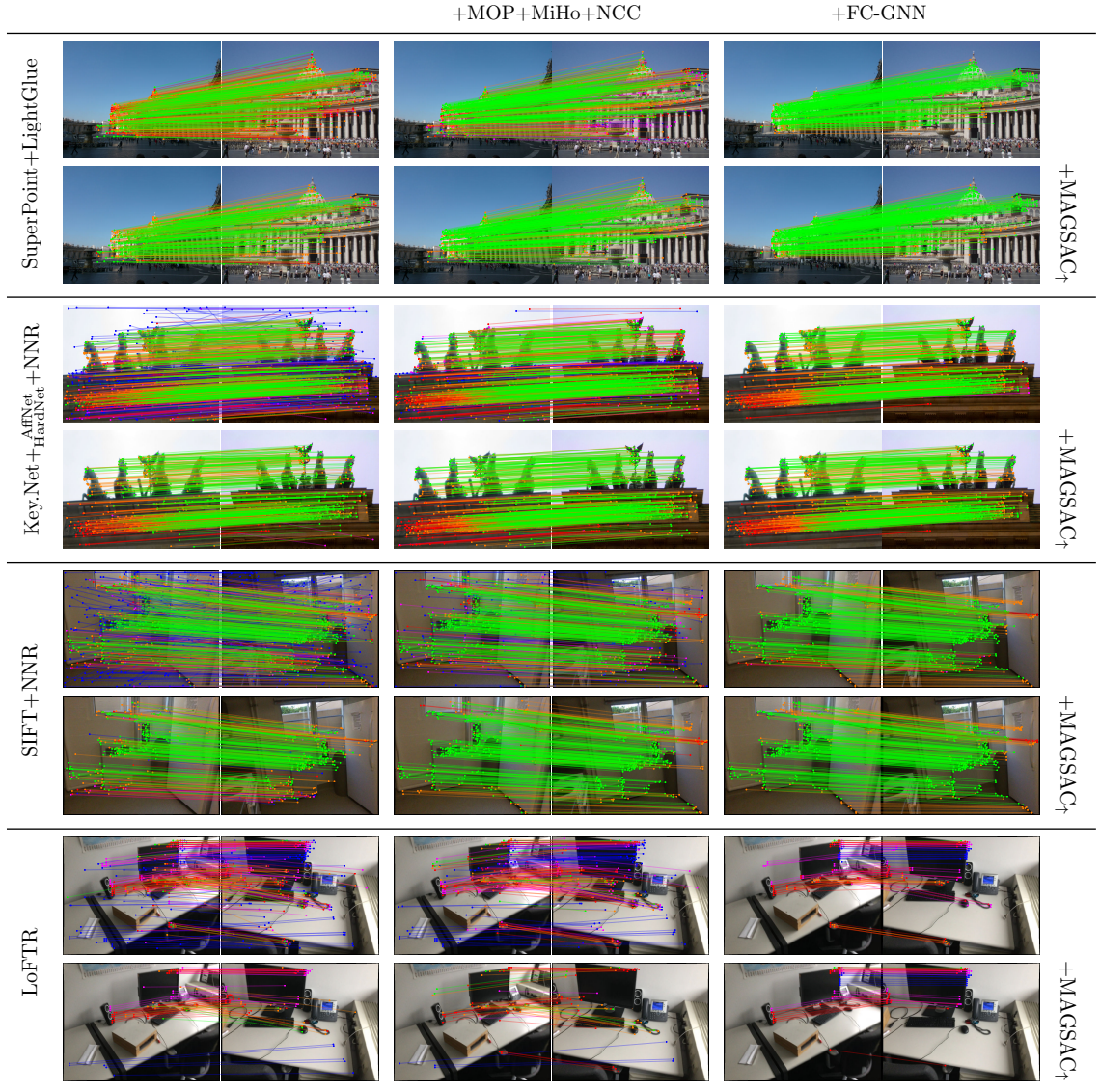
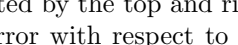


Fig. 8: Visual qualitative comparison for non-planar scenes on example image pairs of MegaDepth (top row sections) and ScanNet (bottom row section). The base pipeline specified on the left is optionally combined with MOP+MiHo+NCC or FC-GNN, and then MAGSAC \uparrow , as indicated by the top and right labels. Matches are colored according to the maximum epipolar error with respect to the GT such that the five consecutive intervals in $[0, 1, 3, 7, 15, \infty]$ px are colored as . Please refer to Sec. 4.2.9. Best viewed in color and zoomed in.

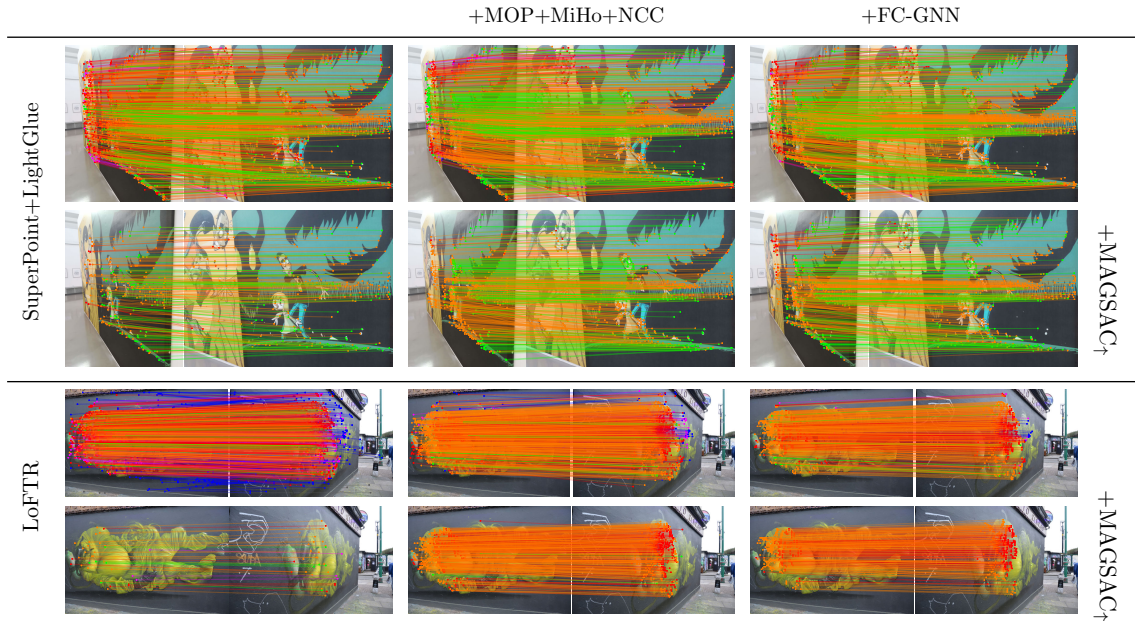


Fig. 9: Visual qualitative comparison for planar scenes in the Planar dataset. The base pipeline specified on the left is optionally combined with MOP+MiHo+NCC or FC-GNN, and then MAGSAC \uparrow , as indicated by the top and right labels, respectively. Matches are colored according to the maximum reprojection error with respect to the GT such that the five consecutive intervals in $[0, 1, 3, 7, 15, \infty]$ px are colored as . Matches where both keypoints are outside the considered plane so that the GT is not valid are marked in gray. Please refer to Sec. 4.2.9. Best viewed in color and zoomed in.